Static and Dynamic Characteristics of Nano-Reinforced Polymer Composites with Application in 3D-Fiber Metal Laminates: Experimental and Numerical Studies

by

Babak Soltannia

A thesis submitted in partial fulfillment of the requirements for the degree of

Doctor of Philosophy

Department of Mechanical Engineering

University of Alberta

Abstract

Crashworthiness, energy absorption capacity and safety are important factors in the design of light-weight vehicles made of fiber-reinforced polymer composite (FRP) components. The relatively recent emergence of the nanotechnology industry has presented a novel means to augment the mechanical properties of various materials. Also, uncontrolled vibration in mechanical systems (e.g. aircraft, trains, and automobiles) may result in undesirable noise and eventually, cause mechanical failure. As a result, recent attempts have contemplated the use of nanoparticles to further improve the resiliency of resins, especially when resins are used for mating FRP components as well as three-dimensional fiber metal laminates (3D-FMLs). 3D-FMLs are a class of novel lightweight hybrid material systems with great potential for use in aforementioned applications. Therefore, a comprehensive understanding of the response of nano-reinforced polymer composites, subjected to various rates of loading, as well as exploring parameters that govern and affect the frequency response of 3D-FMLs is vital for developing reliable structures. In this study, the effects of nano-reinforcement on the mechanical response of a commonly used epoxy resin subjected to different strain rates, were systematically investigated. The results were then compared to those of the neat resin. To characterize the mechanical properties of the nanocomposite, a combination of the strain rate dependent mechanical (SRDM) model of Goldberg and his co-workers, and Halpin-Tsai's micromechanical approach was employed. Subsequently, a parametric study was conducted in addition to statistical approach, to ascertain the influences of various parameters (i.e., the particle type, their weight percentage). Then, the numerical results, as well as statistical results were compared to the experimental data obtained from testing of the neat and the nano-reinforced epoxy resin.

Further, the vibration characteristics of the two more commonly used configurations of 3D-FMLs were experimentally investigated by nontraditional and conventional approaches. The study explored the material damping by the inclusion of two different types of nanocarbon particles (NCPs) within the core and/or interfaces of the hybrid system. The results were presented and compared. The inclusion of NCPs increased the fundamental frequency of the system slightly; however, material damping was enhanced significantly when only 1 wt% NCP was used in the interfacial sections of the system at room temperature.

Keywords: Carbon nanoparticles, functionalized graphene nanoparticles, nanocomposite adhesives, Fiber-metal Laminates (FMLs), vibration, damping, shear deformation, thermal fatigue, Finite Element Method (FEM), Design of Experiment (DOE), Non-destructive Testing (NDT)

Preface

Chapter 3 has been published as a peer-reviewed journal publication in Vol. 2016 of the journal "Nanomaterials" (IF: 1.980; CiteScore: 3.2 (Scopus; 2020)), by B. Soltannia as the 1st author. The title is "Parametric Study of Strain Rate Effects on Nanoparticle-Reinforced Polymer Composites". The paper consists of nine double-column pages and was published in 2016 [1]. Note that Sections 3.2 'Nomenclature' and 3.6 'Vibration Response of Pure and NP-reinforced Polymer Composite Beam' and some latter parts of Sections 3.3 'Introduction', 3.7 'Results and Discussion' and 3.8 'Conclusions' are not part of the published article and have been added later to form Chapter 3.

Chapter 4 is an updated version of a previously peer-reviewed journal paper published in Vol. 8, No. 2 of the journal "Reviews of Adhesion and Adhesives" (CiteScore 1.8 (Scopus; 2020)), by B. Soltannia as the 1st author. The title is "Quantification of the Effects of Strain Rate and Nano-Reinforcement on the Performance of Adhesively Bonded Single-Lap Joints". The paper consists of 19 single-spaced single-column pages and was published in 2020 [2]. Note that Section 4.2 'Nomenclature' is not part of the published article and has been added to this chapter later.

Chapter 5 has been published as a peer-reviewed journal publication in the journal "Sandwich Structures and Materials" (IF: 5.616; CiteScore: 5.1 (Scopus; 2020)), by B. Soltannia as the 1st author. The title is "Static and dynamic characteristics of nano-reinforced 3D-fiber metal laminates using non-destructive techniques". The paper consists of 32 single-spaced single column pages and was electronically published in May 2020 [3]. An abbreviated and preliminary version of this work was presented and published in the proceeding of the 11th Canadian-International Conference on Composites (CANCOM2019) by B. Soltannia as the 1st author. The title is "Vibration Characteristics of Multi-Wall Carbon Nanotubes (MWCNT) Reinforced 3D-Fiber

Metal Laminates (3D-FML)". The conference paper consists of eight single-spaced single-column pages and was selected as one of the five best runner-up conference papers [4]. Note that Sections 5.2 'Nomenclature' and 5.8 'Finite Element Modeling', and Subsection 5.9.4 'Finite Element Results' are not part of the published journal article and were added to this chapter later. Also, note that Sections 5.3 'Introduction' and 5.9 'Results and Discussion', as well as subsection 5.7.4 'Bending Rigidity' have been updated.

Chapter 6 has been presented and published in the proceeding of the 37th Annual Technical Conference of Canadian Machinery Vibration Association by B. Soltannia as the 1st author. Its title is "Vibration Characteristics of Thermally Cycled Graphene Nanoplatelet (GNP) Reinforced 3D-Fiber Metal Laminates (3D-FML)". The conference paper consists of 11 single-spaced single-column pages and received a Student Award for Article and Presentation [5]. Sections 6.4. 'Results and Discussion', and 6.5. 'Conclusions' of this chapter have been updated.

Dedicated to my parents,

Iran and Davood

For their unconditional love and endless support.

I always Love you.

Acknowledgment

I am using this opportunity to express my profound gratitude to my supervisor, mentor, inspirational scientist and my role model of professionalism and integrity, Professor Pierre Mertiny. I would not have been able to advance my thesis without his financial and scientific supports. I cannot thank him enough for encouraging me in becoming a sessional instructor and teaching a course to undergraduate students during my Ph.D. program, and supporting me to work for a Canadian company to gain industrial experience. I am pretty sure I am neither the first person nor the last one who thanks him for ameliorating his/her life and extending the borders of kindness. Professor Mertiny, I sincerely thank you for trusting in my capabilities while many others did not, and for helping me throughout my Ph.D. setbacks without ever losing your hope and enthusiasm. Ich möchte mich recht herzlich bedanken; Ich bin Ihnen sehr dankbar.

I am also very thankful to my supervisory committee members, Professor Michael Lipsett and Professor Donald Raboud for their invaluable guidance and precious advice, my arm's length examiner Professor Ying Hei Chui and my external examiner Professor Gabriel LaPlante, for their constructive comments and suggestions in producing the final version of this thesis. I would also like to thank every and each person involved in the administration of my program, including my examination committee chair, Professor Christopher Dennison, the Department of Mechanical Engineering especially Ms. Gail Dowler, Ms. Linda Paulic, Ms. Serena Pike, Ms. Isabelle Gibbins, Dr. Robyn Braun, Mr. Richard Groulx, and the Faculty of Graduate Studies and Research at the University of Alberta, especially Professor Heather Zwicker, Professor Tracy Raivio and Professor Janice Causgrove Dunn, for their gracious kindness, endless support and incredible inspiration.

I would also like to extend my appreciations to Professor Brian Fleck, Professor John Doucette and Professor Morris Flynn for their continued supports and encouragements during my

Ph.D. program and my involvement in the University of Alberta and graduate students' governance as a member of the Board of Governors and President of the Graduate Students' Association (GSA). Also, my special thanks to Dr. Courtney Thomas, Dr. Julie Tanguay, Ms. Heather Hogg, Ms. Lisa Hareuther, Ms. Laura Hanon, Ms. Fiona Robertson, Ms. Mahsa Toghrai and entire GSA and its incredible people, for their kind and endless supports during my tenure as president of the GSA in 2017-18, one of the most rewarding and eye-opening experiences of my academic life.

I would also like to thank Professor Darrel Doman for his gracious kindness in giving me the opportunity of teaching "Vibrations" to a large class of fourth-year undergraduate students as a visiting sessional instructor at Dalhousie University; I would also like to sincerely thank Professor Raboud again for kindly allowing me to use his unique "Sound and Vibrations" course notes to which I owe my success in instructing the course and receiving good course evaluation. I am very fortunate and grateful to have good colleagues and friends in the Advanced Composite Materials Engineering Group (ACMEG), the University of Alberta, Dalhousie University, and beyond.

Also, I thankfully acknowledge and appreciate the financial support from the federal and provincial governments of Canada and Alberta through Natural Sciences and Engineering Research Council of Canada (NSERC), Alberta Innovates-Technology Futures (AITF), as well as Gerald W Sadler, J. Gordin Kaplan, Donald D. Lougheed, Andrew Stewart, Gerald J. Maier, R. R. Gilpin, and all other financial supports during my Ph.D. program provided through the University of Alberta, the Faculty of Graduate Studies and Research, and the Department of Mechanical Engineering. I wish to be fortunate enough to return their kind investment in me. Last but not least, my deepest love and gratitude goes to my family members. They were always supportive and were encouraging me to continue my education. Undoubtedly, without their endless help and unconditional love and sacrifice, the fulfillment of this study was impossible.

Table of Contents

Abstract ii

Preface iv

Acknowledgment vii

Table of Contents ix

List of Tables xv

List of Figures xvi

Chapter 1 1

Introduction 1

1 Introduction 2

1.1 Introduction 2

1.2 Hypothesis and Thesis Objectives 2

1.2.1 General Objective 3

1.2.2 Specific Objectives 3

1.2.3 Hypothesis 3

1.3 Thesis Organization 4

Chapter 2 6

Literature Review 6

2.1 Introduction 7

2.2 Vibration 8

2.2.1 Static and Dynamic Characterization of Thin/Thick Isotropic/Anisotropic Beams/Plates/Shells 8

2.2.2 Mathematical, Numerical, Statistical, Stochastical and Experimental Approaches Used in Static and Dynamic Characterization of Objects 10

2.3 Adhesives 11

2.3.1 Adhesive Types 11

2.3.2 Surface Treatment 13

2.3.3 Nanocomposite Adhesives 14

2.4 2D- and 3D-Fiber Metal Laminates (2D- and 3D-FMLs) 16

2.5 Finite Element Modeling 17

Chapter 3 20

Parametric Study of Strain Rate Effects on Nanoparticle-reinforced Polymer Composites and Their Dynamic Behavior 20

3.1 Publication Statement 21

3.2 Nomenclature 21

3.3 Introduction 24

3.4 Experimental Investigation 29

3.4.1 Materials and Specimen Preparation 29

3.4.2 Characterization of the Mechanical Properties of Adhesives 32

3.5 Problem Statement and Modeling Strategy 34

3.5.1 Strain Rate Dependent Continuum-based Constitutive Equation of Polymers 34

3.5.2 The Halpin-Tsai Micromechanical Model 38

3.6 Vibration Response of Pure and NP-reinforced Polymer Composite Beam 40

3.6.1 Governing Equation of Motion 40

3.6.2 Finite Element Modeling 42

3.7 Results and Discussion 43

3.8 Conclusions 49

Chapter 4 51

Quantification of the Effects of Strain Rate and Nano-reinforcement on the Performance of Adhesively Bonded Single-Lap Joints 51

4.1 Publication Statement 52

4.2 Nomenclature 52

4.3 Introduction 53

4.4 Materials and Methods 55

4.5 Design of Experiments (DOE) Methodology 57

4.6 Results 61

4.6.1 Influence of the Variables on the AUSS of SLJs 61

4.6.2 Influence of GNP wt% on AUSS of the SLJs 65

4.7 Discussion 70

4.8 Conclusions 71

Chapter 5 73

Static and Dynamic Characteristics of Nano-Reinforced 3D-Fiber Metal Laminates Using Non-Destructive Techniques 73

5.1 Publication Statement 74

5.2 Nomenclature 74

5.3 Introduction 77

5.4 Research Objectives of This Study 82

5.5 Materials and Fabrication 84

5.5.1 Materials 84

5.5.2 Specimen Manufacturing 85

5.5.2.1 3D-FGF Specimens……85

5.5.2.2 3D-FML Specimens……...86

5.5.2.3 Foam Core Sandwich Specimens Specimens……87

5.5.2.4 NCP Reinforced 3D-FGF and 3D-FML Specimens……...87

5.5.2.5 Specimen Configurations and Nomenclature.……88

5.6 Experimentation 89

5.6.1 Vibration Testing 89

5.6.2 Bending Rigidity Testing 92

5.7 Data Analyses 93

5.7.1 Fundamental Frequency 93

5.7.2 Damping Ratio 94
5.7.3 Vibration Signal Extraction and Analysis 95
5.7.4 Bending Rigidity 97
5.8 Finite Element Modeling 98
5.9 Results and Discussion 100
5.9.1 Bending Rigidities 100
5.9.2 Fundamental Frequencies 103
5.9.3 Damping Ratio 107
5.9.4 Finite Element Results 109
5.10 Conclusions 110
Chapter 6 112
Vibration Characteristics of Thermally Cycled Graphene Nanoplatelet (GNP) Reinforced 3D-Fiber Metal Laminates (3D-FML) 112
6.1 Publication Statement 113
6.2 Introduction 114
6.3 Materials and Methods 118
6.3.1 Materials 118
6.3.2 Specimen Preparation 118
6.3.3 Cyclic Thermal Fatigue Test 119
6.3.4. Bending Rigidity Testing 121

6.3.5 Testing and Analysis Procedures 122

6.3.6 Vibration Signal Extraction and Analysis 123

6.4 Results and Discussion 124

6.5 Conclusions 128

Chapter 7 129

Summary and Conclusion 129

7.1 Summary 130

7.2 Conclusions 130

7.3 Recommendations 134

Bibliography 136

Appendices 163

Appendix I 163

Appendix II 165

Appendix III 181

List of Tables

Table 3.1 Calculated rate dependent material constants of WS-105 epoxy resin. 44

Table 3.2 Material specification of aluminum, pure and GNP-reinforced WS-105 epoxy resin beams 47

Table 3.3 Fundamental frequencies and damping ratios of aluminum, pure and GNP-reinforced epoxy resin obtained numerically 47

Table 4.1 Manipulated variables for the phase 60

Table 4.2 Controlled variables for the phase 60

Table 4.3 Manipulated variables for the phase 2 60

Table 4.4 Controlled variables for the phase 2 60

Table 4.5 Effect estimates results of the phase 1 62

Table 4.6 Regression table for the phase 1 analyses 63

Table 4.7 Effect estimates table of the phase 2 of analyses 66

Table 4.8 Reduced regression values of the phase 2 of analyses 68

Table 5.1 Preform 3D-FGF specifications [198]. 86

Table 5.2 Specimen configurations and nomenclature. 89

Table 5.3 Modulus of elasticity of baseline aluminum material and 3D-FGF facial fabrics with and without NCP reinforcement. 103

Table 5.4 Fundamental frequencies obtained experimentally (via GS and LDV) and analytically 105

Table 5.5 Comparison of damping ratios obtained from GS and LDV measurements. 107

Table 6.1 Specimen configurations and nomenclature. 120

Table 6.2 Temperature range, type of specimens and results. 120

List of Figures

Figure 2.1 Schematic illustration of (a) longitudinal bending vibration of isotropic beam; (b) lateral (transversal) bending vibration of isotropic beam; (c) longitudinal bending vibration of anisotropic beam; (b) lateral (transversal) bending vibration of anisotropic beam. 9

Figure 2.2 Schematic illustration of (a) 2D-FML and (b) 3D-FML beams. 17

Figure 3.1 Representative tensile coupons of the neat and nanoparticle reinforced epoxy resins, and their dimensions (in mm). "R" stands for radius. 32

Figure 3. 2 Experimental setup for the (a) static; (b) quasi-static and higher loading rate tests... 33

Figure 3.3 Influence of strain rate, on the tensile elastic modulus of the epoxy resin reinforced with various amounts (wt%) of GNP. 33

Figure 3.4 (a) Two dimensional illustration of a Timoshenko beam with free-free boundary condition; (b) Three dimensional illustration of first mode of longitudinal bending vibration of isotropic beam with free-free boundary condition, undergoing free vibration. 40

Figure 3.5 Timoshenko beam element: degrees of freedom of the two-noded element. 42

Figure 3.6 Influence of the time steps (dt) on the numerical stability of the adopted iterative procedure used for predicting the stress-strain curves of the neat WS-105 epoxy resin at an arbitrary strain rate 44

Figure 3.7 Variation of the tangential modulus of WS-105 neat epoxy resin, as a function of strain when the material loaded under quasi-static strain rate of 10^{-1} s^{-1} 45

Figure 3.8 Comparison of predicted and experimental stress-strain curves of WS-105 resins reinforced with various types of nanoparticles; (a) Influence of nanoparticles type; (b) Influence of GNP weight-content for a quasi-static strain rate of 10^{-3} s^{-1}; and (c) influence of strain rate on the stress-strain responses of resin with 1wt% GNP. 46

Figure 3.9 (a) Mode shapes of an aluminum beam with F-F BC, (b) Transient response of an aluminum beam with F-F BC used to calculate its damping ratio, (c) Transient response of pure epoxy resin, and (d) Transient response of GNP-reinforced epoxy resin. 48
Figure 4.1 Typical single-lap joint specimens (dimensions in mm; drawing not to scale) [124]. 56
Figure 4.2 Experimental test setup used in the high strain rate test (tensile impact apparatus) [124]. 56
Figure 4.3 Experimental setup used for conducting the static and quasi-static strain rate tests [124]. 57
Figure 4.4 Flowchart showing the required steps for design of experiments. 59
Figure 4.5 The Pareto chart of the phase 1 61
Figure 4.6 Interaction (Mean) plots of the phase 1 tests (see Table 4.1 for the meaning of -1, 0 and 1 noted on the chart). Note that data is valid only for discrete values at -1, 0, and 1, lines have been added to guide the eye. Some data points are offset from the integer values by the software to improve clarity. 63
Figure 4.7 Surface plot of AUSS (MPa) vs. strain rate and nano particle type (for the SLJ with CFRP adherend). Note that a continuous surface is shown for illustration purposes only, with data being valid only for discrete values at -1, 0, and 1 65
Figure 4.8 Pareto chart of the phase 2 of analyses 66
Figure 4.9 Interaction (Mean) plot of the phase 2 of analyses (see Table 4.3 for the meaning of -1, 0 and 1 noted on the chart). Note that data is valid only for discrete values at -1, 0, and 1, lines have been added to guide the eye. Some data points are offset from the integer values by the software to improve clarity. 67
Figure 4.10 Half-normal plot of the phase 2 67

Figure 4.11 Surface plot of AUSS (MPa) vs. nanoparticle wt% and strain-rate (CFRP adherend). Note that a continuous surface is shown for illustration purposes only, with data being valid only for discrete values at -1, 0, and 1. 69

Figure 4.12 Taguchi results based on maximum S/N for the phase 2. Note that data is valid only for discrete values at -1, 0, and 1, lines have been added to guide the eye. Some data points are offset from the integer values by the software to improve clarity. 70

Figure 5.1 Schematic illustration of (a) 2D-FML and (b) 3D-FML beams. 81

Figure 5.2 Schematic of research subjects considered in the present work. 84

Figure 5.3 3D-FGF images: (a) preform 3D-FGF; (b) its resin impregnated composite; and (c) 3D-FGF with different thicknesses. [198] 86

Figure 5.4 Experimental test setup for recording vibration signals of free-free supported specimens using the GS and LDV. 91

Figure 5.5 (a) Three- and (b) Four-point bending rigidity test setup. 92

Figure 5.6 Typical vibration signals and the representative signal envelopes for (a) aluminum and (b) 1% GNP-reinforced 3D-FML specimens (GNP in both core and interface). 95

Figure 5.7 Power spectrum of: (a) Aluminum; (b) 3D-FML specimens with 1% GNP-reinforced core and interfaces. 96

Figure 5.8 Mesh representation used for finite element analyses: (a) Aluminum (b) 3D-FML1 (c) 3D-FML9 (d) 3D-FGF17 (e) 3D-FGF20 99

Figure 5.9 Specimen flexural bending rigidity obtained theoretically and experimentally via Eqs. (5.2), (5.10) and (5.14). 102

Figure 5.10 Influence of NCP reinforcement on fundamental frequencies of 3D-FGF and 3D-FML. 105

Figure 5.11 Influence of NCP reinforcement on the fundamental frequencies of 3D-FMLs as a function reinforced constituent(s). 106
Figure 5.12 FESEM images of NCP reinforced 3D-FML resin phase: (a) GNP; (b) MWCNT agglomeration; (c) voids; and (d) well-dispersed MWCNT reinforcement. 106
Figure 5.13 Influence of NC-reinforcement on the damping ratio of (a) 3D-FGF and (b) 3D-FML hybrid materials 109
Figure 5.14 Fundamental frequencies obtained through finite element analyses using LS-DYNA commercial software versus experimental and empirical measurements 110
Figure 6.1 (a) Typical heating/cooling cycle, and (b) specimens in the environmental chamber. 121
Figure 6.2 Three-point bending rigidity test setup. 122
Figure 6.3 Experimental test setup for recording vibration signals of specimens with free-free boundary conditions using a Grindosonic device. 122
Figure 6.4 (a) Typical vibration signal and its representative envelope; (b) power spectrum (aluminum specimen). 123
Figure 6.5 Experimental and theoretical flexural bending rigidity of thermally cycled specimens in comparison with non-cycled ones (Eq. 5.10, Eq. 5.2 and Eq. 5.14 have been explained in detail in Sections 5.7.4, 5.7.1 and 5.9.1, respectively) 126
Figure 6.6 (a) Specimen averaged normalized fundamental frequencies, and (b) damping ratios. 127

Chapter 1

Introduction

1 Introduction

1.1 Introduction

Unwanted and unharnessed vibration in structures results in undesirable noise and may cause mechanical failure. Such problems are often encountered in transport vehicle body components, airplane cabins, and train and subway enclosures. Three-dimensional fiber metal laminates (3D-FMLs) are speculated to offer a damper vibration response compared to conventional fiber-reinforced composites, as well as 2D-FMLs, especially if their polymer matrix is reinforced with nanoparticles. Characterizing the different parameters that govern and affect the static and dynamic response of such sandwich composites, along with the polymer composites as one of their main constituents, would advance the knowledge required to produce systems with high damping and proper noise and vibration reduction attributes. Therefore, it is important to understand and characterize the static and dynamic response of polymer composites and 3D-FMLs and improve their vibration characteristics, while maintaining or augmenting their stiffness-to-weight ratio, by effective solutions, thereby reducing their vibration and the radiated noise, especially when such systems are subjected to a critical frequency range (range of frequencies near its natural frequency).

1.2 Hypothesis and Thesis Objectives

General and specific objectives can be extracted from answering to the following research question: “Which parameters affect the vibration characteristics of 3D-FMLs, and how can the performance of 3D-FML systems be enhanced when subject to vibratory loading?” Based on this research question, the general objective of this work can be articulated as follows.

1.2.1 General Objective

The general objective for this research is to investigate the static and dynamic characteristics of polymer composites and 3D-FMLs, and to formulate design recommendations to improve the performance of 3D-FML structural components under vibratory loads and enhance their stiffness-to-weight ratio by incorporating energy- and/or optimization-based approaches. From the general objective, the derived specific objectives are fourfold as follows.

1.2.2 Specific Objectives

1 - Study the effect of nanoparticle reinforcement on the enhancement of stiffness and vibration characteristics of polymer adhesives and polymer composites as one of the main constituents of 3D-FMLs.

2 - Study the effect of nanoparticle reinforcement on stiffness enhancement as well as static and dynamic response of different configurations of 3D-FMLs.

3 - Study the effect of temperature and moisture on the vibration response of such modified 3D-FMLs.

1.2.3 Hypothesis

A novel way of enhancing structural (static and dynamic) properties of 3D-FMLs is believed to be achievable by enhancing the stiffness and damping properties of their main constituent, their polymer matrix. This may become possible by the inclusion of nanoparticles in the matrix of the sandwich system. Hence, it is hypothesized that one may be able to enhance the stiffness-to-weight ratio of the system and reduce its cost by strategically reinforcing sections of the 3D-FML, i.e., between the laminates of two face sheets using nano-reinforced polymer composites.

1.3 Thesis Organization

The present dissertation was organized in a hybrid format, i.e., the amalgamation of paper-based and non-paper-based (traditional) content.

- Chapters 1 and 2 of this thesis provide a general overview of the thesis and its structure, as well as the background to the study and a literature review.
- Chapters 3, 4, 5 and 6 each were written based on published articles.
- Chapter 3 presents the results of parametric (systematic numerical) studies on the static and dynamic behavior of neat and nanoparticle-reinforced (NP-reinforced) thermoset resin (adhesive). This study provides some indication of the effects of NP modification on structural performance, static and dynamic characteristics of NP-reinforced polymers and possible causes for their enhanced performance. The effect of load and time on neat and NP modified thermoset polymer is also explored. Hence, this work serves to obtain a deeper understanding of temporal aspects in the context of the thesis. This chapter also provides the outcomes of a numerical study on the transient response of neat and GNP-reinforced thermoset resin (adhesive) based on structural dynamics.
- Similar to Chapter 3, Chapter 4 is based on the outcome of a series of statistical studies on the effect of incorporating NPs in thermoset resin (adhesive), a feasible range of nanoparticles weight percentage (wt%), as well as processing and fabrication of NP-reinforced polymers (thermoset resin (adhesive)) and their composites with application in single-lap joint (SLJ). SLJs can be considered a simpler yet somewhat similar geometry to 3D-FMLs. This chapter thus serves as a preparatory part for work on 3D-FMLs. The study also provides some indication of the effects of NP modification on structural performance and static characteristics

of NP-reinforced polymers and their composites application in SLJs and possible causes for their enhanced performance.

- Chapter 5 deals with the rather complex hybrid system of material and geometry in 3D-FMLs. This chapter is the core part of the thesis and provides the outcomes of systematic studies on processing, fabrication, and behavior of NP-reinforced polymers (thermoset resin (adhesive)) and their composites with application to 3D-FMLs. Static and dynamic characteristics were investigated experimentally based on a non-destructive testing (NDT) method and are compared with a proposed empirical model. The chapter concludes with comparing results from finite element analyses (FEA) to experimental and empirical findings.
- Chapter 6 is an extension of the work in Chapter 5 as it expands into temperature and moisture effects.
- Chapter 7 summarizes the major findings of all parts of this research and provides a concluding discussion. Moreover, suggestions and recommendations for further advancement of the ongoing research are provided. In addition to summarizing Chapters 3 to 6, the learnings from the different studies and how they support or contradict the research hypothesis, with Chapters 5 and 6 being the most impactful pieces of work, are discussed.

Chapter 2

Literature Review

2.1 Introduction

Crashworthiness, energy absorption capacity and safety are important factors in the design of light-weight vehicles made of fiber-reinforced polymer composite (FRP) components. The relatively recent emergence of the nanotechnology industry has presented a novel means to augment the mechanical properties of various materials. Also, unwanted and unharnessed vibration in mechanical systems (e.g. aircraft, trains, and automobiles) may result in undesirable noise and eventually, cause mechanical failure. As a result, recent attempts have contemplated the use of nanoparticles to further improve the resiliency of resins, especially when resins are used for mating FRP components as well as 3D-FMLs. 3D-FMLs are a class of novel lightweight hybrid material systems with great potential for use in the aforementioned applications. 3D-FMLs are speculated to offer damper vibration response compared to the conventional fiber-reinforced composites, as well as 2D-FMLs, especially if their polymer matrix is reinforced with nanoparticles. Therefore, a comprehensive understanding of the response of nano-reinforced polymer composites, subjected to various rates of loading, is vital for developing reliable structures, as well as exploring parameters that govern and affect the frequency response of 3D-FMLs.

Characterizing the different parameters that govern and affect the static and dynamic response of such sandwich composites, along with polymer composites as one of their main constituents, may provide the understanding for producing a system with high damping and proper noise and vibration reduction attributes. Therefore, it is important to understand and characterize the static and dynamic response of polymer composites and 3D-FMLs and improve their vibration characteristics, while maintaining or augmenting their stiffness-to-weight ratio, by effective solutions, thereby reducing their vibration and the radiated noise, especially when such systems are subjected to a critical frequency range.

2.2 Vibration

2.2.1 Static and Dynamic Characterization of Thin/Thick Isotropic/Anisotropic Beams/Plates/Shells

Transverse vibration of a thin rectangular plate, which was first observed and demonstrated by Chladni [6–9] in the early 19th century, is one of the simplest yet most sophisticate classical problems, which attracted many mathematical physicists to tackle solving this old problem. Despite many attempts to obtain a closed form solution, this problem only has an exact analytical solution when two opposite edges of the plate are simply supported [10,11]. Amongst many approximate solutions, a method of dual separation of variables and a method of superposition have been found more attractive and applicable to solving the problem of free vibration of plates with arbitrary boundary conditions [12–14]. The importance of vibration of plates, as an important structural element of mechanical system, stimulated the development of solutions based on variational principles to obtain a better understanding about the mechanical behavior of complex systems. The Ritz method is one of this type of approached used to solve the free transverse vibration problem of a plate with all free edges [15]. Later, Timoshenko solved the problem of free vibration of plates with all clamped edges [16]. The vibration of other types of isotropic plates with different geometry and boundary conditions has also been investigated, e.g., Meleshko and Papkov [17] investigated the problem of bending vibration of rectangular plates using the method of superposition; Shakeri et al. [18–26] studied the free vibration of parallelogram plates with an all-edges free boundary conditions experimentally and theoretically using the method of superposition; and Barnyak and Soltannia [27,28] studied the vibration of elliptical plate with a clamped boundary condition. To study the effect of complex in-plane loads applied to a plate, the Rayleigh-Ritz method was developed [29,30]. Dawe and Craig utilized the Rayleigh-Ritz method

to study vibration and stability of thin laminate rectangular composite plates under applied in-plane load [31]. Beams are simpler structures and can be defined as a plate having one dimension (length) much larger than the other two dimensions (i.e., length almost 10 times greater than width and almost 40 times greater than thickness). Hence, studying vibration characteristics of a beam can be considered a preliminary step towards exploring the characteristics of vibrating plates. Figure 2.1 illustrates the first modes of longitudinal and lateral (transversal) bending vibration of isotropic and anisotropic beams. It is also worth mentioning that throughout this work, free vibration of a beam is of interest where after initial excitation, the beam vibrates on its own and no external force is acting on the beam to derive the vibrations. Free vibration is in contrast to forced vibration where the external stimulus acts on the beam.

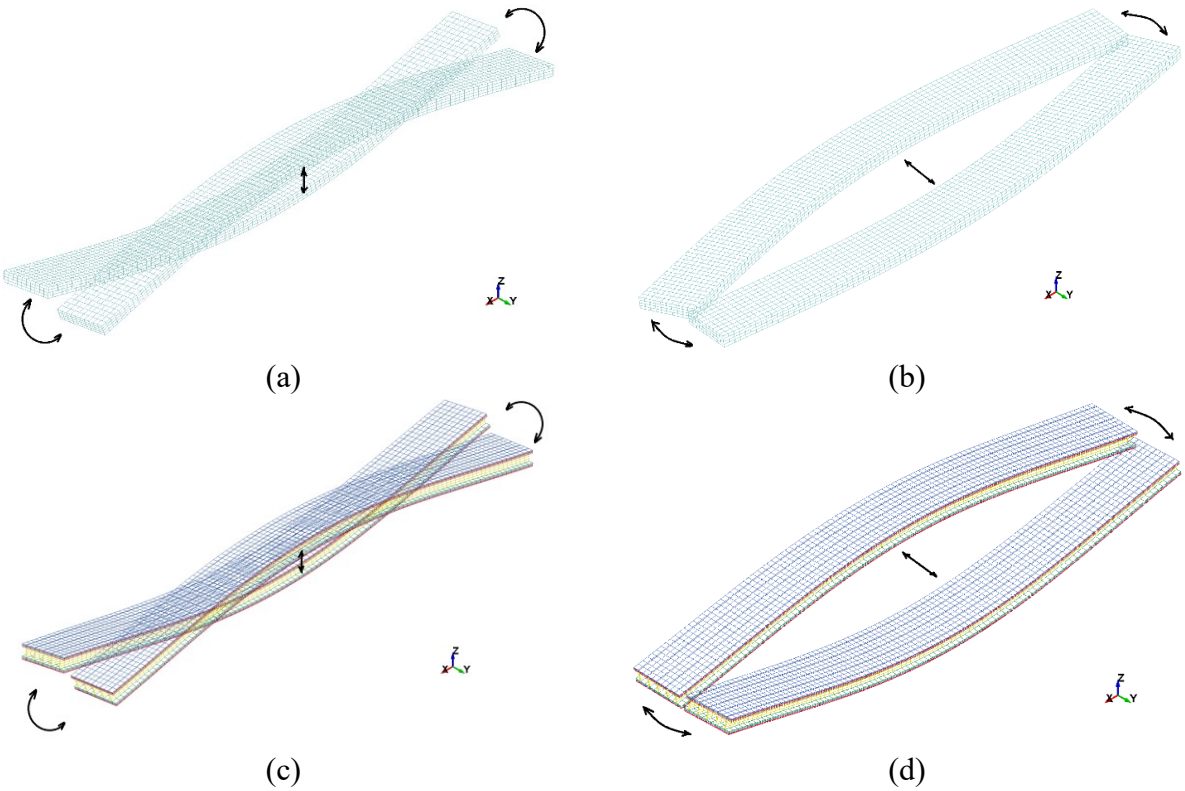

Figure 2.1 Schematic illustration of (a) longitudinal bending vibration of isotropic beam; (b) lateral (transversal) bending vibration of isotropic beam; (c) longitudinal bending vibration of anisotropic beam; (b) lateral (transversal) bending vibration of anisotropic beam.

2.2.2 Mathematical, Numerical, Statistical, Stochastical and Experimental Approaches Used in Static and Dynamic Characterization of Objects

Hu et al. [32] analyzed the vibration response of twisted angle-ply laminated plates using the Rayleigh-Ritz method based on the Mindlin plate theory. In another work, Lei et al. [33] utilized the Ritz method to investigate the damping properties of functionally graded thin laminate composite plates, reinforced with carbon nanotubes (CNT), with clamped boundary conditions. Chen et al. [34] used Galerkin's method to analyze the nonlinear vibration response of rectangular laminated composite plates. Kant and Swaminathan [35] developed a higher-order theory, considering through-thickness shear effects for analyzing the free vibration of sandwich plates. Tu et al. [36] formulated a finite element approach to model the vibration and bending characteristics of laminated and sandwich composite plates using a nine-node rectangular element formulated based on a higher-order shear-deformation theory, thereby accounting for the variation of the through-the-thickness shear.

In addition to the aforementioned analytical and semi-analytical techniques used to solve vibration problems of isotropic and anisotropic plates, Bardell et al. [37], and Tsay and Reddy [38] used the finite element method (FEM) to study vibration of orthotropic plates. Ahmadi Moghaddam and Mertiny [39–41] employed stochastic finite element analysis and introduced effective means to predict material properties of particulate modified polymer composites for elucidating experimental studies and guiding the design of this class of hybrid materials. Improving the damping characteristics of laminated or sandwich composite plates has also been explored experimentally by several researchers. The use of inherently damped materials and nanoparticles (NPs) as passive damping tools on the one hand, and the use of external damping sources as an active damping strategy on the other hand, have been found to generate the most

effective approach for enhancing the dynamic damping properties of composite materials and structures. Zou et al. [42], Hajikhani et al. [43], Soltannia et al. [4,5], and De Cicco and Taheri [44] experimentally investigated the vibration characteristics of laminated and sandwich composite beams using nondestructive testing (NDT) techniques.

2.3 Adhesives

Adhesives have been used in bonding applications for many decades, with effective methods of adhesive bonding emerging in the mid-1940s as a result of enhancements in synthetic polymers as the precursor material [45]. Synthetic polymers are capable of adhering to most materials and are able to transfer a considerable amount of load. Kinloch in 1987 defined an adhesive as a material that joins adherends and resists dissociation of the adherends [46]. Structural adhesives are materials that can carry a significant amount of load, and sometimes improve the strength and stiffness of the structure [47]. Of great interest is the concept of 'cohesion' and 'adhesion', where the first term refers to the intermolecular forces inside one material while the latter one is concerned with the intermolecular forces established at the interface of bonding substances or substrates named adherends after bonding [48]. Bonded substances fail in the cohesion zone or at the interface where adhesive and adherend meet, or by a combination of both. The interphase or the zone enclosed by the adhesive and adherend has different chemical and mechanical properties from those of the bulk adhesive and adherend, which plays a significant role for the adhesion strength.

2.3.1 Adhesive Types

From a chemical point of view, there are two types of polymers: thermosets and thermoplastics. Thermosets have a highly crosslinked structure and cannot be reformed again after solidification (cure). In contrast, thermoplastics only contain linear and branched polymer chains

with weak bonding between adjacent chains. Therefore, thermoplastics melt at sufficiently high temperatures, allowing them to be reshaped and thus be recycled. Some examples of thermoset polymers are: epoxies (often used in high-performance fiber reinforced polymer composites (FRPC)); polyesters (often used in low-cost FRPC), polyurethanes (a highly durable polymer with high resilience); and polyimides (typically for high temperature applications). The group of thermoplastic polymers includes: polyethylene (the most widely used plastic); polypropylene (a fatigue resistant polymer); polyamide (known for its high resilience and tenacity, e.g. Nylon 6 or high strength Kevlar fiber); and polyvinyl chloride (the third most common plastic).

Structural polymer adhesives can be categorized as follows: high temperature adhesives (polyimides, bismaleimides, and phenolics), silicones (provide excellent sealant for low strength applications, high-temperature resistance and a high degree of flexibility), anaerobics (polymer compound with a specially formulated curative that only reacts in the absence of oxygen, predominantly used for bonding metallic cylindrical substrates), polyurethanes (offer flexibility at low temperatures and fatigue resistant), cyanoacrylates (have capability of rapid curing but weak resistance to temperature and moisture), acrylics (are versatile adhesives with fast bonding capability, requiring less surface treatment), and epoxies (having high strength). From a physical and design point of view, two basic types of adhesives are available: dry adhesives (reversible adhesives) [49–51] and wet adhesives (irreversible or ordinary adhesives). In general, an increased usage of resin-matrix composite materials and structures, including for operation in challenging environments such as elevated temperature conditions, has promoted the development and emergence of high-performance epoxy resins and adhesives.

2.3.2 Surface Treatment

In general, surface engineering refers to physically or chemically altering and modifying the surface properties in favor of requirements. For example, the application of physical surface modification or patterning can be seen for dry adhesives [49–51], and the application of chemical surface treatment is observed in thin film composite membranes used for water treatment [52–55] or anti-icing surfaces. In terms of high-performance composite materials or structures, especially in terms of bonding joints or thin-film metal to carbon- or glass-fiber reinforced polymers in the case of 2D- or 3D-FMLs, surface treatment refers to the required chemical and/or physical processes to render bonding surfaces of substrates receptive to the adhesive. The surface quality plays an important role for bond strength and integrity of joints and sandwich structures [45]. Enhancing adhesion between metals and polymers is a rigorous yet inevitable process affecting final product's quality. Mechanical surface treatments include sandpaper abrading, sandblasting, chemical etching, phosphoric acid anodizing (PAA), and other mechanical, chemical, electrochemical processes or coupling agents [56,57]. Utilizing surface treatment before lamination enhances mechanical properties of FMLs by altering surface morphology, surface energy and wettability [58–62].

Coupling nanoparticles are an interesting aspect of surface treatment in the context of this research. Konstantakopoulou and Kotsikos [63] showed that bond strength between aluminum and glass fibers reinforced polymer (GFRP) composites is higher when the surface is grit-blasted compared to anodized surfaces. They also showed that the inclusion of multi-walled carbon nanotubes (MWCNTs) ameliorated adhesion strength. They further demonstrated that the enhancement in adhesion strength in the presence of MWCNTs was greater in the case of anodized surface-treated samples compared to grit-blasted samples. They attributed this to the pores

developed during the anodization process. Khurram et al. [64] studied the effect of pressure on adhesion strength. They found that increasing the pressure results in higher adhesion strength which can be attributed to higher filling performance of MWCNTs into micro-pores caused by chromic acid treatment.

2.3.3 Nanocomposite Adhesives

Nanocomposite adhesives have many applications in the aerospace, automotive, naval, medical and construction industries. Nanocomposite adhesives are increasingly being used following the advent of nanotechnology. In 1999, Kim and Reneker noted that the stiffness of nanofiber-reinforced polymer composite becomes ten times greater compared to the pristine material [65]. Carbon nanofibers (CNFs) can chemically functionalize facile sites with additives or fillers to create a stronger interfacial bond with the matrix. DeArmitt and Rothon mentioned that in contrast to nanoparticles, it is widely presumed that additives are cheap [66], however this is not always the case. As the nanoparticle production grows, nanoparticles are more available in large quantities, and their price greatly depends on their purity and type [67]. The application of carbon nanotubes (CNTs) was first introduced by Iijima in 1991 [68]. There are two main types of these sheets of graphite forming a tube: single-walled carbon nanotubes (SWCNTs) consisting of a single graphene layer shaped as a cylinder with diameter of 1-2 nm [69,70], and MWCNTs containing multi coaxial graphene cylinders with outer diameter of 3-10 nm. The estimated elastic modulus and strength of CNTs are 1 TPa and 150 MPa, respectively [71,72]. Due to weak Van der Waals forces between the layers, tension loads will be carried only by the out layer of MWCNT [71]. In 2000, Qian et al. reported that CNTs could evolve strength of composite adhesives by 25% [73]. Liu et al. [74] investigated the effect of functionalized SWCNT on the damping properties of composite materials. They investigated the influence of chemical crosslinking between SWCNT

and epoxy resin in polymer composites on the interfacial shear strength and damping properties of the composites. They found that enhancing the degree of crosslinking between SWCNT and epoxy resin, by forming functional groups on the SWCNT, increases the interfacial shear strength of the polymer composite. However, the SWCNT functionalization can either increase or decrease the loss factor, depending on the combined effects of operational stress range, nanotube aspect ratio, and interfacial shear strength. Nevertheless, they observed that merely adding randomly dispersed SWCNT ropes generally augments the damping ability of the polymer composite, which can further be enhanced by aligning the nanoropes in the loading direction.

In general, graphene nanoplatelets (GNP) are 1 nm-thick graphene sheets piled on top of each other. Their lateral dimensions can vary from 25 nm to micrometers [75]. The quality of a nano-reinforced adhesive is tied to the quality and level of dispersion of nanoparticles within the adhesive. Dispersing the filler is rigorous process because formation of agglomerations can act as defect zone, mitigating performance instead of evolving it.

Ahmadi-Moghadam et al. [76] demonstrated that the use of chemically functionalized GNP (G-Si) using a silane coupling agent can result in significant improvement in mechanical and fracture response of composite materials compared to non-functionalized GNP, due to the chemical affinity of the functional group (Si) bonded to the surface of GNP with the host resin, thus providing a stronger interface between each nanoparticle and some polymeric matrices. They reported that the inclusion of 0.5 and 1 wt.% pristine and amino-functionalized GNP enhanced the ductility of 3D-FMLs.

2.4 2D- and 3D-Fiber Metal Laminates (2D- and 3D-FMLs)

At this juncture, it is worth mentioning some of the relatively recent efforts expended in developing more resilient, cost-effective and lightweight hybrid materials, notably, FMLs [77,78]. FMLs are hybrid laminates consisting of thin alternating bonded layers of thin metallic sheets (e.g., aluminum or magnesium alloys) and fiber/epoxy [79]. FMLs were developed first in the early 1980s as a more cost-effective alternative to CFRP used in the aerospace industry. The first FML was ARALL (an acronym for aramid reinforced aluminum laminate), developed by a student at the University of Delft, Marissen, which consists of a layup of aramid fiber layers with aluminum layers [80]. Since these pioneering efforts, various FMLs have been developed and produced using different fiber types, such as carbon and aramid. A new rendition of conventional thin FMLs was recently introduced by Asaee and Taheri [81], referred to as three-dimensional FLM. This class of FML has been demonstrated to possess exemplary characteristics compared to conventional FRPs and FMLs, especially from the perspective of crashworthiness and impact tolerance, as demonstrated in [82]. A 3D-FML is essentially a sandwich composite consisting of a novel 3D fiberglass fabric (3D-FGF), sandwiched between thin sheets of a lightweight metallic alloy (e.g., aluminum or magnesium alloys). The superior responses of various configurations of this class of 3D-FML under static and dynamic loading conditions have been demonstrated, promising the suitability of this type of FML in forming lightweight structural panels, especially for meeting recent weight reduction and thus fuel efficiency targets in the automotive industry [4,5,44,81], beside many other techniques to enhance stiffness-to-weight ratio by introducing high performance pseudo-ductile (HiPerDuCT) composites utilizing only FRP composite materials [83]. A schematic illustration of 2D- and 3D-FML beams are shown in Figure 2.2.

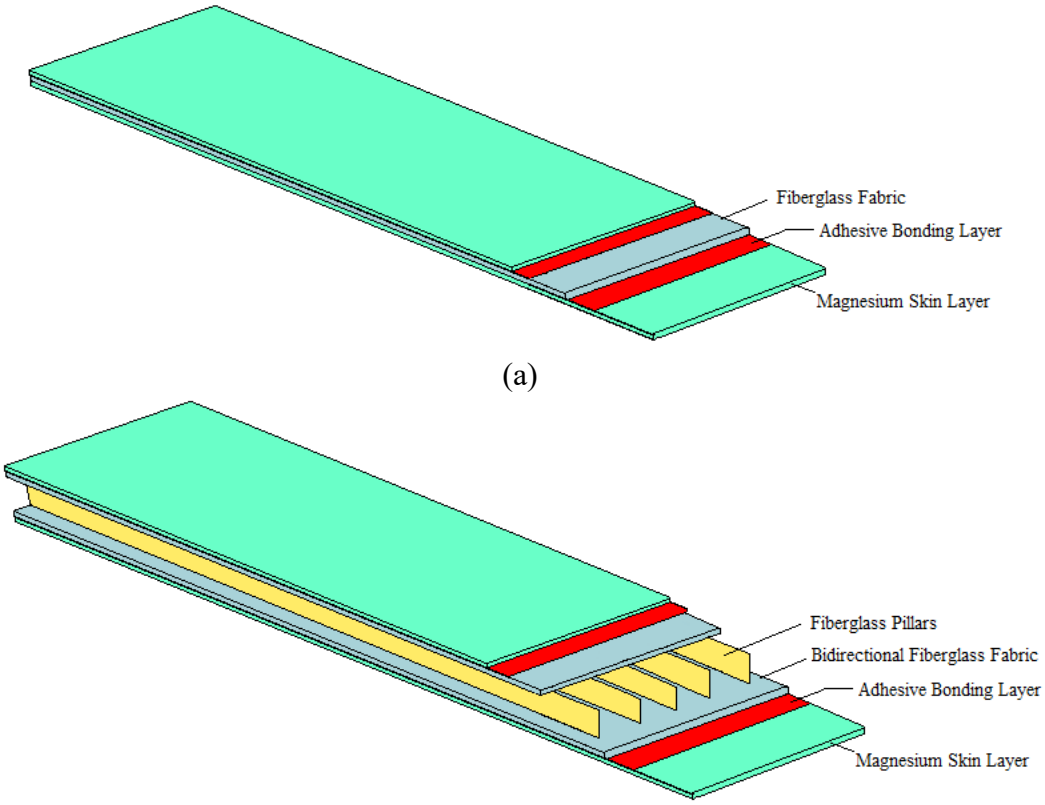

Figure 2.2 Schematic illustration of (a) 2D-FML and (b) 3D-FML beams.

2.5 Finite Element Modeling

To design structural components, it is vital to accurately evaluate and analyze mechanical characteristics of the structure under given loading scenarios, and to estimate approximate failure limit. There are two fundamental mathematical approaches for carrying out analyses: closed-form solutions (i.e., analytical methods) and numerical methods (e.g., FEM). With the advancement in numerical modeling the accurate prediction of the behavior of FMLs has greatly improved. A very thorough and comprehensive literature review has been presented by Sayyad and Ghugal, providing broad insight regarding analytical and numerical analyses of free vibration of composite materials [84].

The finite element method can be used to solve free vibration problem of laminated composites and sandwich plates based on higher order shear and normal deformation theory [35,85,86]. As it was mentioned earlier, Tu et al. [36] formulated a finite element approach to model the vibration and bending characteristics of laminated and sandwich composite plates using a nine-node rectangular element formulated based on a higher-order shear-deformation theory, thereby accounting for the variation of the through-the-thickness shear. Parhi et al. [87] carried out finite element dynamic analysis of laminated composite plates with multiple delamination. De Cicco and Taheri [44] numerically investigated the vibration characteristics of laminated and sandwich composite beams using finite element modeling in LS-Dyna and compared the results with ones obtained experimentally using NDT techniques.

Extensive research has been performed on the effect of nanoparticle reinforcement, static and dynamic properties of polymer composite microbeams, beams and plates, also on static and dynamic properties of non-reinforced FRPs, as well as 2D-FMLs using traditional techniques. However, to the best of the author's knowledge, these subjects have not been studied together as a whole, including 3D-FMLs, and through non-traditional methods. It is worth mentioning that "non-traditional" vibration characterization method refers to testing of structures that are excited using an actuator or external stimulus (this ranges from piezoelectric transducers or accelerators to manual or electrical hammer, etc.) to produce vibrations and then sense/acquire vibration signals to be analyzed later. On the other hand, "traditional" vibration characterization method refers to identifying vibration characteristics of a structure through equivalent (effective) material properties (equivalent (effective) mass and stiffness of homogenized structure) through standard material testing techniques.

It has also been demonstrated that 3D-FMLs would offer comparatively superior stiffness-to-weight ratio to the material systems, thus reducing the overall material weight, thereby lowering the overall cost. Therefore, it was hypothesized that by strategically damping the FML using nano-reinforced polymer composites, one could potentially improve the dynamic response of 3D-FMLs. By providing additional reinforcement using nanoparticles at strategic regions (e.g., matrix, interface, both, etc.), it was postulated that one could optimize the reinforcing effect of nanoparticle on the static and dynamic characteristics of 3D-FMLs, which to the best knowledge of the author had not been attempted previously. The conducted characterizations would help the future researchers to produce a lightweight, cost-effective and resilient system for both static and dynamic loading applications. Therefore, it is important to understand and characterize the static and dynamic response of nano-reinforced polymer composites as the main constituent of the relatively new class of 3D-FMLs. As a result, attempts were made to establish an optimum solution for a new class of material to produce proper static and dynamic performances with the aim of targeting structural applications in transportation industries.

Chapter 3

Parametric Study of Strain Rate Effects on Nanoparticle-reinforced Polymer Composites and Their Dynamic Behavior

3.1 Publication Statement

This chapter has been published as peer-reviewed journal publication in Vol. 2016 of the journal "Nanomaterials" (IF: 1.980; CiteScore: 3.2 (Scopus; 2020)), by B. Soltannia as the 1st author. Its title is "Parametric Study of Strain Rate Effects on Nanoparticle-Reinforced Polymer Composites". It consists of nine double-column pages and was published in 2016 [1]. Note that Sections 3.2 'Nomenclature' and 3.6 'Vibration Response of Pure and NP-reinforced Polymer Composite Beam' and some latter parts of Sections 3.3 'Introduction', 3.7 'Results and Discussion' and 3.8 'Conclusion' are not part of the published article and have been added later to form Chapter 3.

3.2 Nomenclature

α	State variable; controls the level of hydrostatic stress' effect as a state variable
$\dot{\alpha}$	Rate of change of the state variable α
α_0	Initial value of the material constant α
γ_{xz}	Shear strain component
δ_{ij}	Kronecker delta
ε^E	Elastic strain
ε^T	Total strain
ε^I	Inelastic strain
$\dot{\varepsilon}_{ij}^I$	Inelastic strain rate tensor; can be defined as a function of deviatoric stress S_{ij}
$\dot{\varepsilon}_{ij}^{(n+1)}$	Total strain rate
ε_x	Normal strain component

ζ	Natural coordinate
$\theta(x)$	Rotation component
κ	Shear correction factor
ξ	Shape factors
$\tilde{\xi}$	Damping ratio
σ_e	Equivalent (effective) stress
σ_{kk}	Normal stress components
σ_{ij}^n	Initial guess, considered as a value less than the yield stress
σ_x	Normal stress component
τ_{xy}	Shear stress component
ϕ	Nanoparticles volume fraction in the mixture
$\widetilde{\omega}$	Fundamental frequency
$d\mathcal{A}$	Incremental area
$[C_m]$	Stiffness matrix of the polymer
$[\mathcal{C}^{\mathcal{R}}{}_e]$	Rayleigh damping coefficient
D_0	Material constant; represents the maximum inelastic strain rate
d	Diameter of the nanoparticles
E_c	Composite's tangential modulus
E_f	Nanoparticle's modulus of elasticity
E_m	Tangential modulus of neat polymer
$\dot{e}_e^I$	Effective deviatoric inelastic strain rate $\dot{e}_{ij}^I$
$\dot{e}_{ij}^I$	Deviatoric inelastic strain rate
$\{F_e\}$	Force vector
G	Shear modulus
I_1	Mass per length
I_2	Inertia of the section (per unit length)

J_2	Second invariant of the deviatoric stress tensor
$\mathcal{K}$	Kinetic energy
$[\mathcal{K}_e]$	Stiffness matrix
$\mathcal{L}$	Lagrangian functional
l	Length of the nanoparticles
$[\mathcal{M}_e]$	Mass matrix
$\mathcal{N}_{(x)}$	Shape function
n	Material constant; controls the rate dependency of the material
q	Material constant; representing the hardening rate
$\mathcal{R}_a$	The inertial components of Rayleigh damping matrix
$\mathcal{R}_b$	The stiffness components of Rayleigh damping matrix
S_{ij}	Deviatoric stress
t	Thickness of the nanoparticles
$\mathcal{U}$	Strain energy
$u(x)$	Displacement component
$\dot{u}$	General velocity component
$\dot{w}$	General velocity component
Z	State variable
$\dot{Z}$	Rate of change of the state variable Z
Z_0	Initial value of the material constant Z ; equal to magnitude of the stress at the point where the shear stress-strain curve becomes nonlinear

3.3 Introduction

Nanoparticle-reinforced polymer composites (NRPs) are receiving special attention, especially for bonding applications in automotive, marine, aerospace and oil and gas industries. NRPs are known to enhance the mechanical, electrical, thermal, permeability properties and diffusion barrier attributes of their host polymers. Moreover, in some cases, they could also provide self-healing ability. The enactment of mechanical properties gained by the inclusion of nanoparticles includes improved strength and stiffness to weight and cost ratios, improved fatigue and corrosion resistance, more controllable damage mechanism, and augmentation of the energy-absorption capacity of their host polymer. Therefore, these attributed properties render them as effective candidates for reinforcing polymers [88–97].

NRPs are increasingly being used in various engineering applications, especially in the form of adhesives. Adhesives are becoming increasingly more popular for joining structural components because of the recent advancements in techniques used for toughening them. One such emerging technique has been the inclusion of an appropriate amount of inexpensive nanocarbon, namely graphene nanoplatelets (GNP), in resins/adhesives. GNP, which have larger diameter and aspect ratio than their more commonly used nanocarbon tubes counterpart, are less expensive and are more widely available.

One of the thrusts of our current research has been to promote the use of NRPs, in form of adhesives, in automobile applications. In such applications, the NRPs become often subject to large loading rates. Unfortunately, there is a clear paucity in databases that convey the performance of nanoparticle-reinforced adhesives, especially when subject to high loading (or strain) rates. This issue, in turn, has impeded the greater usage of NRPs in such engineering

applications. Therefore, the mechanical characterization of such nano-reinforced adhesives is vital, especially when they are subject to large loading rates.

The use of carbon nanotubes, which are essentially sheets of graphite rolled into tubes [68,69], was first proposed by Iijima in 1991 and later by Iijima and Ichihashi in 1993. Even though CNTs (both single-walled, and multi-walled varieties) are quite flexible in the direction perpendicular to their longitudinal axis [98], the strength and elastic modulus of MWCNTs have been estimated to be as high as 150 GPa and 900 GPa, respectively [72]. Their superior mechanical characteristics and proper length-to-diameter ratio have rendered CNTs as an effective reinforcing agent for resins. Nevertheless, in order to fully harness the exceptional mechanical properties of CNTs, a strong interfacial bond between the polymer matrix and CNTs must exist [99].

Since the advent of nanotechnology, nanoparticle reinforced adhesives have also been increasingly used in many other advanced applications such as naval, automotive, aerospace, and medical industries. Kim and Reneker reported that the Young's modulus of a nanofiber-reinforced composite was ten times greater than that of the neat adhesive [65]. It has also been demonstrated that MWCNT particles enhance the strength and toughness of epoxies, because nano-particles strengthen the polymeric chains of the resin and resist crack initiation and propagation by acting as bridges [100]. Qian et al. suggested that nanotubes (CNTs) could enhance the composite strength by as much as 25% [73]. It should also be noted that a nanoparticle-reinforced adhesive with the most optimum properties can only be produced if the nanoparticles are distributed uniformly and fully dispersed (exfoliated) within the polymer. This is a very challenging process, because the formation of agglomerations can act as defect regions, thus reducing the performance instead of enhancing it.

Despite the noted studies, to date, there are only a limited number of studies that have explored the mechanical properties of resins reinforced with carbon nanoparticles, especially GNP. Moreover, the lack of such studies becomes even more noticeable when one requires information on the effect of loading/strain rates on the response of nanoparticle reinforced resins.

Therefore, in order to better understand the mechanical behavior of the nanoparticle-reinforced polymer composites under dynamic loading conditions (hence, to be able to establish and assess the safety factor of the structure hosting NRPs), one should gain a better understanding of the mechanical response of such resins under different strain rates. Several researchers have demonstrated the rate-dependent mechanical behavior of neat polymers, and have developed constitutive models for their characterization (see, for instance [101–109]). Notwithstanding the abovementioned studies and those alike, there exists no unified and robust theoretical approach capable of mimicking the atomic interaction between nanoparticles and polymers. The involved challenges in constructing such a model have therefore necessitated the use of multi-scale techniques to identify the macroscale mechanical behavior of nanoparticle-reinforced polymer composites. An example of such modeling approach can be found in the work of Shokrieh et al. [110]. They incorporated a strain rate dependent continuum-based macroscale level constitutive model developed by Goldberg et al. [104–106], combined with the Halpin-Tsai micromechanical model [111], to study the loading rate effects on a CNT-reinforced polymer composite.

Another important aspect of NRP's mechanical behavior is their vibration response. To fundamentally study the vibration response of such composite material, free vibration analyses of a continuous beam with free-free boundary condition is required to be investigated. The mathematical model of such beam was developed by Sharma et al. using Euler- Bernoulli beam theory to determine the natural frequency of the beam [112]. In addition to Euler-Bernoulli model,

different engineering theories can be used to investigate dynamic characteristics of a vibrating beam e.g., Rayleigh, Timoshenko, and shear theory, i.e., Al-Ansari et al. identified the natural frequency of a stepped cantilever beam using Rayleigh and modified Rayleigh models as well as Finite Element Analysis (FEA) using ANSYS® [113]. Closed form solution for free vibration of a beam with free-free (F-F) boundary condition (BC) has been examined by Sharma [114] and Cresta [115]. Dynamic behavior of the Timoshenko beam with simply-supported (S-S) BCs was discussed by Reddy, using finite element approach [116]. He observed that the reduced integration element with adequate number of elements can estimate the natural frequencies precisely. Younesian et al. classified various linear and nonlinear vibration modeling and applications of different structures e.g., string, beam, plate, shell structures with different boundary conditions resting on elastic and viscoelastic foundations [117]. Rajoria and Jalili experimentally investigated passive vibration damping of CNT-reinforced composite cantilever beams with structural vibration applications [118]. They observed a 700% increase in damping ratio for multi-walled nanotube-epoxy beam compared to the plain epoxy beam. They also found out that enhancement in damping ratio using carbon nanotube reinforcement is more dominant than enhancement in stiffness. They also reported that MWCNT-reinforcement was superior to SWCNT-reinforcement. Shokri-Oojghaz et al. studied the stress distributions of Aggregated Carbon Nanotube (A-CNT)-reinforced nanocomposite sandwich cylinders under internal and external pressures, using a finite element method (FEM) based on an axisymmetric model [119]. Mirzaalian et al. studied bending behavior of sandwich plates with aggregated CNT-reinforced face sheets as functionally-graded material (FGM), resting on Winkler-Pasternak elastic foundation using a mesh-free method based on first order shear deformation theory (FSDT) [120], which can be simplified and used to identify deflection and time dependent behavior of a homogenous beam resting on Winkler-Pasternak

elastic foundation (implying F-F BC). They employed moving least square (MLS) shape functions in their mesh-free analysis to estimate the displacement. They also used transformation method to impose the essential BC. They observed FG-distribution of aggregation leads to less deflection of the sandwich plates. Moradi-Dastjerdi et al. also investigated damped dynamic behavior (deflection) of an advanced (GNP-FG) piezoelectric sandwich plate (APSP) under thermo-electro-mechanical loads using MLS shape functions in meshless solution [121]. They observed that increase in stiffness and inertial components of structural damping significantly reduce the settling time of vibrations such that among Rayleigh's structural damping coefficients, R_b is more sensitive to change than R_a. Their results also revealed that more voids in the core layer greatly mitigates amplitude of vibration and damping ratio. They also found that increasing the volume fraction of GNP from 3% to 7% significantly affects the damping ratio, settling time and dynamic responses, however further increase had less influence. Further, Mohammadimehr et al. studied free and forced vibration of uniformly and FG SWCNT reinforced viscoelastic microcomposite beam using modified couple stress theory (MCST) [122]. They used energy method and Hamilton's principle to obtain the governing equation of motion (EoM). They employed the Kelvin-Voigt model to account for material's viscoelasticity. They observed that neglection of structural damping coefficients in presence of external periodic force causes vibration amplitude to increase resulting in loss of beam's stability. In contrast to Rajoria and Jalili [118], Mohammadimehr et al. [122] concluded that natural frequency of SWCNT-reinforced composite beam was higher compared to those reinforced by MWCNT. Bouamama et al. conducted dynamic stability analysis of FG Timoshenko beams based on Kelvin-Voigt model accounting for internal viscous damping distribution (DIVD) [123]. They used Lagrange principle to develop their governing EoM, discretized and solved to find natural frequencies and damped eigenfrequencies of the material

system using FEM. They found that the damped frequencies are inversely proportional to internal damping coefficient. The slenderness ratio (L/h) has noticeable effect on variation of the damped fundamental frequencies.

In this chapter, using a similar approach adopted by Shokrieh et al. [110], the effects of nano-reinforcement on the mechanical response of a nano-reinforced resin, subjected to different strain rates are modeled and systematically investigated. More specifically, neat and nano-reinforced resins are subjected to tensile loadings applied at the rates of 1.5, 15, 150, and 1500 mm/min. Further, the influence of various parameters (i.e., the particle type, their weight percentage) on the mechanical properties of the nanocomposite was studied. Further, the numerical results are compared to the experimental data obtained for the neat and the nano-reinforced epoxy resins [124,125]. Finally, free vibration analysis of a continuous Timoshenko beam made of aluminum, pure and GNP-reinforced epoxy resin (unidirectional (UD) case of FG beam) with free-free boundary condition is carried out using Rayleigh structural method, discretized and solved by FEM.

3.4 Experimental Investigation

3.4.1 Materials and Specimen Preparation

A commonly used thermoset epoxy resin (i.e., the West System 105 resin and 206 hardener [Bay City, MI]), was used as the baseline adhesive to fabricate the test specimens. This resin was selected because it is a commonly used resin, has a relatively low-cost, and is readily available.

In order to establish a cost-effective means for enhancing the mechanical properties of the resin/adhesive, different types of nano-carbon particles were utilized as the reinforcing agent. However, the uniform distribution, and dispersion of nano-carbon particles in resin were found to

be quite time-consuming and challenging, hence increasing the processing cost. It should be noted that not only do the distribution and dispersion of particles directly influence adhesive's mechanical properties, but more importantly, the nano-particle agglomeration results in significant statistical discrepancies in performance of the final product.

Three different forms of nano-carbon particles were chosen to be dispersed into the epoxy resin.

(i) Graphitized Carbon Nanofibers (CNF) with an outer diameter of 200 to 600 nm (reported by the manufacturer; 4 μm in current study (this can be attributed to aggregation of the NFs alongside each other) and more than 99.9 % purity (obtained from the US Research Nanomaterials, Inc., Houston, TX).

(ii) Graphene nanoplatelets (GNP-M-25) with an average diameter of 25 μm (reported by the manufacturer; 25 nm to 1 μm reported in the literatures [67,126]; and 0.5 μm in current experiments and analyses which can be attributed to particles breaking into smaller pieces due to milling process), thickness of 6 nm (reported by manufacturer; 34 nm in current experiments and analyses which can be due to piling/stacking of NP on top of each other), and surface area of 100 m^2/g (obtained from XG Science Ltd., Lansing, MI).

(iii) Multi-Walled Carbon Nanotubes (MWCNTs) with an outer diameter of 5 to 15 nm (provided information by the manufacturer. The outer diameter of MWCNTs used in current experiments and analyses was 20 nm) and more than 95% purity (obtained from the US Research Nanomaterials, Inc., Houston, TX).

To facilitate uniform dispersion of the nanoparticles in resin, a mechanical stirrer was used first. Each slurry of resin/nanoparticle was stirred at a speed of 2000 rpm for 10 min. This procedure was followed by calendering the resin/nanoparticles mix with a three-roll mill. The calendering rollers' speed was set to the machine's maximum rotational speed of 174 RPM. To

maximize dispersion quality and minimize agglomerations, the calendering was performed seven times. The roller gaps were set at 20 μm. Note that, concentrations of CNF, MWCNT, and GNP with weight percentages of 0.25%, 0.5% and1% were considered. It should be noted that selection of the rollers gap size is quite important. It is postulated that when the nanoparticles are dispersed into adhesives, they are surrounded by monomer molecules. After each round, the quality of the distribution and dispersion was monitored by sampling the mixed slurry and assessing the uniformity of the dispersion with a digital microscope.

The subsequent addition of the curing agent would initiate the chemical reaction process of the resin, promoting the monomer molecules to surround the GNP as the resin cures. In addition to the mechanical bonding, chemical bonding known as Van der Waals bond is also generated. The inclusion of nano-particles into resin also increases resin's viscosity (thickens it). It should also be noted that in comparison to other types of nanoparticles (e.g., CNFs or CNTs), the relatively greater aspect ratio of GNP helps to increase the resin/nanoparticles interactions, thus forming a tougher adhesive.

Following the aforementioned procedures, the curing agent (hardener) was added to the slurry and mixed using a stirrer at a speed of 400 rpm for 4 to 6 minutes. The mixture was then degassed under 28″ Hg vacuum for 2 to 3 minutes (the degassing time period depends on the gel time of the resin). After degassing, the mixture was poured into appropriately designed and fabricated molds and allowed to cure for at least 12 hours at room temperature. The final products in the form of dog-bone tensile coupons with dimensions as per ASTM D638, for both neat and nanoparticle-reinforced resins are shown in Figure 3.1 [127].

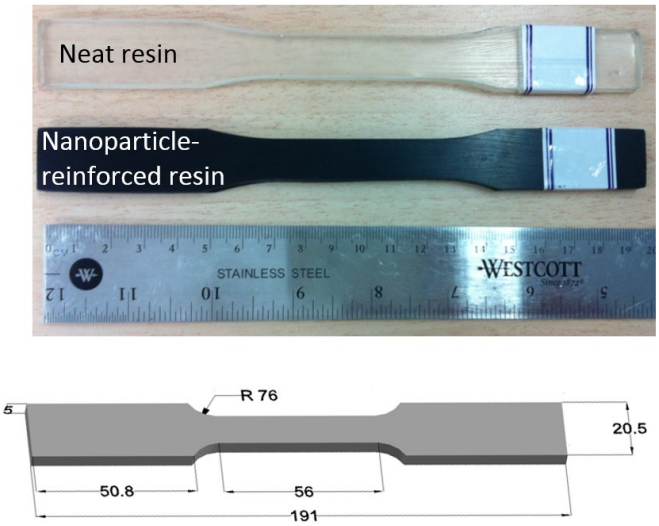

Figure 3.1 Representative tensile coupons of the neat and nanoparticle reinforced epoxy resins, and their dimensions (in mm). "R" stands for radius.

3.4.2 Characterization of the Mechanical Properties of Adhesives

The prepared dog-bone shaped samples were tested in tension using an Instron servo-hydraulic universal test machine equipped with 8500^{+} electronics. To establish the stress-strain characteristics of the neat and nano-reinforced resins, the specimens were subjected to a displacement-controlled tensile loading [127]. First, tensile tests were performed on the neat resin at room temperature, at cross-head speeds of 1.5, 15, and 150 mm/min, per ASTM D 897 (as the baseline tests for the static and quasi-static loading conditions), as well as at 1500 mm/min, per ASTM D 950 (as the baseline tests for the high-strain rate loading condition) [128,129]. Subsequently, the reinforced-adhesive specimens underwent testing with the same loading rates. The gauge-length displacement of specimens tested under quasi-static loading rates (1.5 mm/min), was recorded using an Instron extensometer (Instron Industrial Products, Grove, PA) as well as an EIR Laser Extensometer (Electronic Instrument Research, Irwin, PA). An Instron dynamic extensometer and the laser extensometer were used to record the gauge-length displacement of the specimens tested under the quasi-static, and higher loading rate experiments (i.e., 15, 150, 1500 mm/min), as shown in Figure 3.2. Using the recorded load and gauge length displacement, the

stress-strain curve of each adhesive was constructed and their elastic modulus evaluated. The initial gauge length for all cases was 25.4 mm.

(a) (b)

Figure 3. 2 Experimental setup for the (a) static; (b) quasi-static and higher loading rate tests.

The experimental results revealed that not only did the inclusion of nanoparticles improved the mechanical properties of the adhesive, but it also enhanced the resin's viscosity. The improved viscosity renders the adhesive suitable for use in adhesively bonded joints that oriented vertically, which are often encountered in several industrial applications, especially in marine and other applications where relatively thick bond-lines are commonly used [124,125].

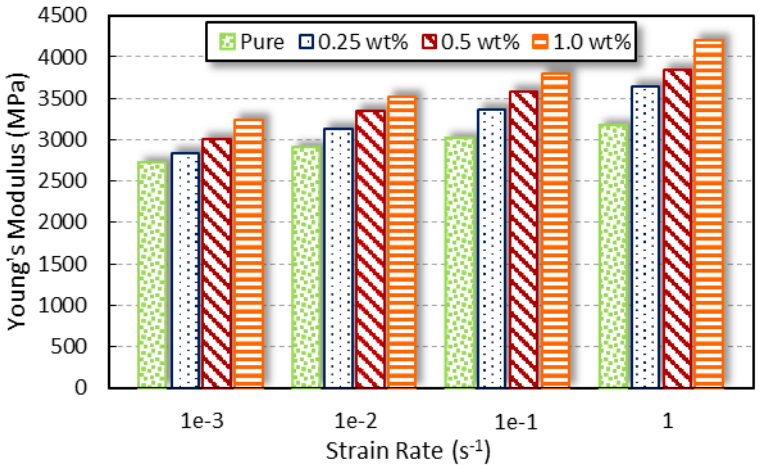

Figure 3.3 Influence of strain rate, on the tensile elastic modulus of the epoxy resin reinforced with various amounts (wt%) of GNP.

Figure 3.3 shows that the inclusion of nanoparticles has the same effect as the increasing of the strain rate, which means by increasing the amount of dispersed nanoparticles the stiffness of the matrix has been enhanced. The same results can be seen as a result of increasing the strain rate.

3.5 Problem Statement and Modeling Strategy

The rate-dependent mechanical behavior of nanoparticle-reinforced polymers has been studied by different researchers. Nonetheless, to the best of the authors' knowledge, there exists a clear lack of coherent and comprehensive parametric studies that have either theoretically or experimentally characterized the effects of nanoparticle types, their weight-content and strain rates on their response. Therefore, in this work, the macroscale rate dependent constitutive equation of Goldberg et al. [104–106] will be modified by incorporating the Halpin-Tsai micromechanical model [111], including the inclusion of more specific shape factors, in order to assess the influence of different strain rates on the response of a polymer reinforced by different types of nanoparticles with various weight-content. The predicted results obtained through the aforementioned superposition technique (as incorporated by Shokrieh et al. [110]), will be validated with the experimental results. At this juncture, it should be noted that one could equally adopt other micromechanical modeling techniques (such as that developed by Mori-Tanaka [91,93], or others), in place of the Halpin-Tsai model used in this study.

3.5.1 Strain Rate Dependent Continuum-based Constitutive Equation of Polymers

Various researchers [102,104–106] have shown that the stress-strain response of nanoparticle-reinforced polymer composites is dominated by the nonlinear response of its main constituent. In order to determine the viscoelastic-viscoplastic response of the polymer, the total strain $\left(\varepsilon^{T}\right)$ can be decomposed into elastic $\left(\varepsilon^{E}\right)$, and inelastic $\left(\varepsilon^{I}\right)$ components. Analogously, the inelastic strain can be calculated as the difference of the total strain and elastic strain.

Goldberg et al. [104–106] proposed a model for predicting the viscoplastic response of neat polymers, utilizing a set of state variables as an indication of the resistance of polymeric chains against flow. It should also be mentioned that polymer's mechanical properties and loading/strain rate are the two main parameters that govern the nonlinear response of the polymer. The inelastic strain components can be expressed in terms of the deviatoric stress components as follows[102,104–106]:

$$\dot{\varepsilon}_{ij}^{I} = 2D_0 \exp\left[-\frac{1}{2}\left(\frac{Z}{\sigma_e}\right)^{2n}\right]\left(\frac{S_{ij}}{2\sqrt{J_2}} + \alpha\delta_{ij}\right) \tag{3.1}$$

where, $\dot{\varepsilon}_{ij}^{I}$ is the inelastic strain rate tensor which can be defined as a function of deviatoric stress; J_2 is the second invariant of the deviatoric stress tensor, and Z and α are the state variables. Z is the internal stress state variable that represents the resistance to molecular flow (internal stress), and α is the hydrostatic stress effect state variable. Moreover, D_0 and n are material constants; D_0 represents the maximum inelastic strain rate and n controls the rate dependency of the material. The equivalent (effective) stress, also be defined as a function of the mean stress, such that the summation of the normal stress components σ_{kk} is three times of the mean stress, as follows:

$$\sigma_e = \sqrt{3J_2} + \sqrt{3}\alpha\sigma_{kk} \tag{3.2}$$

where, α controls the level of hydrostatic stress' effect as a state variable. The term $\dot{e}_e^I$ represent the effective deviatoric inelastic strain rate $\dot{e}_{ij}^I$.

$$\dot{e}_e^I = \sqrt{\frac{2}{3}\dot{e}_{ij}^I\dot{e}_{ij}^I} \tag{3.3}$$

$$\dot{e}_{ij}^I = \dot{\varepsilon}_{ij}^{\,I} - \frac{\dot{\varepsilon}_{kk}^I}{3}\delta_{ij} \tag{3.4}$$

The rate of change of the other two-state variables, Z and α, can be determined using the following evolution equations:

$$\dot{Z} = q\left(Z_1 - Z\right)\dot{e}_e^I \tag{3.5}$$

$$\dot{\alpha} = q\left(\alpha_1 - \alpha\right)\dot{e}_e^I \tag{3.6}$$

Here, q is a material constant, representing the hardening rate, which is determined through trial and error, based on the inelastic shear strain attaining a plateau, or the tensile strain corresponding to the saturation region of the stress-strain curve. Z_1, α_1 are material constants, representing the maximum values of Z and α. Z_0 and α_0 are the initial values of the material constants Z and α. Z_0 is the magnitude of the stress at the point where the shear stress-strain curve becomes nonlinear. α_0 and α_1 are defined using equation (3.2) and tensile stress-strain, and shear stress-strain curves (the values of stress at the plateau and first nonlinearity points of the stress-strain curves, respectively).

The material constants Z_1, Z_0, α_1, α_0, n, and D_0 can be determined using the shear stress-strain and tensile or compression stress-strain curves, obtained by experiments conducted under constant strain rates on neat polymers. Empirically, it has been shown that the value of D_0, quantitatively, can be set equal to 10^4 times the maximum applied total strain rate; qualitatively, it is the restricting (controlling) value of the inelastic strain rate. The values of n, Z_1 can be identified using the shear stress-strain curves constructed under various strain rates. The plateau region of the effective stress under a uniaxial tensile loading at a particular strain rate, corresponds to the saturation region of the effective stress obtained under pure shear loading.

To solve the implicit Goldberg constitutive equation (3.1), one should utilize an appropriate numerical discretization technique. Moreover, one should ensure that the selected technique for solving the equation would be stable. For that, the four-step Runge-Kutta (R-K-4) method is adopted and implemented in this work, which is similar to the procedure that was first proposed by Tabiei and Aminjikarai [130,131], and was also used by Shokrieh et al. [110]. The numerical representations of equation (3.1), (3.5) and (3.6) take the following incremental forms after multiplying the rate dependent equation by the time step (dt):

$$d\varepsilon_{ij}^{I} = \left(2D_0 \exp\left[-\frac{1}{2}\left(\frac{Z}{\sigma_e} \right)^{2n} \right] \left(\frac{S_{ij}}{2\sqrt{J_2}} + \alpha\delta_{ij} \right) \right) dt \tag{3.7}$$

$$de_{ij}^{I} = d\varepsilon_{ij}^{I} - \frac{d\varepsilon_{kk}^{I}}{3}\delta_{ij} \tag{3.8}$$

$$de_{e}^{I} = \sqrt{\frac{2}{3} de_{ij}^{I} de_{ij}^{I}} \tag{3.9}$$

$$dZ = q\left(Z_1 - Z\right) de_{e}^{I} \tag{3.10}$$

$$d\alpha = q\left(\alpha_1 - \alpha\right) de_{e}^{I} \tag{3.11}$$

As in any forward numerical method, the parameters' values from a previous step are available to be used as an input in the subsequent step. Therefore, usually a value less than the yield stress is considered as the initial guess for σ_{ij}^{n} to start the numerical integration. Another given input parameter is the total strain rate, $\dot{\varepsilon}_{ij}^{(n+1)}$, which can be described as:

$$\varepsilon_{ij}^{(n+1)} = \varepsilon_{ij}^{(n)} + \varepsilon_{ij}^{(n+1)} dt \tag{3.12}$$

As the first-time step of the R-K-4, values of $\sigma_{ij} = \sigma_{ij}^{m(0)}$, $Z = Z^{m(0)} = Z_0$, $\alpha = \alpha^{m(0)} = \alpha_0$ are considered as the input parameters (note: the superscript "*m*" refers to the matrix). For an initial

guess, the magnitude of $\sigma_{ij}^{m(0)}$ is selected such that it is less than the material's yield strength. One can then determine the values of $d\varepsilon_{ij}^{I1}$ by substituting the values of Z_0 and α_0 into equation (3.7). As a result, based on equations (3.4), (3.7), (3.9)-(3.11), the first step of the R-K-4 can be represented as follows:

$$d\varepsilon_{ij}^{I(step1)} = d\varepsilon_{ij}^{I}, \quad dZ^{(step1)} = dZ, \quad d\alpha^{(step1)} = d\alpha \tag{3.13}$$

$$\varepsilon_{ij}^{I} = \varepsilon_{ij}^{I(n)} + \frac{1}{2} d\varepsilon_{ij}^{I(step1)} \tag{3.14}$$

$$\{\sigma\} = [C_m]\left(\{\varepsilon\}^{n+1} - \{\varepsilon\}^{I}\right) \tag{3.15}$$

$$Z = Z^{m(n)} + \frac{1}{2} dZ^{(step1)} \tag{3.16}$$

$$\alpha = \alpha^{m(n)} + \frac{1}{2} d\alpha^{(step1)} \tag{3.17}$$

where $[C_m]$ is the stiffness matrix of the polymer, and the stress can be determined based on elastic and inelastic strain's constituents. The remaining steps of the R-K-4 procedure are shown in Appendix I.

3.5.2 The Halpin-Tsai Micromechanical Model

There are different micromechanical models available for characterizing the elastic behavior of nanoparticle-reinforced polymer composites under static loading condition. The models developed by Halpin-Tsai, Mori-Tanaka, Nielsen, to mention a few [91–93]are some examples. The Halpin-Tsai model [91–93] used in this work can be expressed in the following form:

$$\frac{E_c}{E_m} = \frac{1+\xi\eta\phi}{1-\eta\phi} \qquad \text{where,} \quad \eta = \left(\frac{E_f}{E_m} - 1\right)\left(\frac{E_f}{E_m} + \xi\right)^{-1} \tag{3.18}$$

where, E_c is the composite's tangential modulus, which can be determined by another equation developed by Halpin and Tsai [111], E_m is the tangential modulus of neat polymer, determined using the predicted stress-strain curve as described in the previous section, and E_f is the nanoparticle's modulus of elasticity. Moreover, ϕ is the nanoparticles volume fraction in the mixture. Depending on the nanoparticles type, different shape factors, ξ, would have to be used (i.e. for oriented discontinuous polymer composites $\xi_{GNP}^{II} = 2\left(\frac{l}{t}\right)$, where l is the length of nanoparticles (NPs) in the 1st-direction and t is the thickness of the NPs in the 3rd-direction; $\xi_{GNP}^{\perp} = 2$ for circular or square-shape NPs, where their $w = t$ in $\xi_{GNP}^{\perp} = 2\left(\frac{w}{t}\right)$ where, where w is the width of the NPs in the 2nd-direction; and $\xi_{CNT} = 2\left(\frac{l}{d}\right)$, where d refer to the diameter of the NPs) [111].

In the following section, the abovementioned techniques will be employed to establish the integrity of the proposed models and solution scheme. For that, first the stress-strain response of the neat resin will be predicted. That will be followed by a parametric study that will assess the strain-rate effects on the nanoparticle-reinforced epoxy resin. To calculate the stress-strain of nanoparticle-reinforced polymer composite, first the global stress-strain curve of the neat resin is predicted using the Goldberg model [104–106]. Then, the tensile tangent moduli of the pure polymer in appropriate strain intervals are determined, sequentially. Subsequently, the tangent moduli of the nanoparticle-reinforced resin are evaluated at each strain interval by modifying the obtained tangential moduli of the pure polymer using the Halpin-Tsai equation. As a result, the stress corresponding to each strain interval can be determined for the nanoparticle-reinforced resin.

Finally, after establishing the stress values, one would be able to establish the global stress-strain curve.

3.6 Vibration Response of Pure and NP-reinforced Polymer Composite Beam

In this section, the vibration response of a continuous Timoshenko beam made of aluminum, pure epoxy, and NRP with free-free boundary condition, as it is shown in Figure 3.4, is studied using finite element method (FEM), considering Rayleigh structural damping.

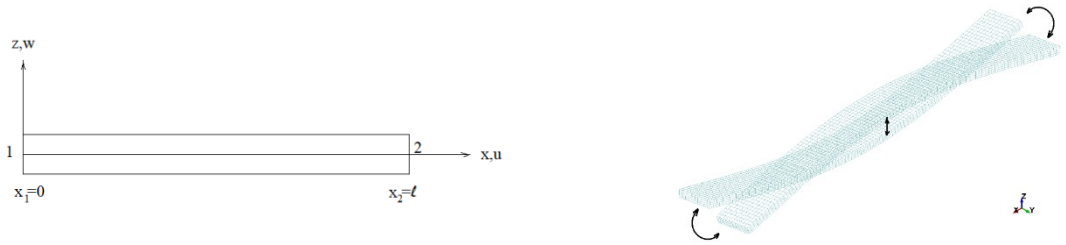

(a) (b)

Figure 3.4 (a) Two dimensional illustration of a Timoshenko beam with free-free boundary condition; (b) Three dimensional illustration of first mode of longitudinal bending vibration of isotropic beam with free-free boundary condition, undergoing free vibration.

3.6.1 Governing Equation of Motion

The governing EoM for a Timoshenko beam can be obtained by applying the Hamilton principle to the Lagrangian $\mathcal{L}$ [121,123]:

$$\delta \int_{t_0}^{t_1} (\mathcal{L})\, dt = \delta \int_{t_0}^{t_1} (\mathcal{K} - \mathcal{U})\, dt = 0 \tag{3.19}$$

where, $\mathcal{K}$ and $\mathcal{U}$ denote the kinetic and strain energies of an elastodynamic system.

The kinetic energy can be expressed as follows:

$$\mathcal{K} = \frac{1}{2} \int_{\mathcal{V}} \rho_{(z)} (\dot{u}^2 + \dot{w}^2) d\mathcal{V} \tag{3.20}$$

where, $\dot{u}$ and $\dot{w}$ are the velocity components of the beam along the x and z axes, respectively; $\rho_{(z)}$ is the mass per unit volume.

After applying the displacement fields $w(x,z,t) = \tilde{w}(x,t) = w$, $u(x,z,t) = z\frac{\partial \tilde{u}_{(x,t)}}{\partial x} = z\theta$, Equation (3.20) takes the following form:

$$\mathcal{K} = \frac{1}{2}\int_0^{\ell}\left[I_1\dot{u}^2 + I_2\dot{\theta}^2\right]dx \tag{3.21}$$

where,

$$(I_1, I_2) = \int_A \rho_{(z)}(1, z^2)d\mathcal{A} \tag{3.22}$$

where, I_1, I_2 are the mass per length, and inertia of the section (per unit length), respectively, and $d\mathcal{A}$ is the incremental area.

Strain energy can be expressed as: $U = {}^1\!/_2 \int_{\mathcal{V}} \sigma_x\varepsilon_x\, d\mathcal{V} + {}^1\!/_2 \int_{\mathcal{V}} \tau_{xz}\gamma_{xz}\, d\mathcal{V}$ (3.23)

where, in our case, $\varepsilon_x = \frac{du}{dx} = z\theta_{z,x}$; $\gamma_{xz} = \frac{\partial u}{\partial z} + \frac{\partial w}{\partial x} = \theta_z + w_{,x}$ are the strains

and $\sigma_x = E\varepsilon_x$; $\tau_{xz} = \kappa G\gamma_{xz}$ are the stresses, in which $G = \frac{E}{2(1+\vartheta)}$; $\kappa = \frac{5}{6}$ where κ is the shear correction factor [132].

Rewriting Equation (3.23) yields:

$$U = {}^1\!/_2 \int_0^{\ell} EI_z\,\theta_{z,x}^2\, dx + {}^1\!/_2 \int_0^{\ell} \kappa AG\left(w_{,x} + \theta_z\right)^2 dx \tag{3.24}$$

Using Equations (3.21) and (3.24), Equation (3.19) takes the following form:

$$\frac{1}{2}\int_{t_0}^{t_1}\int_0^{\ell}\left[I_1\dot{u}^2 + I_2\dot{\theta}^2 - \left(EI_z\theta_{z,x}^2 + \kappa AG\left(w_{,x} + \theta_z\right)^2\right)\right]dx\,dt = 0 \tag{3.25}$$

3.6.2 Finite Element Modeling

Equation (3.25) can be solved using FEM with a variation of displacement $w(x)$ and rotation $\theta(x)$, implying four degrees of freedom (DoF) in each element (two DoF per node), as it is shown in Figure 3.5 [133].

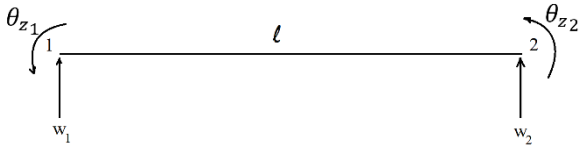

Figure 3.5 Timoshenko beam element: degrees of freedom of the two-noded element.

Hence, the nodal displacement vector has the following generic form:

$$\begin{Bmatrix} w \\ \theta \end{Bmatrix} = [\mathcal{N}_{(x)}]\left\{U_{e_{(t)}}\right\} = \begin{bmatrix} \mathcal{N}_{1_{(x)}} & 0 & \mathcal{N}_{2_{(x)}} & 0 \\ 0 & \mathcal{N}_{1_{(x)}} & 0 & \mathcal{N}_{2_{(x)}} \end{bmatrix} \begin{Bmatrix} w_1 \\ \theta_1 \\ w_2 \\ \theta_2 \end{Bmatrix} \tag{3.26}$$

where, $\mathcal{N}_{1_{(x)}} = \left(1 - \frac{\zeta}{\ell}\right)$, and $\mathcal{N}_{2_{(x)}} = \left(1 + \frac{\zeta}{\ell}\right)$ are the shape functions, and $-1 \leq \zeta \leq 1$ resembles the natural coordinate.

Substituting Equation (3.26) into Equation (3.25), the EoM takes the following general form:

$$[\mathcal{M}_e]\left\{\ddot{\mathcal{U}}_{e_{(t)}}\right\} + [\mathcal{C}^{\mathcal{R}}{}_e]\left\{\dot{\mathcal{U}}_{e_{(t)}}\right\} + [\mathcal{K}_e]\left\{\mathcal{U}_{e_{(t)}}\right\} = \left\{F_{e_{(t)}}\right\} \tag{3.27}$$

where, $[\mathcal{M}_e] = \int_{-1}^{1} l\rho A N^T N \, d\zeta + \int_{-1}^{1} l\rho I_z N^T N \, d\zeta$, is the Mass matrix;

$[\mathcal{C}^{\mathcal{R}}{}_e] = \mathcal{R}_a[\mathcal{M}_e] + \mathcal{R}_b[\mathcal{K}_e]$, is the Rayleigh damping matrix, with $\mathcal{R}_a$ and $\mathcal{R}_b$as are the inertial and stiffness components of Rayleigh damping matrix, respectively [121];

Equation (3.28) shows how $\mathcal{R}_a$ and $\mathcal{R}_b$ can be related to the fundamental frequency and damping ratio [134–136]:

$$\tilde{\xi} = \frac{\mathcal{R}_a}{2\tilde{\omega}} + \frac{\mathcal{R}_b\tilde{\omega}}{2} \tag{3.28}$$

where, $\tilde{\xi}$ is damping ratio and $\tilde{\omega}$ is the fundamental frequency.

$[\mathcal{K}_e] = \int_{-1}^{1} \frac{EI_z}{l^2}\left(N_{,\zeta}^T\right)\left(N_{,\zeta}\right) l\, d\zeta + \int_{-1}^{1} \kappa AG \left(\frac{1}{l}N_{,\zeta} + N\right)^T \left(\frac{1}{l}N_{,\zeta} + N\right) l\, d\zeta$, is the stiffness matrix; and, $\{F_e\} = l \int_{-1}^{1} N^T\, d\zeta$, is the force vector.

Matlab codes used to obtain the transient response of 200 mm × 20 mm × 3.5 mm (length × width × height) beams made of aluminum, pure and NP-reinforced epoxy resin are shown in Appendix III [133,134,137–141].

3.7 Results and Discussion

In this section, we discuss the integrity and accuracy of the developed SRDM model introduced in Section 4.5, for predicting the tensile stress-strain response of the neat epoxy resin reinforced with various nanoparticles. For that, first by following the steps noted in section 4.5, and those in Appendix I, the stability of the iterative R-K-4 numerical procedure for establishing the tensile stress-strain response of the neat resin under an arbitrary strain rate is tested, with the results illustrated in Figure 3.6. As can be seen, three different time-steps, *dt*, were selected for this task.

As seen and anticipated, smoother and more continuous curves are obtained as the value of time step is deceased, and the numerical convergence is clearly evident. To establish the rate dependent material constants, the experimental results of the tensile tests conducted under quasi-static loading rate of 150 mm/min (=10^{-1} s^{-1}) (load rate / (gauge length * 60 sec). The loading rates can be easily converted into strain rates, considering the fact that initial gauge length is 25.4 mm. Therefore, strain rate can be obtained by dividing the load rate to multiplication of initial gauge

length and 60 seconds. The rate dependent material properties of the neat epoxy are provided in Table 3.1.

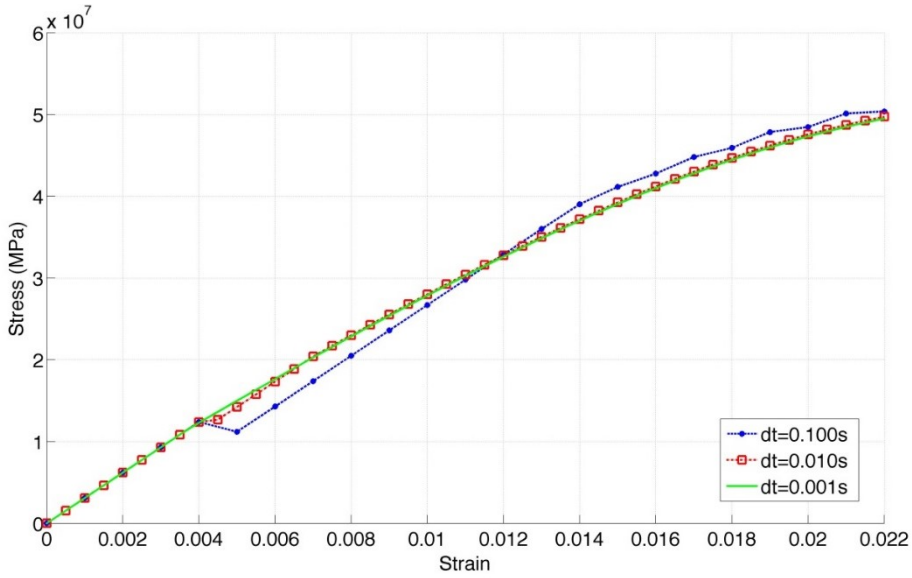

Figure 3.6 Influence of the time steps (dt) on the numerical stability of the adopted iterative procedure used for predicting the stress-strain curves of the neat WS-105 epoxy resin at an arbitrary strain rate

Table 3.1 Calculated rate dependent material constants of WS-105 epoxy resin.

Material	Strain Rate (s^{-1})	Tangential Modulus (GPa)	Poisson's Ratio	$D_0(s^{-1})$	n	$Z_0(MPa)$	$Z_1(MPa)$	q	α_0	α_1
WS-105 epoxy	1×10^{-3} 1×10^{-2} 1×10^{-1} 1	3.1	0.3	$5\square10^{6}$	0.745	200	1130	610	0.202	0.430

Due to the nonlinear behavior of nanoparticle-reinforced polymer composites, the value of the constant linear modulus should be replaced by the tangential modulus. To establish the strain rate dependent response of the resin reinforced with different nanoparticles, and their resulting response to different strain rates, first the instantaneous tangential modulus of the neat resin under

quasi-static strain rate (10^{-1} s^{-1}) is established. Figure 3.7 illustrates the variation of the tangential tensile modulus of the neat resin.

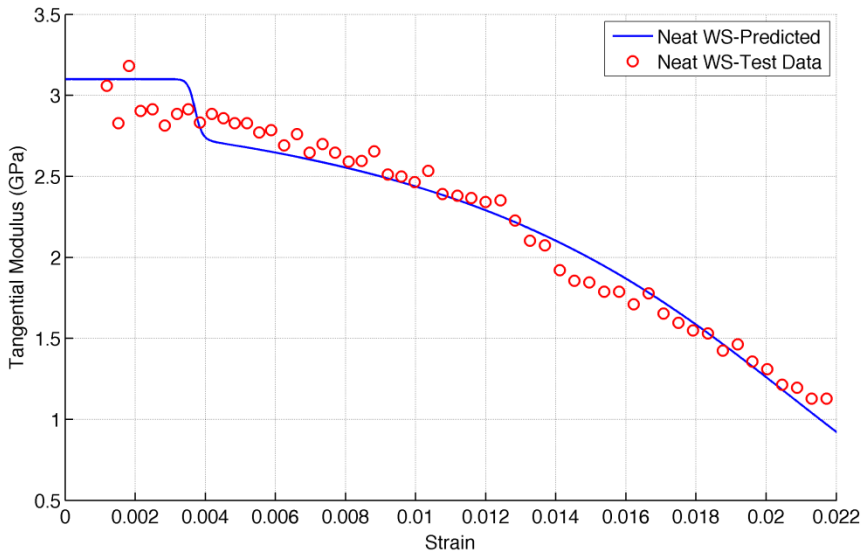

Figure 3.7 Variation of the tangential modulus of WS-105 neat epoxy resin, as a function of strain when the material loaded under quasi-static strain rate of 10^{-1} s^{-1}

Subsequently, having established neat resin's stress-strain response, the SRDM micromechanical model is used to establish the tensile stress-strain response of the resin reinforced with various weight-contents (%wt) of the three nanoparticle types, subjected to different strain rates. The predicted responses are then compared to the experimental results.

Figure 3.8 shows comparison of the predicted and experimental stress-strain curves. Figure 3.8(a) illustrates the variation in stress-strain response as a function of nanoparticles type under quasi-static strain rate of 10^{-3} s^{-1}. Figure 3.8(b) shows the influence of GNP weight-content on the predicted stress-strain responses, loaded at a quasi-static strain rate of 10^{-3} s^{-1}. Finally, Figure 3.8(c) illustrates the influence of the different strain rates on the predicted stress-strain responses of the resin reinforced with 1% wt GNP. It can be seen from the results illustrated in Figure 3.8, that in all cases, the predicted values are in good agreement with the experimental results.

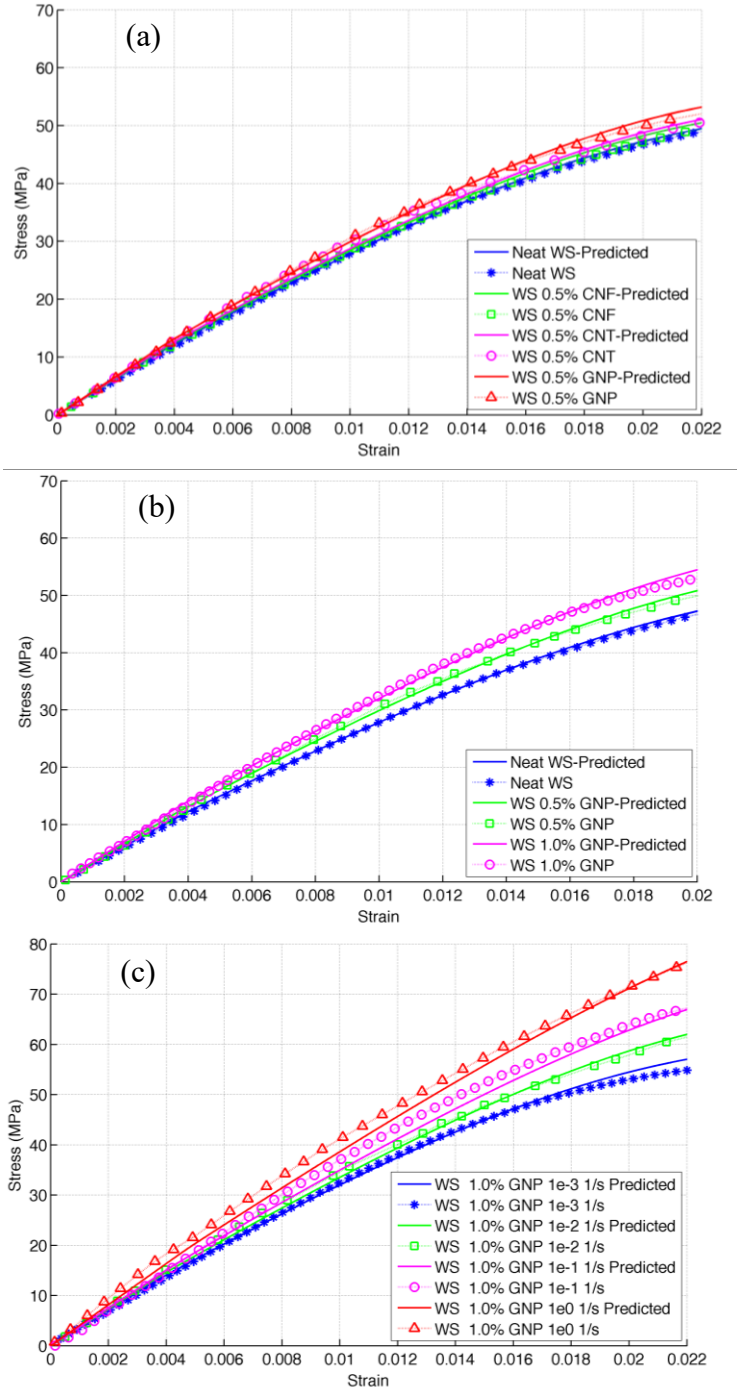

Figure 3.8 Comparison of predicted and experimental stress-strain curves of WS-105 resins reinforced with various types of nanoparticles; (a) Influence of nanoparticles type; (b) Influence of GNP weight-content for a quasi-static strain rate of 10^{-3} s^{-1}; and (c) influence of strain rate on the stress-strain responses of resin with 1wt% GNP.

As seen from the results shown in Figure 3.8(a), the inclusion of the GNP produced the most optimum enhancement of the mechanical response of the resin. Moreover, among the weight

contents considered for the inclusion of GNP in this study, 1 wt% was found to produce the most optimum mechanical response, regardless of the applied strain rates (see Figure 3.8(b)). It was also demonstrated that both the strength and stiffness of the nanoparticle-reinforced resin were increased as the strain rate was increased.

To study the vibration response of 200×20×3.5 mm^3 (l×b×h) beams made of aluminum, pure and GNP-reinforced epoxy resin, following specifications were taken into account (Table 3.2):

Table 3.2 Material specification of aluminum, pure and GNP-reinforced WS-105 epoxy resin beams

	E (GPa)	ν	ρ (kg/m^3)	nElemnts	t (ms)	$\mathcal{R}_a$	$\mathcal{R}_b$	κ
Aluminum (6061)	70	0.33	2700	25	50	0.01	2.04e-6	5/6
Pure WS-105 epoxy	2.708	0.3	1180	25	50	250	2e-5	5/6
GNP-reinforced WS-105 epoxy	3.27	0.3	1180	25	50	250	2e-5	5/6

It is worth mentioning that $\mathcal{R}_a$ and $\mathcal{R}_b$ values were chosen based on trial and error and still require experimental investigations to calibrate the values, for the best outcome. Obtained fundamental frequencies ($\tilde{\omega}$) and damping ratios ($\tilde{\xi}$) have been summarized in Table 3.3, also illustrated in Figure 3.9.

Table 3.3 Fundamental frequencies and damping ratios of aluminum, pure and GNP-reinforced epoxy resin obtained numerically

	$\tilde{\omega}_{Num.}$ (Hz)	$\tilde{\omega}_{Exp.}$ (Hz)	$\tilde{\xi}_{Num.}$	$\tilde{\xi}_{Exp.}$
Aluminum (6061)	458.80	463.75	1.80e-5	4.79e-4
Pure WS-105 epoxy	136.40	N/A	3.82e-5	N/A
GNP-reinforced WS-105 epoxy	149.90	N/A	8.21e-4	N/A

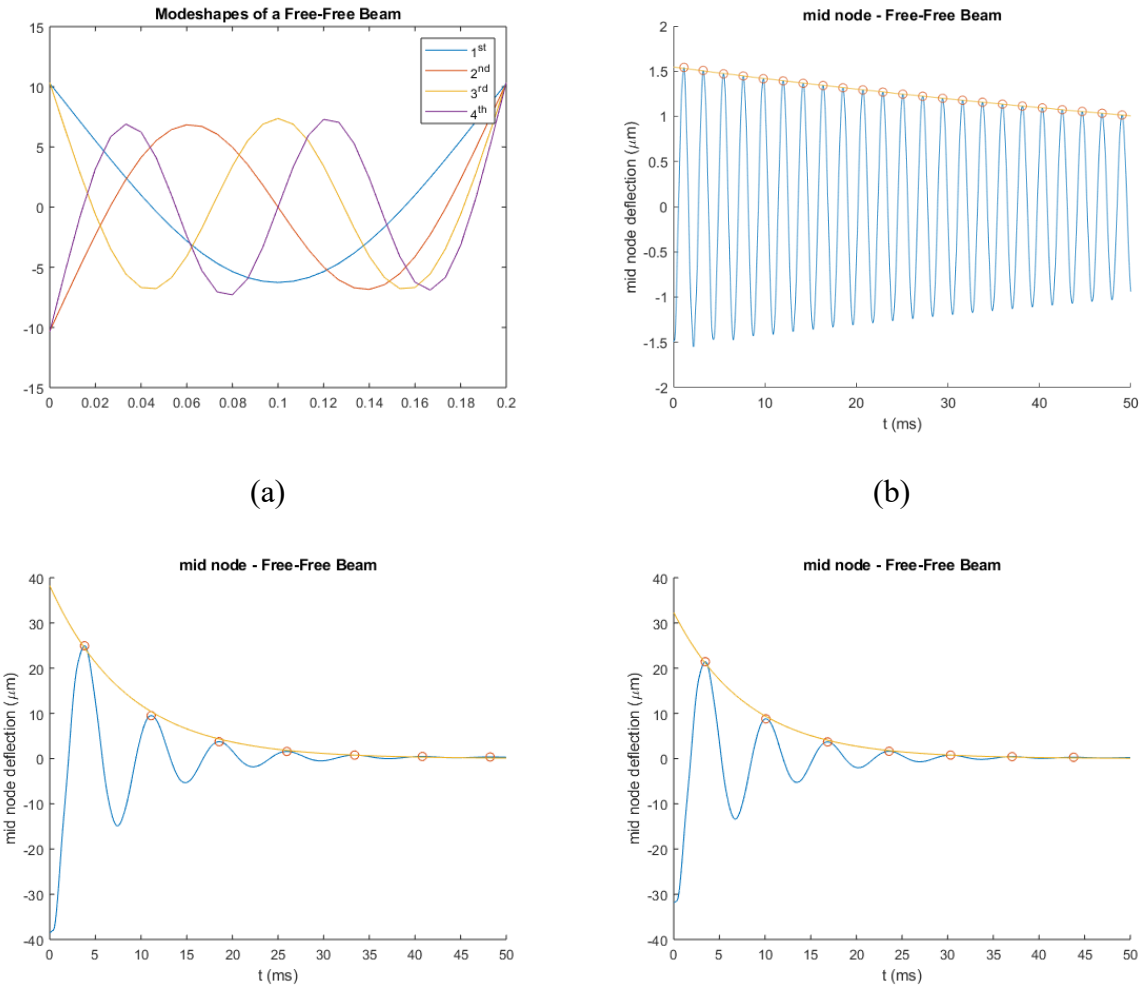

Figure 3.9 (a) Mode shapes of an aluminum beam with F-F BC, (b) Transient response of an aluminum beam with F-F BC used to calculate its damping ratio, (c) Transient response of pure epoxy resin, and (d) Transient response of GNP-reinforced epoxy resin.

As for the base-line tests, the fundamental frequency of aluminum, obtained numerically, is relatively in agreement with the experimental results by an order of magnitude. The details of experimentation are available in subsection 5.6.1. As it is shown in Table 3.3 and Figure 3.9, the inclusion of GNP increases the fundamental frequency and damping ratio of GNP-reinforced epoxy resin compared to the pure one.

3.8 Conclusions

This study demonstrated that the combination of a strain rate dependent mechanical (SRDM) model (in this case, the Goldberg et al. model) and a micromechanical model (in this case, the Halpin-Tsai model) could predict the stress-strain response of neat and nanoparticle reinforced epoxy resins with good accuracy. The predicted results also revealed that the response of the resin was improved when it was reinforced with the relatively inexpensive type nano-carbon particles (i.e., GNP), in comparison to the more expensive CNTs. It was also demonstrated that the increase in strain rate resulted in higher apparent strength and stiffness of nanoparticle-reinforced resin. Comparatively, this increase was even more significant than the enhancement obtained by inclusion of the nano-carbon particles. Moreover, the enhancement in resin's stiffness was observed to be more significant compared to the gain in its strength.

As noted, the inclusion of GNP into the neat resin improved the stiffness of the adhesive, resulting in enhancement of the elastic modulus by 11%, and 21% for the resin reinforced 0.5 wt% GNP, evaluated at the lowest, and highest strain rates, respectively. Furthermore, based on the obtained results, one can conclude that the higher weight percentage (i.e., 1 wt% GNP) resulted in the highest stiffness. It was also observed that reinforced resin's modulus of elasticity was enhanced by 19%, and 33% when the resin was reinforced with 1 wt% GNP, and when the material was tested under the lowest and highest loading rates, respectively.

Further, comparison of the results obtained for the resin reinforced with 0.5 wt% of GNP and that reinforced with 0.5 wt% of CNF, subjected to the quasi-static strain rate, revealed that the inclusion of GNP produced a greater average ultimate tensile strength and modulus of elasticity than the inclusion of CNF could.

Finally, the transient response analysis of pure and GNP-reinforced polymer composite beams at room temperature indicated that the inclusion of GNP mitigates the settling-time response of the vibration, and increases the damping ratio.

Chapter 4

Quantification of the Effects of Strain Rate and Nano-reinforcement on the Performance of Adhesively Bonded Single-Lap Joints

4.1 Publication Statement

This chapter has been published as peer-reviewed journal publication in Vol. 8, No. 2 of the journal "Reviews of Adhesion and Adhesives" (CiteScore 1.8 (Scopus; 2020)), by B. Soltannia as the 1st author. Its title is "Quantification of the Effects of Strain Rate and Nano-Reinforcement on the Performance of Adhesively Bonded Single-Lap Joints". It consists of 19 single-spaced single-column pages and was published in 2020 [2]. Note that Section 4.2 'Nomenclature' is not part of the published article and has been added to this chapter later.

4.2 Nomenclature

AUSS	Averaged ultimate shear strength
A	Adherend type
N	Nanoparticle type
S	Strain-rate
W	Weight percentage of the nanoparticles

4.3 Introduction

Single-lap joints (SLJs) are widely used to mate both fiber-reinforced polymer (FRP) composite and/or metallic structural components in aerospace, marine, automotive, offshore/onshore oil and gas industries and infrastructures. FRP SLJs offer several advantages, including high strength- and stiffness-to-weight ratios, good corrosion resistance and fatigue tolerance, high energy absorption capacity, and controllable damage mechanism, all of which make them more efficient compared to mechanically fastened joints [47,142–149] . However, a major concern with the use of adhesively bonded joints (ABJs) in critical applications has been the lack of adequate database in regard to their mechanical performance under various strain rates, especially at high strain rates (HSRs). Compounded to that factor is the lack of a wide-range database related to the performance of the most recently developed adhesives based on newly emerging techniques.

One of the emerging techniques is strengthening and toughening adhesives by incorporation of various types of nanoparticles (NPs). The NPs that are most widely discussed in the scientific literature are carbon nanotubes (CNTs), which is despite the advantages that carbon nanofibers (CNFs) and graphene nanoplatelets (GNP) offer. Ironically, the latter types have larger aspect ratios, are more widely available and are less expensive than CNTs. The use of carbon nanotubes, which are essentially sheets of graphite rolled into tubes [150], was first proposed by Iijima in 1991. The multi-walled carbon nanotubes (MWCNTs) contain a number of coaxial graphene cylinders, each of which has an end cap, with an outer diameter of 3-10 nm [71]. The strength of MWCNTs has been estimated to be up to 150 GPa and their elastic modulus up to 900 GPa [98]. Their superior mechanical characteristics and superior length-to-diameter ratio make CNTs highly desirable for reinforcement of resins [151].

Hsiao et al. [151] demonstrated that utilizing 5 percent by weight (wt%) MWCNTs in conjunction with an epoxy adhesive could facilitate a more effective shear stress transfer to the adherends. Not only did the addition of the NPs enhance the average shear strength of the joints by 45.6%, but it also facilitated the desired cohesive failure mode.

GNP is another type of nanoparticles, consisting of stocks of platelets that are exfoliated or intercalated by a polymer during processing. The thickness of these plate-like particles is approximately 1 nm and their lateral dimensions can vary from 25 nm to one micron, indicating that they have large aspect ratios [67,126].

It is worth mentioning that the time-dependent behavior of the SLJs should be fully understood, since full understanding of the effect of strain rate on the response of SLJs would enable engineers to design more reliable structures. To understand the time-dependent performance of ABJs, one would have to consider the influence of several parameters, which would render the process time-consuming. As a result, researchers have reported inconsistent observations in regard to the effect of strain rate on the performance of ABJs. For instance, in contrast to the observations of Harris and Adams [152], stating that the strength of SLJs is insensitive to loading rate, an average increase of more than 50% in strength was observed by Galliot et al. [153,154], who reported the results of absorbed energy by ABJs subjected to impact and quasi-static loading, indicating that the failure load and the stiffness response of their joints were intensified as a function of increasing strain rate. Their baseline quasi-static loading tests were conducted using a universal servo-hydraulic test machine at a loading rate of 0.3 mm/min.

In order to effectively determine the influence of strain rate, and the other mentioned parameters that affect the performance of ABJs, one can employ the design of experiment (DOE) approach. It should be briefly mentioned that DOE can aid researchers to increase the efficacy of

an experimental investigation by two means. Firstly, it can be used to optimize the number of the required experiments when the effect of a set of parameters is to be established. Secondly, it can be effectively used to establish the validity and consistency of a set of experimental data and effectively rank the most influencing parameters in a given experiment [155,156]. In this paper, we demonstrate the second utility of the DOE approach.

The objective of this study is to enhance the averaged ultimate shear strength (AUSS) of SLJs and consequently to develop a relatively inexpensive and strong adhesive for common engineering applications. Therefore, a statistical approach has been employed to quantify the influence of a set of factors on the mechanical response of SLJs using two mixed-level full factorial methodology. First, the influence of various variables on the AUSS of SLJs is assessed. Subsequently, once the most influencing variable, strain rate, is identified, the phase 2 of analyses is conducted, through which the other influencing variable, wt%, and its interaction and influence on AUSS of SLJ is examined in detail. Moreover, SLJs can be considered a simpler yet somewhat similar geometry to 3D-FMLs. This study also provides some indication of the effects of NP modification on structural performance and static characteristics of NP-reinforced polymers and their composites in SLJs and possible causes for enhanced performance. This chapter thus serves as a preparatory part for work on 3D-FMLs.

4.4 Materials and Methods

As briefly stated earlier, the effect of strain rate on the mechanical response of nano-reinforced SLJs with different types of FRP adherends is investigated in this work, and the results are compared with those obtained through static, quasi-static and HSR tests. Uni-directional carbon and E-glass fiber-reinforced epoxy laminates are used to fabricate the adherends (see Figure

4.1). The HSR tests are carried out using a modified instrumented Charpy pendulum, equipped with a specially designed tension impact apparatus (see Figure 4.2). The static and quasi-static tests are conducted on an Instron 8500+ universal testing machine equipped with a digital electronic controller (see Figure 4.3) [124]. For details on the employed material systems, specimen fabrication and testing procedures the reader is referred to authors previous works [1,124,125].

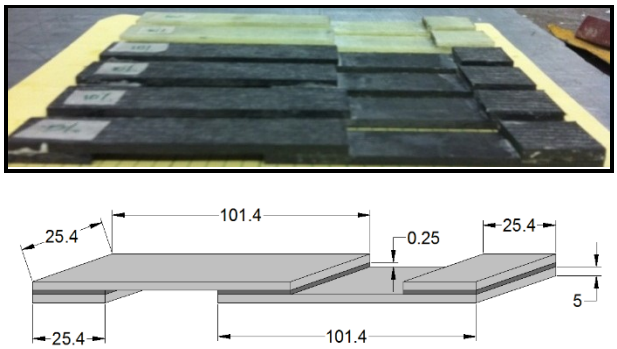

Figure 4.1 Typical single-lap joint specimens (dimensions in mm; drawing not to scale) [124].

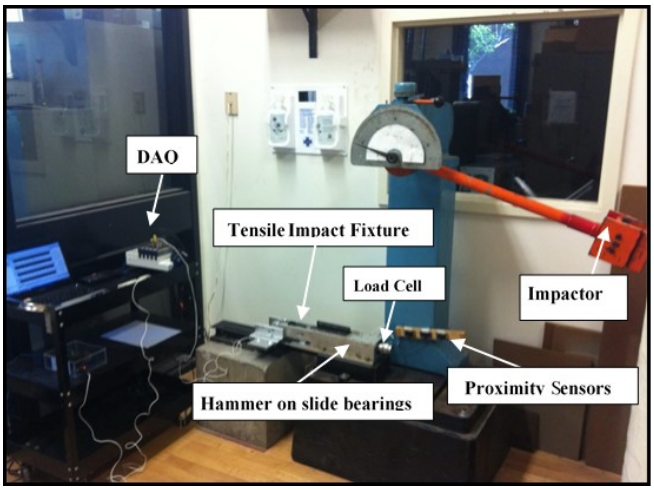

Figure 4.2 Experimental test setup used in the high strain rate test (tensile impact apparatus) [124].

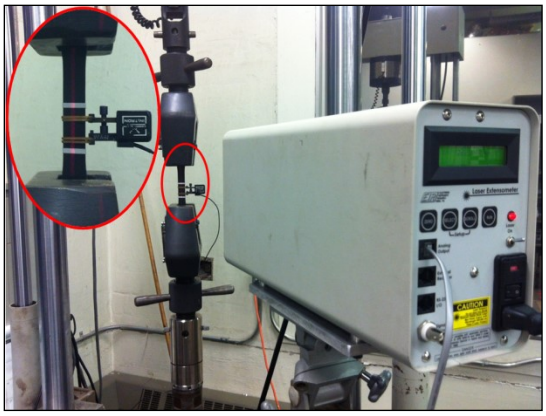

Figure 4.3 Experimental setup used for conducting the static and quasi-static strain rate tests [124].

4.5 Design of Experiments (DOE) Methodology

As briefly stated earlier, DOE is a statistical technique to investigate the dominance of various parameters that influence the response of an experiment; the methodology is mainly implemented to efficiently optimize the output with the least number of required experiments [155]. The flowchart shown in Figure 4.4 demonstrates each step involved in a typical DOE analyses.

In this approach, first, a mixed-level full factorial design (2×3^2) is conducted as the phase 1. The objective of the phase 1 within the context of our investigation is to study the influence of the NP type, adherend type, and strain rate as manipulated variables, while keeping the wt% of the particles constant at 0.5 wt% as the controlled variable (see Table 4.1 and 4.2).

In the phase 2, another mixed-level full factorial design (2×3^2) is performed to investigate the influence (or the "dominance", in DOE terminology) and interactions (nonlinearity) between the wt% content of GNP, strain rate and adherend type as manipulated variables. The NP type (GNP) is considered as controlled variable, identified dominant variable in phase 1 (see Table 4.3 and 4.4). Since in this study, the number of levels from one factor to another is different, therefore,

two mixed-level full factorial designs (i.e., $2\times(2\times3^2)=36$) are adapted to establish the influence of the aforementioned parameters on the AUSS of the SLJs through the phase 1 and the subsequent phase 2 analyses [156]. As stated, NP type was the so-called “manipulated variable” in the phase 1, while in the phase 2, NP type was fixed and the GNP content (wt%) was considered as the manipulated variable.

In this work, the three most significant manipulated factors affecting the mechanical response of the SLJs were selected based on our previous studies (see Tables 4.1 and 4.3) [1,124,125]. Tables 4.2 and 4.4 summarize the selected controlled variables according to the standards [150,157–161]. The AUSS is the selected response variable in this work. Repeated measurements was not considered in this study due to the destructive nature of such experiments; however, each test was replicated three times.

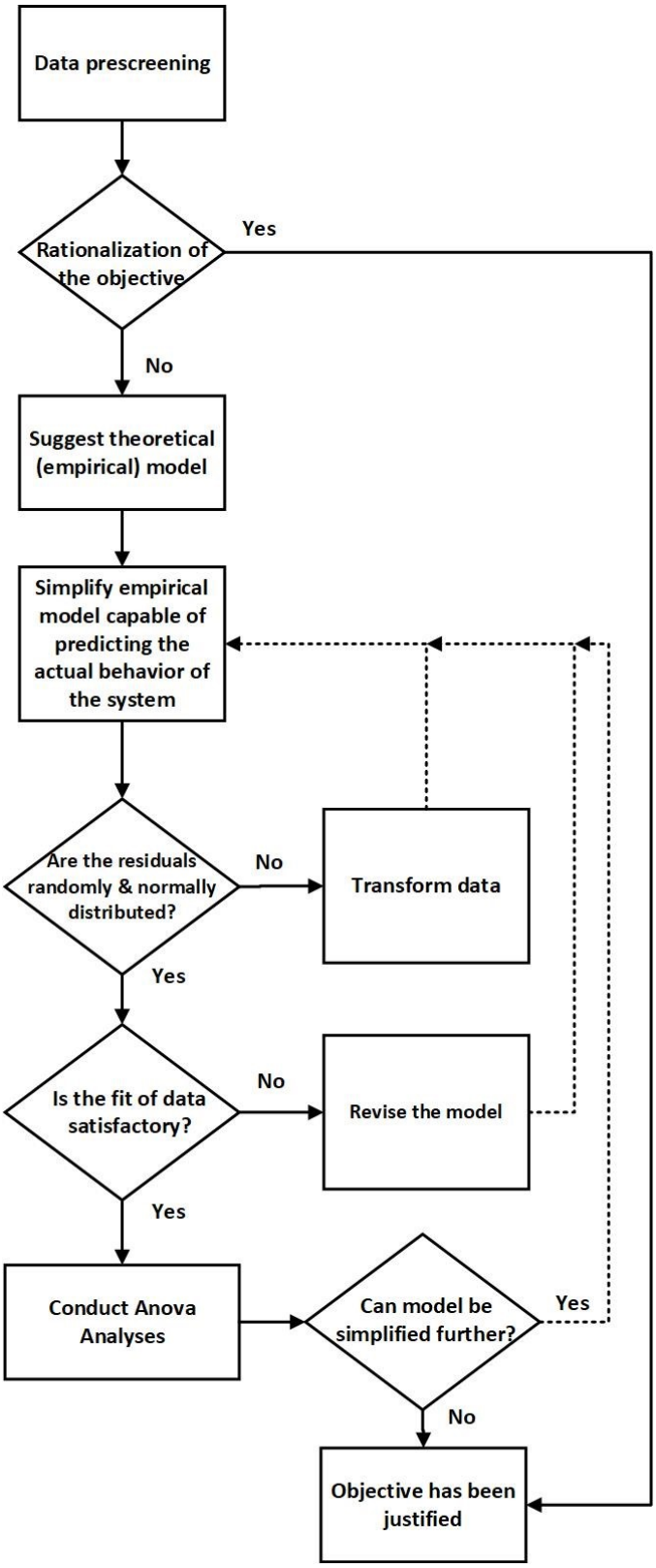

Figure 4.4 Flowchart showing the required steps for design of experiments.

Table 4.1 Manipulated variables for the phase

Manipulated variable(s)	Factor Level		
	-1	0	1
Adherend Type	Glass-epoxy		Graphite-epoxy
Nanoparticle Type	GNP	MWCNT	CNF
Strain Rate (S^{-1})	Static ($1x10^{-3}$)	Quasi-Static ($1x10^{-2}$)	Impact ($1.338x10^{2}$)

Table 4.2 Controlled variables for the phase

Controlled Variable(s)	Level
Single-lap joint geometry	See Figure 4.1
Adhesive thickness	0.25 mm
Adhesive type (thermoset)	WS* 105 Resin, 206 hardener
Adherend thickness	5.0 mm
Nano particle weight percent	0.5 wt%
Temperature	22 °C

*WS stands for West System® [Bay City, MI]

Table 4.3 Manipulated variables for the phase 2

Manipulated variable(s)	Factor Level		
	-1	0	1
Adherend Type	Glass-epoxy		Graphite-epoxy
GNP wt%	0%	0.5%	1.0%
Strain Rate (S^{-1})	Static ($1x10^{-2}$)	Quasi-Static ($1x10^{-1}$)	Impact ($1x10^{0}$)

Table 4.4 Controlled variables for the phase 2

Controlled Variable(s)	Level
Single lap joint geometry	See Figure 4.1
Adhesive thickness	0.25 mm
Adhesive type (thermoset)	WS* 105 Resin, 206 hardener
Adherend thickness	5.0 mm
Nano particle type	GNP
Temperature	22 °C

*WS stands for West System® [Bay City, MI]

4.6 Results

4.6.1 Influence of the Variables on the AUSS of SLJs

In DOE, the normal distribution and randomness of the data are usually evaluated through two plots. First, the distribution of the normal probability of a set of data as a function of the residuals is constructed, followed by tracing the variation of the residuals as a function of the predicted values. There were no significant outlier values, which indicates that the data is normally distributed. The influences of the selected parameters are illustrated through a Pareto chart in Figure 4.5 using STATISTICA® software (Dell Software, Round Rock, TX, United States). The values in the chart indicate that adherend type, strain rate, and NP types all have a linearly varying effect on AUSS of the SLJs, with adherend being the most dominant. In other words, in phase 1, regarding the linear effect of manipulated variables (among those manipulated variables having linear effect), the Adherend Type has the most dominant linear effect.

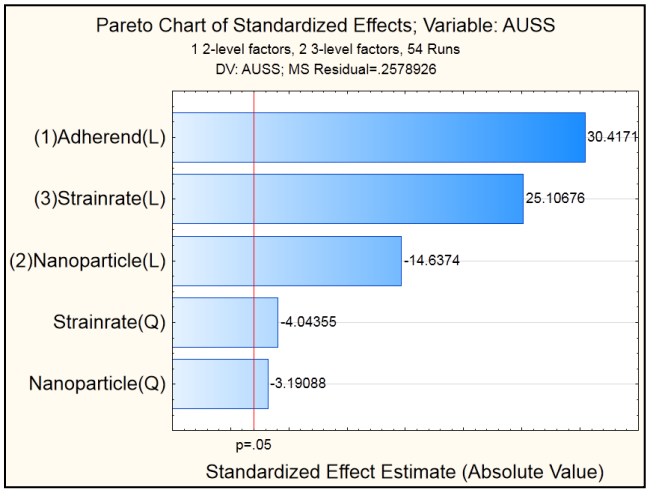

Figure 4.5 The Pareto chart of the phase 1

Table 4.5 is the effect estimates table for the phase 1 of analyses, which helps to distinguish the influence of a particular manipulated variable on AUSS. In other words, it reveals the predicted change in the mean response values as a function of the parameters changing from a low to higher

values. It is shown that strain rate, which affects the results in a nonlinear (quadratic) fashion, had predominant effect on the AUSS than other manipulated variables. This means, in terms of nonlinear (quadratic) effect of manipulated variables (among those manipulated variables also having nonlinear (quadratic) effect), strain rate has dominant effect.

Table 4.5 Effect estimates results of the phase 1

Factor	Effect Estimates; Var.:AUSS; R-sqr=.97992; Adj:.97339 (Spreadsheet100) 1 2-level factors, 2 3-level factors, 54 Runs DV: AUSS; MS Residual=.2388127									
	Effect	Std.Err.	t(40)	p	-95.% Cnf.Limt	+95.% Cnf.Limt	Coeff.	Std.Err. Coeff.	-95.% Cnf.Limt	+95.% Cnf.Limt
Mean/Interc.	12.78333	0.199505	64.07536	0.000000	12.38012	13.18655	12.78333	0.199505	12.38012	13.18655
(1)Adherend(L)	4.08704	0.297404	13.74237	0.000000	3.48596	4.68811	2.04352	0.148702	1.74298	2.34406
(2)Nano Type(L)	-2.53833	0.282142	-8.99665	0.000000	-3.10856	-1.96810	-1.26917	0.141071	-1.55428	-0.98405
Nano Type(Q)	1.27500	0.488685	2.60904	0.012709	0.28733	2.26267	0.63750	0.244342	0.14367	1.13133
(3)Strain Rate(L)	4.33167	0.282142	15.35278	0.000000	3.76144	4.90190	2.16583	0.141071	1.88072	2.45095
Strain Rate(Q)	1.52500	0.488685	3.12062	0.003344	0.53733	2.51267	0.76250	0.244342	0.26867	1.25633
1L by 2L	-0.22889	0.162895	-1.40513	0.167701	-0.55811	0.10033	-0.11444	0.081447	-0.27906	0.05017
1L by 2Q	-0.05556	0.282142	-0.19691	0.844898	-0.62579	0.51468	-0.02778	0.141071	-0.31289	0.25734
1L by 3L	-0.12222	0.162895	-0.75031	0.457457	-0.45145	0.20700	-0.06111	0.081447	-0.22572	0.10350
1L by 3Q	0.23111	0.282142	0.81913	0.417566	-0.33912	0.80134	0.11556	0.141071	-0.16956	0.40067
2L by 3L	-0.55250	0.199505	-2.76936	0.008474	-0.95571	-0.14929	-0.27625	0.099752	-0.47786	-0.07464
2L by 3Q	0.09083	0.345552	0.26286	0.794004	-0.60755	0.78922	0.04542	0.172776	-0.30378	0.39461
2Q by 3L	-0.12250	0.345552	-0.35451	0.724823	-0.82089	0.57589	-0.06125	0.172776	-0.41044	0.28794
2Q by 3Q	-0.50917	0.598514	-0.85072	0.399990	-1.71881	0.70048	-0.25458	0.299257	-0.85940	0.35024

Next, we examine the plots of mean values (Figure 4.6), which essentially represents the influence of the manipulated variables selected in this study. The variations in the AUSS, as a function of NP type for different strain rates, reveals that the greatest enhancement could be obtained by GNP (-1 nano type) NPs in comparison to the gains attained by the inclusion of CNT and CNF nanoparticles. Hence, in the phase 2 of analyses, the GNP's was held constant but weight content was selected as the new manipulated variable. Table 4.6 reports the regression coefficients for the phase 1 of analyses.

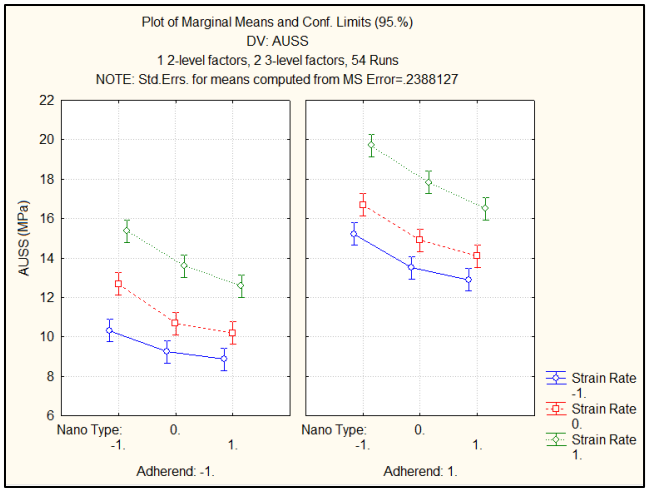

Figure 4.6 Interaction (Mean) plots of the phase 1 tests (see Table 4.1 for the meaning of -1, 0 and 1 noted on the chart). Note that data is valid only for discrete values at -1, 0, and 1, lines have been added to guide the eye. Some data points are offset from the integer values by the software to improve clarity.

Table 4.6 Regression table for the phase 1 analyses

Factor	Regressn Coeff.	Std.Err.	t(40)	p	-95.% Cnf.Limt	+95.% Cnf.Limt
	Regr. Coefficients; Var.:AUSS; R-sqr=.97992; Adj:.97339 (Spreadsheet100) 1 2-level factors, 2 3-level factors, 54 Runs DV: AUSS; MS Residual=.2388127					
Mean/Interc.	12.78333	0.199505	64.07536	0.000000	12.38012	13.18655
(1)Adherend(L)	2.04352	0.148702	13.74237	0.000000	1.74298	2.34406
(2)Nano Type(L)	-1.26917	0.141071	-8.99665	0.000000	-1.55428	-0.98405
Nano Type(Q)	0.63750	0.244342	2.60904	0.012709	0.14367	1.13133
(3)Strain Rate(L)	2.16583	0.141071	15.35278	0.000000	1.88072	2.45095
Strain Rate(Q)	0.76250	0.244342	3.12062	0.003344	0.26867	1.25633
1L by 2L	-0.11444	0.081447	-1.40513	0.167701	-0.27906	0.05017
1L by 2Q	-0.02778	0.141071	-0.19691	0.844898	-0.31289	0.25734
1L by 3L	-0.06111	0.081447	-0.75031	0.457457	-0.22572	0.10350
1L by 3Q	0.11556	0.141071	0.81913	0.417566	-0.16956	0.40067
2L by 3L	-0.27625	0.099752	-2.76936	0.008474	-0.47786	-0.07464
2L by 3Q	0.04542	0.172776	0.26286	0.794004	-0.30378	0.39461
2Q by 3L	-0.06125	0.172776	-0.35451	0.724823	-0.41044	0.28794
2Q by 3Q	-0.25458	0.299257	-0.85072	0.399990	-0.85940	0.35024

At this juncture, a model is proposed, which was obtained by conducting a multi-variable least-square regression of the data reported in Table 4.6 using STATISTICA®. By using the proposed model (equation (4.1)), one can evaluate a given SLJ's AUSS (the response variable) as

a function of NP type, strain rate, and adherend type (in other words, evaluating AUSS as a function of the manipulated variables). The model is somewhat complicated due to the interactions of the variables which are both linear and nonlinear.

$$\begin{aligned}\text{AUSS} = 12.783 \; &+ 2.043\,A - 1.269\,N + 0.6375\,N^2 + 2.165\,\text{S} + 0.762\,S^2 - 0.114\,AN - \\ &0.027\,AN^2 - 0.061\,AS + 0.115\,AS^2 - 0.276\,NS + 0.045\,NS^2 - 0.061\,N^2S - \\ &0.254\,N^2S^2 \end{aligned} \tag{4.1}$$

In the above equation, *A* refers to adherend type, *N* refers to NP type, and *S* represents the strain-rate. It is worth mentioning that as the factors involved in an experiment can be either qualitative or quantitative [155], here, adherend type and NP type are qualitative and must be fixed at their levels -1, 0 or 1, however the magnitude of the coefficients in the equation still show their relative importance.

The surface plot shown in Figure 4.7 exhibits a pseudo-linear relationship (not completely linear and not completely nonlinear, with tendency towards linear behavior) between AUSS versus strain rate and NP type. Moreover, the slope of the surface plot corresponding to the strain rate and NP type demonstrates the intensity of the influence of these factors on AUSS.

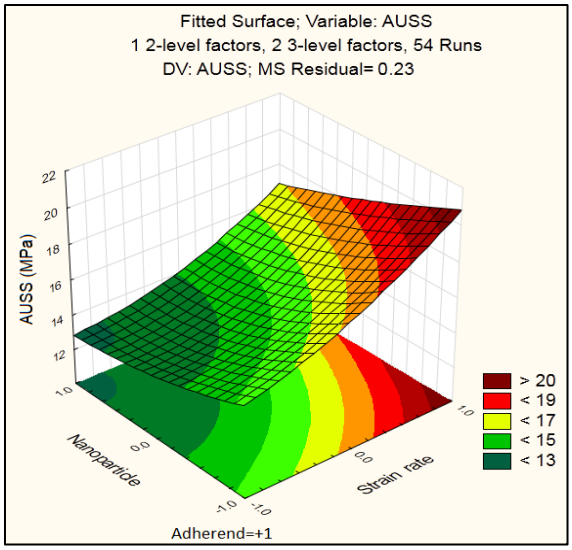

Figure 4.7 Surface plot of AUSS (MPa) vs. strain rate and nano particle type (for the SLJ with CFRP adherend). Note that a continuous surface is shown for illustration purposes only, with data being valid only for discrete values at -1, 0, and 1.

4.6.2 Influence of GNP wt% on AUSS of the SLJs

Figure 4.8 and Table 4.7 show the Pareto chart and the effect estimates table for the phase 2 of analyses, respectively. Note the effect estimate values enables one to discern the influence of a particular manipulated variable on AUSS. In other words, it reveals the predicted change in the mean response values as a function of the parameters changing from a low to higher values. It is shown that NP content (wt%), which affects the results in a nonlinear (quadratic) fashion, had a more predominant effect on the AUSS than the strain-rates. This further confirms the importance of NP wt% in comparison to the other manipulated variables, i.e., in phase 2, NP wt% was found to be the most dominant linear as well as nonlinear (quadratic) effect.

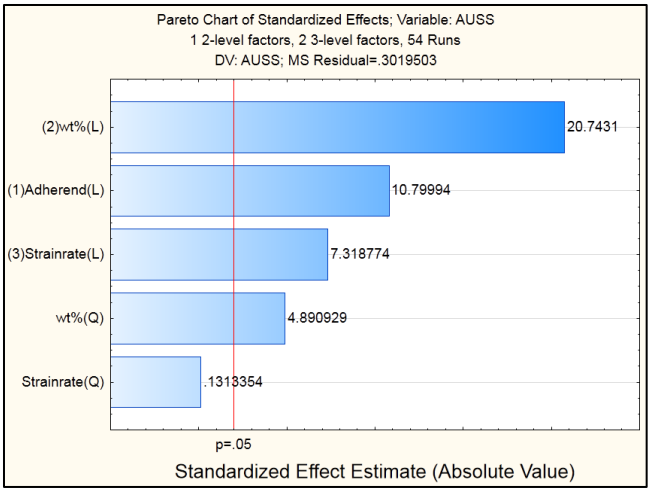

Figure 4.8 Pareto chart of the phase 2 of analyses

Table 4.7 Effect estimates table of the phase 2 of analyses

Factor	Effect Estimates; Var.:AUSS; R-sqr=.99044; Adj:.98733 (Spreadsheet24) 1 2-level factors, 2 3-level factors, 54 Runs DV: AUSS; MS Residual=.0485369									
	Effect	Std.Err.	t(40)	p	-95.% Cnf.Limt	+95.% Cnf.Limt	Coeff.	Std.Err. Coeff.	-95.% Cnf.Limt	+95.% Cnf.Limt
Mean/Interc.	15.27500	0.029981	509.4978	0.000000	15.21441	15.33559	15.27500	0.029981	15.21441	15.33559
(1)Adherend(L)	1.61519	0.059961	26.9373	0.000000	1.49400	1.73637	0.80759	0.029981	0.74700	0.86819
(2)wt%(L)	3.79944	0.073437	51.7375	0.000000	3.65102	3.94787	1.89972	0.036718	1.82551	1.97393
wt%(Q)	0.77583	0.063598	12.1990	0.000000	0.64730	0.90437	0.38792	0.031799	0.32365	0.45219
(3)Strainrate(L)	1.34056	0.073437	18.2545	0.000000	1.19213	1.48898	0.67028	0.036718	0.59607	0.74449
Strainrate(Q)	0.02083	0.063598	0.3276	0.744940	-0.10770	0.14937	0.01042	0.031799	-0.05385	0.07469
1L by 2L	0.62389	0.073437	8.4956	0.000000	0.47547	0.77231	0.31194	0.036718	0.23773	0.38616
1L by 2Q	0.84361	0.063598	13.2647	0.000000	0.71507	0.97215	0.42181	0.031799	0.35754	0.48607
1L by 3L	0.06833	0.073437	0.9305	0.357693	-0.08009	0.21675	0.03417	0.036718	-0.04004	0.10838
1L by 3Q	-0.10306	0.063598	-1.6204	0.113001	-0.23159	0.02548	-0.05153	0.031799	-0.11580	0.01274
2L by 3L	0.23667	0.089942	2.6313	0.012022	0.05489	0.41845	0.11833	0.044971	0.02744	0.20922
2L by 3Q	0.01167	0.077892	0.1498	0.881690	-0.14576	0.16909	0.00583	0.038946	-0.07288	0.08455
2Q by 3L	0.00833	0.077892	0.1070	0.915335	-0.14909	0.16576	0.00417	0.038946	-0.07455	0.08288
2Q by 3Q	-0.01250	0.067456	-0.1853	0.853926	-0.14883	0.12383	-0.00625	0.033728	-0.07442	0.06192

Furthermore, examination of the interaction plot illustrated in Figure 4.9 further confirms the fact that 1 wt% GNP content would produce the maximum enhancement of the response variables and that it has the greatest effect among the other parameters considered in this study.

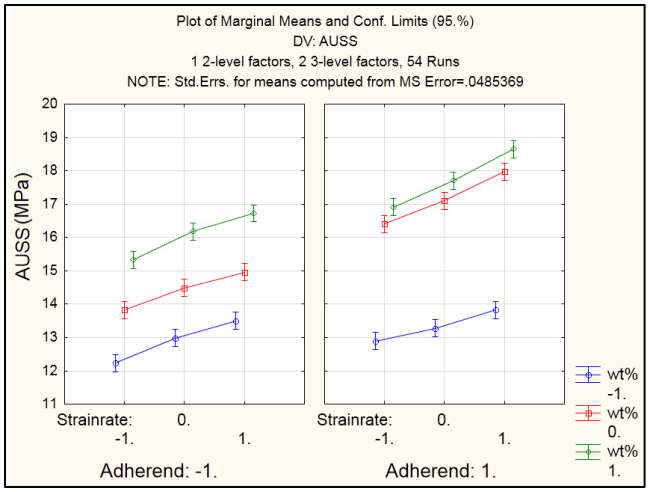

Figure 4.9 Interaction (Mean) plot of the phase 2 of analyses (see Table 4.3 for the meaning of -1, 0 and 1 noted on the chart). Note that data is valid only for discrete values at -1, 0, and 1, lines have been added to guide the eye. Some data points are offset from the integer values by the software to improve clarity.

In DOE, the half-normal plot illustrates graphically the order of considered factors' effect in terms of their importance. The results are shown for the phase 2 of analyses in Figure 4.10 also confirms that NP wt% has the greatest effect on AUSS.

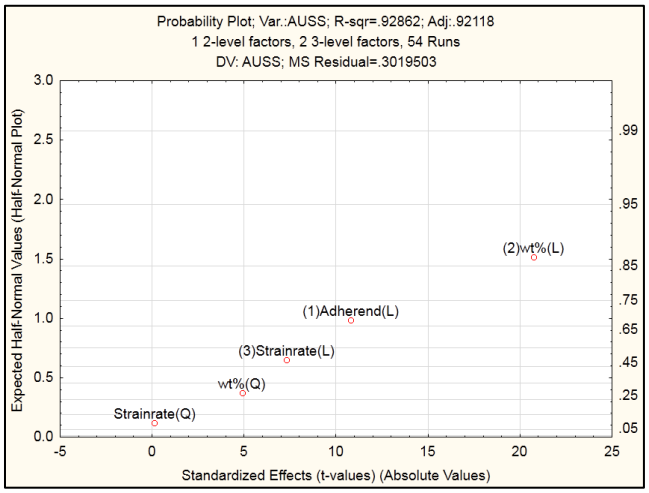

Figure 4.10 Half-normal plot of the phase 2

At this juncture, STATISTICA® software is used again to generate a reduced regression model based on the results obtained through this study, as reported in Table 4.8. The proposed

model (equation (4.2)), indicates that AUSS (response variable) is affected by NP wt%, strain-rate, and adherend type (i.e., the manipulated variables), as well as having some linear and quadratic interactions with the lower probability value (P-value).

Table 4.8 Reduced regression values of the phase 2 of analyses

Factor	Regr. Coefficients; Var.:AUSS; R-sqr=.98956; Adj:.98797 (Spreadsheet24) 1 2-level factors, 2 3-level factors, 54 Runs DV: AUSS; MS Residual=.0460753					
	Regressn Coeff.	Std.Err.	t(46)	p	-95.% Cnf.Limt	+95.% Cnf.Limt
Mean/Interc.	15.79222	0.050594	312.1371	0.000000	15.69038	15.89406
(1)Adherend(L)	1.37000	0.050594	27.0784	0.000000	1.26816	1.47184
(2)wt%(L)	1.89972	0.035775	53.1016	0.000000	1.82771	1.97173
wt%(Q)	-0.77583	0.061965	-12.5206	0.000000	-0.90056	-0.65111
(3)Strainrate(L)	0.67028	0.035775	18.7358	0.000000	0.59827	0.74229
1L by 2L	0.31194	0.035775	8.7196	0.000000	0.23993	0.38396
1L by 2Q	-0.84361	0.061965	-13.6144	0.000000	-0.96834	-0.71888
2L by 3L	0.11833	0.043816	2.7007	0.009652	0.03014	0.20653

$$\text{AUSS} = 15.795 + 1.37\,A + 1.89\,W - 0.77\,W^2 + 0.67583\,\text{S} + 0.31194\,AW - 0.84351\,AW^2 + 0.11833\,WS \quad (4.2)$$

In the above equation, W represents NP wt%, and A, W, and S are as defined previously in equation (4.1).

The contour (or surface) plot illustrated in Figure 4.11 reveals a linear relationship between the strain rate and AUSS, but a nonlinear interaction between NP wt% and AUSS, respectively. Moreover, the slope of the surface plot demonstrates the intensity of the influence of these factors on AUSS.

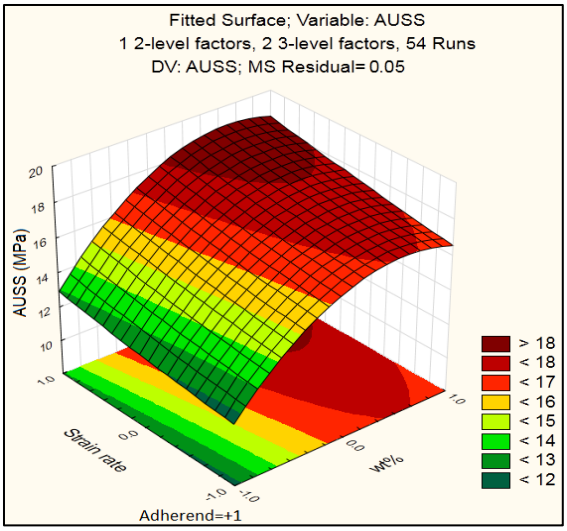

Figure 4.11 Surface plot of AUSS (MPa) vs. nanoparticle wt% and strain-rate (CFRP adherend). Note that a continuous surface is shown for illustration purposes only, with data being valid only for discrete values at -1, 0, and 1.

The normal distribution and randomness of the data were evaluated with normal probability plot and the predicted vs. raw residuals without any concerns.

Another effective approach for illustrating the influence of the variables can be done through the Taguchi plot. This plot, which is also referred to as "signal-to-noise" or S/N plot essentially reveals the intensity of the independent variable leading to the best value of the response as measured by the largest value of the signal-to-noise (S/N) ratio (or simply, the ratio of mean to variance). In such plots (see Figure 4.12), the ratio of S/N denotes the greater influence of the variable. The plot clearly shows the dominant influence of NP wt% on the response variable.

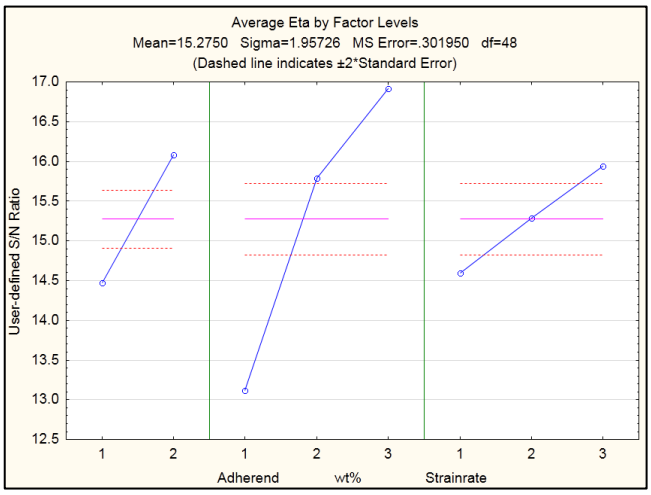

Figure 4.12 Taguchi results based on maximum S/N for the phase 2. Note that data is valid only for discrete values at -1, 0, and 1, lines have been added to guide the eye. Some data points are offset from the integer values by the software to improve clarity.

4.7 Discussion

Based on the results of this study presented in Figures 4.5 and 4.8, and Table 4.5, it is revealed that amongst the investigated variables, NP wt% proved to have the greatest influence on the ultimate load-bearing capacity of SLJs, dominating its effect in a quadratic fashion. Moreover, among the NPs considered in this study, the results shown in Figure 4.6 indicate that GNP produces the greatest enhancement in the joints load-bearing capacity, compared to CNT and CNF. Therefore, GNP was selected as a controlled variable for the phase 2 of analyses conducted within this study, while its wt% was considered as a manipulated factor to augment AUSS of SLJs. Results presented in this study (see Figures 4.8 and 4.9, and Table 4.7) reveals the intensity of GNP content on enhancing AUSS.

Based on the presented results the greatest AUSS value was attained by the inclusion of 1.0 wt% GNP content, and CFRP adherend type which was determined to be proper GNP-reinforcement content for enhancing the load-bearing capacity of the SLJ, under $1x10^{0}$ (S^{-1}). This

level of enhancement was attained when the joints were subjected to the highest strain rate amongst the rates considered in the phase 2 of this study. In other words, SLJ's load-bearing capacity was enhanced compared to the capacity of SLJs formed by the neat adhesive, which corroborates with the actual experimental results reported in [125]. For the future work, finding the optimum GNP wt%, after which the AUSS drops (i.e., 0.5% 1% and 1.5% to determine the behavior around 1%), has paramount importance and interest.

4.8 Conclusions

Improved results were obtained when the relatively inexpensive type nano-carbon (i.e., GNP) was added to the resin. It was also observed that the addition of CNF or MWCNTs to a widely used epoxy resin improved the resin's mechanical properties, but not to the same degree as the GNP did.

It was demonstrated that the increase in loading rate resulted in a higher apparent strength of the SLJ. This enhancement was even more significant than the enhancement obtained by inclusion of GNP in the resin.

As expected, SLJs with graphite/epoxy adherends exhibited higher strength compared to those formed by glass/epoxy adherends. This increase is attributed to the fact that graphite/epoxy adherends are in general stiffer than glass/epoxy adherends, and consequently, the bending moments at the overlap region (hence the shear and peel stresses) are comparatively lower.

Moreover, this study demonstrated the influence of some parameters such as NP wt%, adherend type, and strain-rate on the mechanical response of SLJs, particularly on their AUSS. It was shown that inclusion of GNP in the adhesive forming SLJs with CFRP adherends under HSR produced the most enhancement in the load-bearing capacity. Moreover, the effective utility of the DOE approach to optimize the augmentation of the response variables within a desired

experimental investigation was also demonstrated. It should also be mentioned that SLJs would exhibit higher load-bearing capacity when subjected to a load that is applied at a high rate.

Chapter 5

Static and Dynamic Characteristics of Nano-Reinforced 3D-Fiber Metal Laminates Using Non-Destructive Techniques

5.1 Publication Statement

This chapter has been published as a peer-reviewed journal publication in the journal "Sandwich Structures and Materials" (IF: 5.616; CiteScore: 5.1 (Scopus; 2020)), by B. Soltannia as the 1st author. The title is "Static and dynamic characteristics of nano-reinforced 3D-fiber metal laminates using non-destructive techniques". The paper consists of 32 single-spaced single column pages and was electronically published in May 2020 (it's still *in*-press and to be indexed) [3]. A brief and preliminary version of this work was also presented and published in the proceedings of the 11th Canadian-International Conference on Composites (CANCOM2019) by B. Soltannia as the 1st author. The title of the conference paper is "Vibration Characteristics of Multi-Wall Carbon Nanotubes (MWCNT) Reinforced 3D-Fiber Metal Laminates (3D-FML)". It consists of eight single-spaced single-column pages and was selected as one of the five best runner-up conference papers [4]. Note that Sections 5.2 'Nomenclature' and 5.8 'Finite Element Modeling', and Subsection 5.9.4 'Finite Element Results' are not part of the published journal article and were added to this chapter later. Also, note that Sections 5.3 'Introduction' and 5.9 'Results and Discussion', as well as subsection 5.7.4 'Bending Rigidity' have been updated.

5.2 Nomenclature

α	Slope of load-displacement curve ($\alpha=\boldsymbol{P}/\boldsymbol{\delta}$)
δ	Logarithmic decrement
δ_i	Natural logarithm of the ratio of the amplitudes of two successive oscillations
$\boldsymbol{\delta}$	Displacement in three-point bending tests
γ_n	n^{th} solution of the equation obtained by solving the constitutive equation of motion

	of a free-free prismatic beam using the separation of variable technique
μ	Mass per unit length
ξ	Damping ratio (damping coefficient also has been used interchangeably) ($\xi < \xi_c = 1$)
ξ_c	Critical damping ratio ($\xi < \xi_c = 1$)
ϕ	Phase angle
ω_0	Undamped angular natural frequency
ω_D	Damped angular natural frequency
A	Amplitude
a	Distance between the load P and the nearest support
b	Width (breadth) of the beam
D_{11}	Bending rigidity per unit width of the laminate in the longitudinal direction
d	Distance between the centroid of the face sheets ($d = t_f + t_c$)
E	Modulus of elasticity
E_f	Flexural modulus of the face-sheets
E_c	Flexural modulus of the core
f_n	Frequency of the n^{th} vibration mode
G	Shear modulus of the thick 3D-FGF or thick 3D-FML beam calculated based on G_P and G_C
G_P	Shear moduli of the pillars
G_C	Shear moduli of the core
$H(t)$	Hilbert transform of the function $u(t)$
h	Total thickness of the specimen

I	Cross-section moment of inertia about the bending axis
k	Individual ply (layer) index in the panel
L	Beam length
L_S	Span length
n	Total number of plies in the panel
P	One-half of the actual total load applied to the specimen
$\boldsymbol{P}$	Applied load in three-point bending tests
Q	Transformed stiffness matrix of each ply (layer) of the composite material
R	Bending rigidity of the beam
s	Span between nodal points
T_D	Oscillation period
t	Time
t_f	Thicknesses of the face-sheets
t_c	Thicknesses of core
$u(t)$	Deformation (displacement) function
$x_{(t)}$	Time (t) dependent motion of a single degree of freedom vibrating mass
Z_k	Distances measured from the mid-plane of the 3D-FGF or 3D-FML panels to the bottom of each plies (layers)
Z_{k-1}	Distances measured from the mid-plane of the 3D-FGF or 3D-FML panels to the top of each plies (layers)

5.3 Introduction

Fiber-reinforced polymer (FRP) composites offer superior specific strength, stiffness and durability compared to most metallic materials [162,163]. FRPs are corrosion resistant and highly tailorable materials. They also possess high energy absorption capacity and controllable damage mechanism [164–166]. These characteristics make them highly effective and desirable compared to many materials traditionally used in various applications [146,149,167–170]. As a result, FRPs are increasingly employed in primary and non-primary structural applications in the aerospace, infrastructure, marine, automotive, offshore/onshore oil and gas industries. Amongst the positive attributes of FRP composites is their favorable vibration damping capacity, which outperforms most other materials. This characteristic is an important feature of this class of materials, since excessive and unharnessed vibration in structures may result in undesirable consequences, such as unwanted noise and even failure of the structure. Such problems are often encountered in transport vehicle body components, airplane cabins, and train and subway enclosures.

Spanning several decades, vibration analyses of composite materials and structures (thin and thick laminates and sandwich configurations) have been the focus of multiple analytical, numerical and experimental studies [84]. In 1973, Noor [171] pointed out the inadequacies of available analytical models for evaluating the low-frequency response of simply-supported thick composite beams. Since then, several researchers have employed and modified the classical Rayleigh-Ritz method, which has often been used to evaluate the natural frequencies of thin or thick laminates and sandwich plates [172–174]. For instance, Hu et al. [32] analyzed the vibration response of twisted angle-ply laminated plates using the Rayleigh-Ritz method based on the Mindlin plate theory. In another work, Lei et al. [33] utilized the Ritz method to investigate the damping properties of functionally graded thin laminate composite plates, reinforced with carbon nanotubes

(CNT), with clamped boundary conditions. Chen et al. [34] used Galerkin's method to analyze the nonlinear vibration response of rectangular laminated composite plates. Kant and Swaminathan [35] developed a higher-order theory, considering through-thickness shear effects for analyzing the free vibration of sandwich plates. Tu et al. [36] formulated a finite element approach to model the vibration and bending characteristics of laminated and sandwich composite plates using a nine-node rectangular element formulated based on a higher-order shear-deformation theory, thereby accounting for the variation of the through-the-thickness shear.

Improving the damping characteristics of laminated or sandwich composite plates has also been explored experimentally by several researchers. The use of inherently damped materials and nanoparticles (NPs) as passive damping tools on the one hand, and the use of external damping sources as an active damping strategy on the other hand, have been found to generate the most effective approach for enhancing the dynamic damping properties of composite materials and structures. Zou et al. [42], Hajikhani et al. [43], Soltannia et al. [4,5], and De Cicco and Taheri [44] experimentally investigated the vibration characteristics of laminated and sandwich composite beams using nondestructive testing (NDT) techniques. Similarly, Cheraghi et al. [175] used the impulse excitation technique along with the use of piezoelectric sensors to establish the damping response of polyvinyl chloride (PVC) pipes. The accuracy of various methods for retrieving the damping coefficient from the acquired vibration data has also been explored by a few researchers [42,176,177].

Various approaches have also been explored to improve the material damping response. A notable example would be the approach adopted by Berthelot [146,178], Piollet et al. [179], and Fotsing et al. [180,181], who investigated the effect of entangled cross-linked fibers and interleaved viscoelastic layers (as inherently damped materials) in damping the vibration response

of laminate and sandwich composites. Sargianis et al. [182] demonstrated the use of naturally damped materials to augment the structural damping ratio of sandwich composite plates by 100%. They used balsa wood for the core and natural fibers to form the facial laminate constituents of their sandwich plates. They also incorporated a synthetic core material (Rohacell®51 WF) instead of the balsa core, achieving an impressive damping enhancement of 233% at the expense of a marginal loss of flexural bending rigidity (FBR).

The advantages of including small amounts of NPs to improve the mechanical and electrical properties of the matrix of laminated polymer composite structures and adhesives have been actively investigated by several researchers in recent years [1,2,45,124,125,183–185]. Ahmadi-Moghadam et al. [76] demonstrated that the use of chemically functionalized graphene nanoplatelets (G-Si) using silane coupling agent, can result in much greater improvement in the mechanical and fracture response of composite materials compared to non-functionalized GNP, due to chemical affinity of the functional group (Si) bonded to the surface of GNP, with the host resin, thus providing a stronger interface between each nanoparticle and some polymeric matrices. can result in much greater improvement in the mechanical and fracture response of composite materials compared to non-functionalized GNP. Liu et al. [74] investigated the effect of functionalized single-wall carbon nanotubes (SWCNT) on the damping properties of composite materials. DeValve and Pitchumani [186] experimentally investigated the effect of adding CNT on damping enhancement of carbon fiber reinforced polymer (CFRP) laminated composite beams. The addition of merely 1 to 2 wt% CNT improved the damping properties by 40 to 60%. Similarly, Khan et al. [187] showed that the inclusion of multi-wall carbon nanotubes (MWCNT) enhanced the damping properties of cantilever CFRP beams. They highlighted that the improved damping performance of their beams was a result of enhanced beam stiffness facilitated by the MWCNT.

Static and dynamic properties of the functionally graded polymers composite have also been investigated numerically and analytically by several researchers [188–190].

To establish the improvement gained in mechanical properties of composites by various approaches as briefly described above, many investigators have used traditional techniques such as those developed by the National Aeronautics and Space Administration (NASA) [191], or those described in various ASTM Standards [192,193]. In addition, several novel and mainly nondestructive approaches have also been developed by researchers. For instances, Viens and Johnson [176] discussed the effectiveness of using the dynamic excitation technique for evaluating the elastic properties of composites non-destructively. They demonstrated the utility of GrindoSonic devices [194] as an effective tool for evaluating the elastic properties of composite beams nondestructively and with acceptable accuracy.

At this juncture, and beside many other techniques to enhance stiffness-to-weight ratio by introducing high performance pseudo-ductile (HiPerDuCT) composites utilizing only FRP composite materials [83], it is worth mentioning some of the relatively recent efforts expended in developing more resilient, cost-effective and lightweight hybrid materials, notably, fiber-metal laminates (FMLs) [77,78]. FMLs are hybrid laminates consisting of thin alternating bonded layers of thin metallic sheets (e.g., aluminum or magnesium alloys) and fiber/epoxy [79]. FMLs were developed first in the early 1980s as a more cost-effective alternative to CFRP used in the aerospace industry. The first FML was ARALL (an acronym for aramid reinforced aluminum laminate), developed by a University of Delft student, Marissen, which consists of a layout of aramid fiber layers with aluminum layers [80]. Since these pioneering efforts, various FMLs have been developed and produced using different fiber types, such as carbon and aramid. A new rendition of conventional thin FMLs was recently introduced by Asaee and Taheri [81], thereafter

referred to as three-dimensional FLM (3D-FML). This class of FML has been demonstrated to possess exemplary characteristics compared to conventional FRPs and FMLs, especially from the perspective of crashworthiness and impact tolerance, as demonstrated in [82]. A 3D-FML is essentially a sandwich composite consisting of a novel 3D fiberglass fabric (3D-FGF), sandwiched between thin sheets of a lightweight metallic alloy (e.g., aluminum or magnesium alloys). Having lower density (almost one-third lower than aluminum and three-quarter lower than steel), and costing less compare to aluminum alloys, as well as possessing a high strength to weight ratio, makes magnesium alloys more suitable candidates for the fabrication of sandwich panels [195–197]. A schematic illustration of 2D- and 3D-FML beams are shown in Figure 5.1.

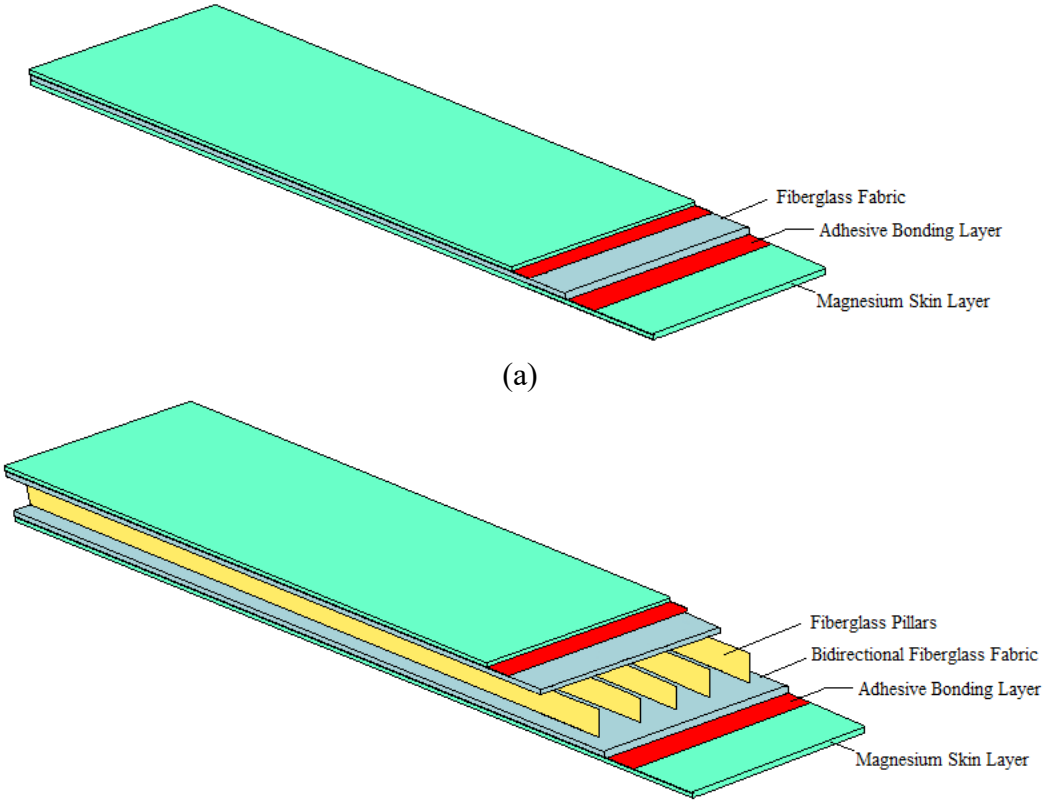

Figure 5.1 Schematic illustration of (a) 2D-FML and (b) 3D-FML beams.

The superior responses of various configurations of this class of 3D-FML under static and dynamic loading conditions have been demonstrated, promising the suitability of this type of FML in forming lightweight structural panels, especially for meeting recent weight reduction and thus fuel efficiency targets in the automotive industry [4,5,44,81], beside many other techniques to enhance stiffness-to-weight ratio by introducing HiPerDuCT composites utilizing only FRP composite materials [83].

5.4 Research Objectives of This Study

The work presented was prompted by the speculation that 3D-FMLs could offer a more damped vibration response compared to the conventional fiber-reinforced composites (shown in De Cicco and Taheri's work [26]), especially if their polymer matrix is reinforced with nanoparticles. Therefore, in the paper it has been demonstrated that comparatively, 3D-FMLs would offer superior stiffness-to-weight ratio to the material systems, thus reducing the overall material weight, thereby lowering the overall cost. Moreover, it was hypothesized that by strategically dampening the FML using nano-reinforced polymer composites, one could potentially improve the dynamic response of 3D-FMLs. By providing additional reinforcement using nanoparticles at strategic regions (e.g., matrix, interface, both, etc.), it was postulated that one could optimize the reinforcing effect of nanoparticle on the static and dynamic characteristics of 3D-FMLs, which to the best knowledge of the authors' had not been attempted previously. In other words, there are quite bit of investigation on the effect of nanoparticle reinforcement on the static and dynamic properties of polymer composite microbeams, beams and plates; also works done on static and dynamic properties of non-reinforced FRPs, as well as 2D- and 3D-FMLs using non-traditional techniques, however again to the best knowledge of the authors, no one has investigated all these subjects together as a whole. The conducted characterizations would help us

and the future researchers to produce a lightweight, cost-effective and resilient system for both static and dynamic loading applications. Therefore, it is important to understand and characterize the static and dynamic response of this new class of 3D-FMLs. As a result, attempts were made to establish an appropriate solution for a new class of material to produce proper static and dynamic performances with the aim of targeting structural applications in transportation industries.

Results of several investigations have revealed the superior mechanical response of 3D-FMLs to lateral and axial loading at various rates, see e.g. [81,82]. However, only a preliminary investigation has been conducted to assess the vibration characteristics of this interesting class of material system [4,5,44]. The latter study speculated that one could further improve the vibration response of 3D-FMLs by inclusion of suitable NPs. Therefore, the objectives of the present study are twofold. First, to investigate the different parameters that affect and govern the vibration response of 3D-FMLs. Under this objective, the 3D-FML configuration that would possess the highest damping and proper noise and vibration reduction attributes shall be identified. Secondly, the potential of enhancing the vibration characteristics of 3D-FMLs by incorporating NPs within the hybrid system shall also be explored. In this regard, an attempt was made to improve the material damping characteristics by including NPs within the core and/or interface layers of the hybrid material system to establish the 3D-FML configuration that would generate the most effective damping response. For that, two types of nanocarbon particles (NCP), namely MWCNT and functionalized GNP (G-Si) were employed, thereby establishing an effective nanocomposite for enhancing the vibration response of 3D-FMLs. The results obtained by various NDT characterization approaches are presented and compared with a traditional technique in order to verify the accuracy of NDT methods and equipment. Figure 5.2 shows a graphical illustration of

the topics considered in the present experimental investigation that are described in detail in the remaining parts of this paper.

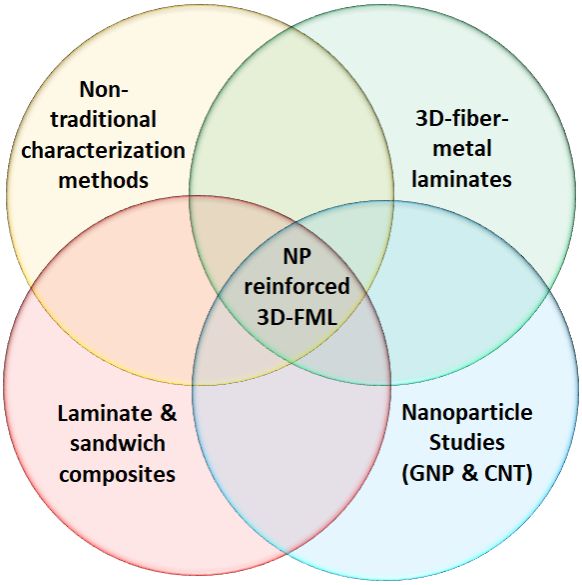

Figure 5.2 Schematic of research subjects considered in the present work.

5.5 Materials and Fabrication

5.5.1 Materials

Preform 3D-FGF was procured from China Beihai Fiberglass Co. (Jiujiang City, Jiangxi, China). For 3D-FMLs with metal face sheets, magnesium alloy sheets (type AZ31B-H24) with thickness of 0.5 mm were purchased from MetalMart International (Commerce, CA, USA). A hot-cure epoxy resin was used for fabricating the 3D-FGF constituents. This two-part resin system was composed of bisphenol-A based Araldite LY 1564 resin and Aradur 2954 cycloaliphatic polyamine hardener (Huntsman Co., West Point, GA, USA). For bonding magnesium face sheets to 3D-FGF cores, a two-part cold-cure epoxy resin was applied at the interface (105 resin and 206 hardener, West System, Bay City, MI, USA). To facilitate certain material characterization tasks an alternative core material was employed, which was a two-part urethane foam with free rise density of 128 kg/m^3 (8 lb/ft^3) supplied by US Composites (West Palm Beach, FL, USA). To serve

as a baseline for comparison with various composite sandwich configurations, as well as for the fabrication of some samples, an aluminum (Al) plate material (type 6061-T6) with thickness of 4 mm was obtained from a local supplier.

Two types of NCP were chosen to be dispersed within the epoxy resins. They were (i) functionalized GNP (type GNP-M-25) with an average diameter of 25 μm, thickness of 6 nm, and surface area of 100 m^2/g (XG Science Ltd., Lansing, MI, USA); and (ii) MWCNT with purity greater than 95% and outer diameters ranging between 5 and 15 nm (US Research Nanomaterials, Inc., Houston, TX, USA).

5.5.2 Specimen Manufacturing

5.5.2.1 3D-FGF Specimens

3D-FGF was utilized in two forms: (i) 3D-FGF was used to generate monolithic 3D-FGF sandwich plates; and (ii) 3D-FGF formed the core region of the magnesium alloy faced 3D-FML panels investigated in this study. In either case, to create panels, the hot-cure epoxy resin was brushed onto the fabric. It should be mentioned that the 3D-FGF, which in its dry state is flat, 'awakens' upon resin impregnation, creating several rows of identical sized channels (or cavities) within the thickness of the fabric. Each resin-impregnated fabric was then cured in an oven at 60°C for 2 hours and then at 120°C for 8 hours. After curing, at least three beam specimens were cut from each panel. 3D-FGF specimen dimensions were 200 mm by 20 mm by 4 mm, referring to the beam length, L, width, b, and thickness, h, respectively, the same as for all other specimens unless specified otherwise (e.g., in case of foam core sandwich beams). Preform 3D-FGF specifications have been listed in Table 5.1 [198]. Note that preform warp direction aligned with the specimen longitudinal direction. Also, picture of preform 3D-FGF and its resin impregnated composite, as well as 3D-FGF with different thicknesses have been shown in Figure 5.3 [198].

Table 5.1 Preform 3D-FGF specifications [198].

Area Weight (g/m^2)	Core Thickness (mm)	Density of Warp (ends/cm)	Density of Weft (ends/cm)	Tensile strength Warp (n/50mm)	Tensile strength Weft (n/50mm)
740	2	18	12	4500	7600
800	4	18	10	4800	8400
1480	10	15	8	6800	12000

(a) (b) (c)

Figure 5.3 3D-FGF images: (a) preform 3D-FGF; (b) its resin impregnated composite; and (c) 3D-FGF with different thicknesses. [198]

5.5.2.2 3D-FML Specimens

To form the 3D-FML panels, the processed 3D-FGF panels were sandwiched between a pair of magnesium sheets. The sheets were initially roughened by grit-blasting and cleaned with an air gun, followed by acetone washing and air-drying. They were then bonded to the 3D-FGF core using the cold-cure epoxy resin. Resulting sandwich panels were cured for at least 24 hours at room temperature under vacuum to ensure high-quality interface-bonding. Additional details on the fabrication procedure of the 3D-FMLs can be found in [81]. Specimens were appropriately cut into dimensions using a diamond blade saw, having length and width of 200 mm and 20 mm, and total thickness of ~5.5 mm and ~11.5 mm for 4 mm and 10 mm 3D-FGFs, respectively. To identify

their flexural bending rigidity, three-point bending tests were conducted according to the ASTM D790 standard [199].

5.5.2.3 Foam Core Sandwich Specimens

In order to establish the elastic modulus of the main 3D-FGF constituents (i.e., the biaxial fabrics forming the two outer panels of the 3D-FGF), a series of sandwich specimens were fabricated in conformance with the ASTM D7249 standard [200]. For that, first, the foam core section of the sandwich panel was fabricated by pouring the two-part urethane foam (1:1 mix) in between the space created between two clamped aluminum plates, separated by 4 mm spacers. The foam-mating surfaces of the plates were covered with non-porous Teflon sheets. The foam was let to cure at room temperature for 24 hours. Subsequently, two pieces of 3D-FGF fabrics were resin impregnated (using the hot-cure epoxy system) and then placed in an oven for curing while applying vacuum bagging so that the 3D-FGF fabrics would remain in their 2D state. Then, the foam panel was sandwiched in between the two fabrics, using the cold-cure resin system for bonding. The resulting assembly was cured at room temperature under vacuum, yielding the final sandwich configuration required for testing. Appropriately sized specimens fabricated in conformance with the ASTM D7249 standard [200] having length, width and total thickness of 275 mm, 20 mm and 8.5 mm, respectively, were extracted from the fabricated foam core sandwich plates to establish the elastic modulus of the biaxial fabrics forming the two outer panels of the 3D-FGF, conducting four-point bending tests according to the pertinent ASTM standard [200]. Specimens were cut using a diamond blade saw.

5.5.2.4 NCP Reinforced 3D-FGF and 3D-FML Specimens

In order to create NCP reinforced 3D-FGF and 3D-FML specimens, NCP modified resin was first prepared as follows. For each type of NCP, filler particles with 1 wt% (by weight

concentration) were dispersed in the resin system using a mechanical stirrer set at a speed of 2000 rpm for 10 minutes. Then, the NCP resin slurry was calendered using a three-roll mill homogenizer (Torrey Hills Technologies, San Diego, CA, USA). The roller gaps were set at 30 μm using a feeler gauge. In this study, the roller speed was set at a constant rate of 174 rpm. To maximize the quality of dispersion, calendering was conducted seven times. The curing agent was subsequently blended with the resin slurry using the stirrer at a speed of 400 rpm for 4 to 6 minutes. The mixture was then degassed under 711 Torr (28" Hg) vacuum for 2 to 3 minutes. The interested reader is referred to [76,125] for information on NCP functionalization and particle dispersion and calendaring processes.

To study the morphology of NCP modified 3D-FGF-epoxy panels, a jeweler saw was used to extract samples from several panel locations for field emission scanning electron microscopy (FESEM) using a S-4700 device by Hitachi High-Technologies (Tokyo, Japan). Samples for microscopic analysis were palladium-gold coated using a sputtering device (Model ACE200, Leica, Wetzlar, Germany).

5.5.2.5 Specimen Configurations and Nomenclature

Various specimen types were fabricated as per the procedures described in the preceding sections. The different specimen configurations are listed in Table 5.2 along with the abbreviations used to identify samples throughout this study. In the remainder of this document, data is also presented using an abridged nomenclature to ease the identification of specimens or groups thereof, in addition to the specimen identifiers (ID) listed in Table 5.2. For example, MWCNT-4-3D-FML refers to 3D-FML specimens having 4 mm thickness and being reinforced with MWCNT. The length and width of all beam specimens reported in this table are 200 mm by 20 mm, respectively.

Table 5.2 Specimen configurations and nomenclature.

ID	Material	Core thickness	Resin modification	Filler/resin in core	Filler/resin at interface
Al	Al 6061-T6	4 mm			
3D-FML1	3D-FML	4 mm	Neat	0 wt%	0 wt%
3D-FML2	3D-FML	4 mm	GNP	0 wt%	1 wt%
3D-FML3	3D-FML	4 mm	GNP	1 wt%	0 wt%
3D-FML4	3D-FML	4 mm	GNP	1 wt%	1 wt%
3D-FML6	3D-FML	4 mm	MWCNT	0 wt%	1 wt%
3D-FML7	3D-FML	4 mm	MWCNT	1 wt%	0 wt%
3D-FML8	3D-FML	4 mm	MWCNT	1 wt%	1 wt%
3D-FML9	3D-FML	10 mm	Neat	0 wt%	0 wt%
3D-FML10	3D-FML	10 mm	GNP	0 wt%	1 wt%
3D-FML11	3D-FML	10 mm	GNP	1 wt%	0 wt%
3D-FML12	3D-FML	10 mm	GNP	1 wt%	1 wt%
3D-FML14	3D-FML	10 mm	MWCNT	0 wt%	1 wt%
3D-FML15	3D-FML	10 mm	MWCNT	1 wt%	0 wt%
3D-FML16	3D-FML	10 mm	MWCNT	1 wt%	1 wt%
3D-FGF17	3D-FGF	4 mm	Neat	0 wt%	
3D-FGF18	3D-FGF	4 mm	GNP	1 wt%	
3D-FGF19	3D-FGF	4 mm	MWCNT	1 wt%	
3D-FGF20	3D-FGF	10 mm	Neat	0 wt%	
3DFGF21	3D-FGF	10 mm	GNP	1 wt%	
3D-FGF22	3D-FGF	10 mm	MWCNT	1 wt%	

5.6 Experimentation

5.6.1 Vibration Testing

The instrumentation used to acquire vibration signals employed contact type and non-contact type techniques. As illustrated in Figure 5.4, the contact type device was a GrindoSonic instrument (GS) model MK5i (Leuven, Belgium). The non-contact type device was a laser-Doppler vibrometer (LDV) (Model LP01, Optical Measurement System, Laguna Hills, CA, USA). Also shown in Figure 5.4 are two prismatic low-density foam sponges supporting a specimen during testing. This setup mimics a free-free boundary condition. A light-weight hammer, consisting of a

steel ball attached to a thin wooden rod, was used to excite the specimens, as per the GS technical documentation [194] and NASA Technical Memorandum 104629 [176].

The prismatic sponge supports were located to coincide with specimens' fundamental vibration mode nodal points. The GS instrument has a small and highly sensitive probe tip (see Figure 5.4), which was positioned in light contact with the specimens, close to one of the free vibration nodal points, where the vibration amplitude vanishes. The span between nodal points (s), which are distanced equally from each specimen extremity, can be calculated using Equation (5.1) [194,201].

$$s = 0.224\, L \tag{5.1}$$

where L is the beam length. A distance of 45 mm between a support and the corresponding specimen extremity was adjusted for all specimens. The correctness of this distance was confirmed by an eigenvalue finite element analysis conducted earlier by this research group [44,82].

Several researchers demonstrated that data with satisfactory accuracy can be obtained via GS measurements [42,176,177]. However, as mentioned in NASA Technical Memorandum 104629 [176], GS may produce inaccurate results in environments with significant external noise. Inaccurate results are also obtained when a specimen is excited such that higher vibration modes, as opposed to the fundamental mode, are imposed. To mitigate these anomalies, present experiments were conducted in a quiet room. Moreover, all specimens were excited by tapping them at a consistent location (i.e., at a point between the two supports, close to the center span of each specimen).

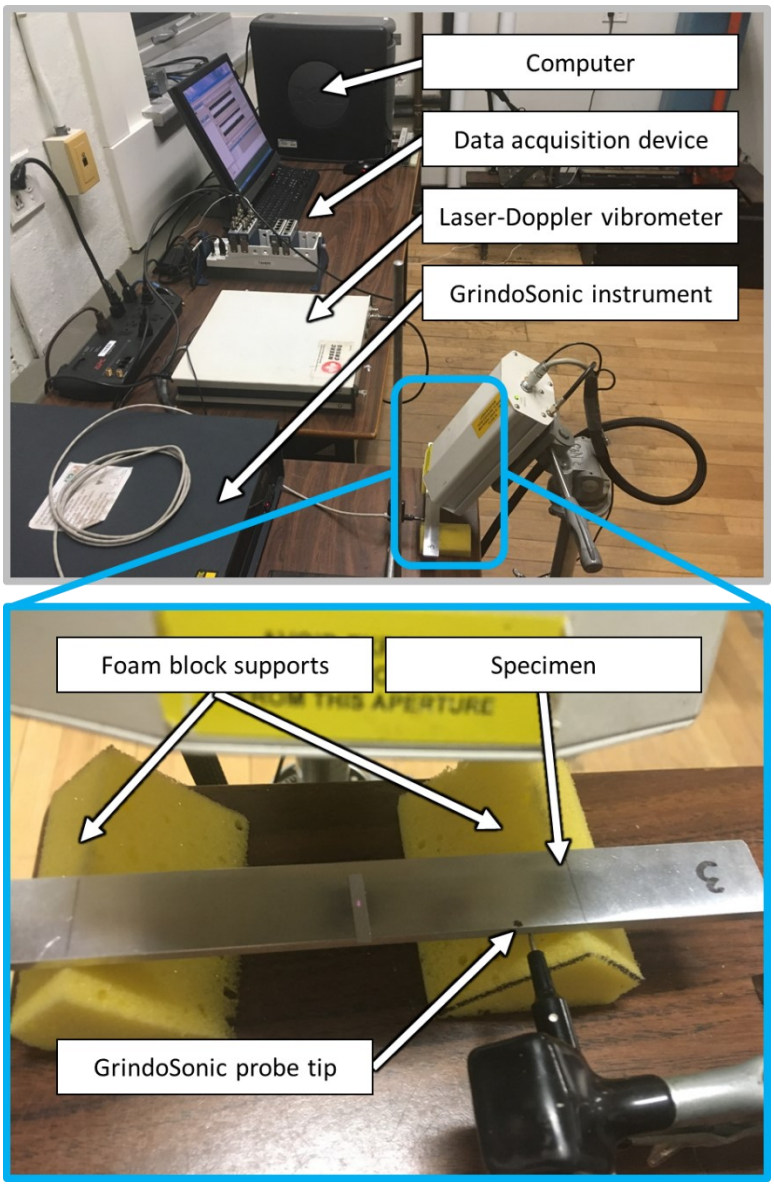

Figure 5.4 Experimental test setup for recording vibration signals of free-free supported specimens using the GS and LDV.

The outputs from GS and LDV are in the form of an electric potential (voltage), proportional to the amplitude of the excitation. After specimen excitation, the software embedded in the GS automatically analyzes the specimen's oscillatory motion transient response and calculates and displays the specimen's fundamental frequency. However, in order to determine the material damping ratio, the entire oscillation spectrum needs to be captured. Therefore, the GS device was connected to a data-acquisition system (cDAQ-9172, National Instrument, Austin, TX, USA) and

a personal computer (PC) running the Signal Express software (2010, National Instruments, Austin, TX, USA) to record the entire oscillatory spectrum at a 100 kHz sampling rate. The recorded data was then post-processed using the LabVIEW software (2010, National Instruments). For the LDV a laser reflective tape was applied to the specimen to increase the reflected signal intensity. Modal experiments were repeated at least nine times.

5.6.2 Bending Rigidity Testing

The FBR of the various specimens was evaluated employing three- and four-point bending tests according to the pertinent ASTM standards [199,200]. A servo-hydraulic testing machine equipped with a digital electronic controller was employed for this purpose (2518-610, MTS, Eden Prairie, MN, USA). Figure 5.5 illustrates the experimental setup. The mid-span deflection of the test specimens was acquired using a laser extensometer (LE-05, Electronic Instrument Research, Irwin, PA, USA). Experimental data in terms of load and deflection was recorded using a PC.

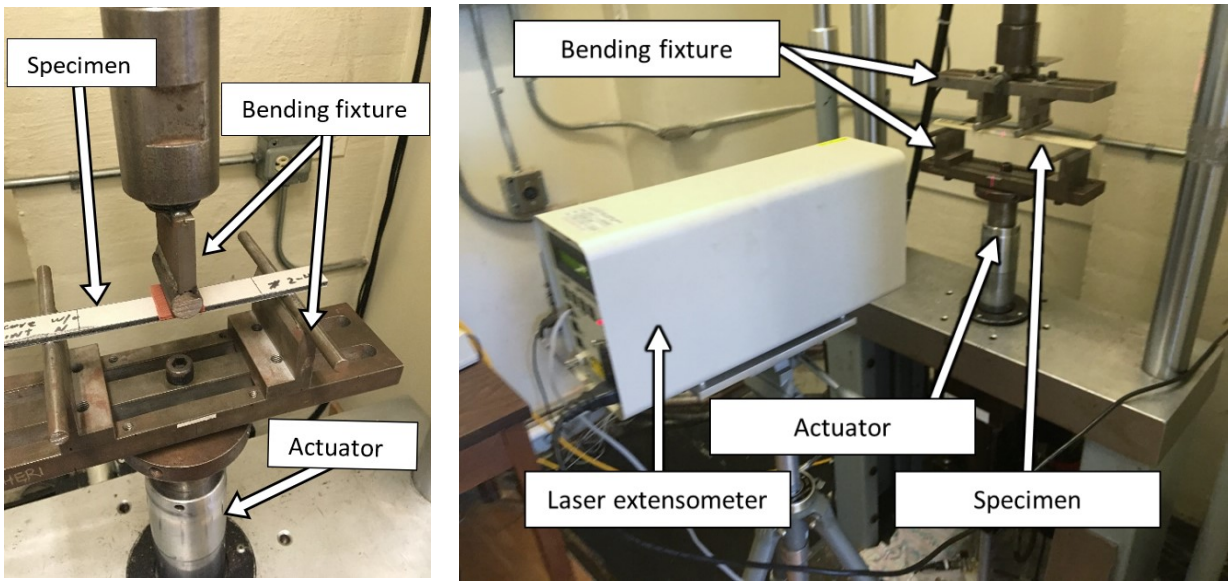

(a) (b)

Figure 5.5 (a) Three- and (b) Four-point bending rigidity test setup.

5.7 Data Analyses

5.7.1 Fundamental Frequency

The frequencies acquired experimentally using the GS and LDV were contrasted with results from the available closed-form solution given by Equation (5.2). The latter was explained extensively in various sources [4,5,44,146,178,201,202].

$$f_n = \frac{1}{2\pi}\left(\frac{\gamma_n}{L}\right)^2 \sqrt{\frac{R}{\mu}} \quad \text{with} \quad R = \begin{cases} EI & \text{for homogeneous beams} \\ bD_{11} & \text{for composite beams} \end{cases} \tag{5.2}$$

where f_n is the frequency of the n^{th} vibration mode; γ_n is the n^{th} solution according to Equation (5.3) [201]; In this equation, R is the bending rigidity of the beam, and its value, EI, for an isotropic (homogeneous) beam, is replaced by bD_{11} for orthotropic (composite) beam based on homogenization model of material (rule of thumb), where b is the width of the beam, and D_{11} (dynamic stiffness) is the bending rigidity per unit width of the laminate in the longitudinal direction; μ is the mass per unit length; E is the modulus of elasticity; I is the cross-section moment of inertia about the bending axis.

$$\cos\gamma \cosh\gamma = 1 \tag{5.3}$$

Equation (5.3) is obtained by solving the constitutive equation of motion of a free-free prismatic beam using the separation of variable technique. Since in this study the fundamental bending frequency of the beam is of interest, only the first value for γ_n was computed numerically, yielding $\gamma_1 = 4.73$. Moreover, D_{11} (apparent stiffness (Equation (5.10)) and shear-free stiffness (Equation (5.14))) obtained from the experimental data (i.e., load-deflection curves of 3-point bending tests) were contrasted with the analytical solution for D_{11} (dynamic stiffness) back-

calculated from Equation (5.2), knowing fundamental frequencies obtained experimentally using GS. [146,149,167–170].

5.7.2 Damping Ratio

Knowledge of a material's damping properties is vital for controlling the vibration response of a given structure that is subjected to vibratory loading. By knowing the damping ratio and natural frequencies, one can simplify a complex vibration analysis into a much simpler equivalent quasi-static analysis. However, conventional techniques used to evaluate the material damping coefficient are very time-consuming, as discussed by Naghipour et al. [203], who used various characterization techniques to identify the damping coefficient of fiber-reinforced glue-laminated timber beams.

The evaluation of the damping coefficient involves solving the governing constitutive equation of the damped oscillatory motion of a system, represented by Equation (5.4) [4,5,44,146,201]:

$$x_{(t)} = Ae^{-\xi\omega_0 t}\, cos(\omega_{\mathrm{D}} t - \phi) \tag{5.4}$$

where $x_{(t)}$ is the time (t) dependent motion of a single degree of freedom vibrating mass; A *is* the amplitude; ξ is the damping ratio ($\xi < \xi_c = 1$), with ξ_c being the critical damping ratio; ϕ, ω_0 and ω_{D} are the phase angle, undamped and damped angular natural frequency, respectively. ω_0 and ω_{D} are related to each other according to Equation (5.5).

$$\omega_{\mathrm{D}} = \omega_0\sqrt{1-\xi^2} \tag{5.5}$$

It should be noted that in a damped vibrating system where $\xi < \xi_c = 1$, the amplitude of motion is bound between two exponential curves that form the so-called 'signal envelope'. The half-symmetry envelope of typical signals is illustrated in Figure 5.6.

The damping coefficient, ξ, can be determined using the logarithmic decrement, δ, of the signal over an oscillation period, T_D, using Equation (5.6).

$$\xi = \frac{\delta_i}{\sqrt{4\pi^2+\delta_i^2}} \tag{5.6}$$

where δ_i is the natural logarithm of the ratio of the amplitudes of two successive oscillations. To improve accuracy, the damping ratio can be evaluated over multiple oscillation periods instead of over only one period. The logarithmic decrement and damping coefficient were computed using LabVIEW, employing exponential curve fitting and extraction of curve parameters (power and coefficients).

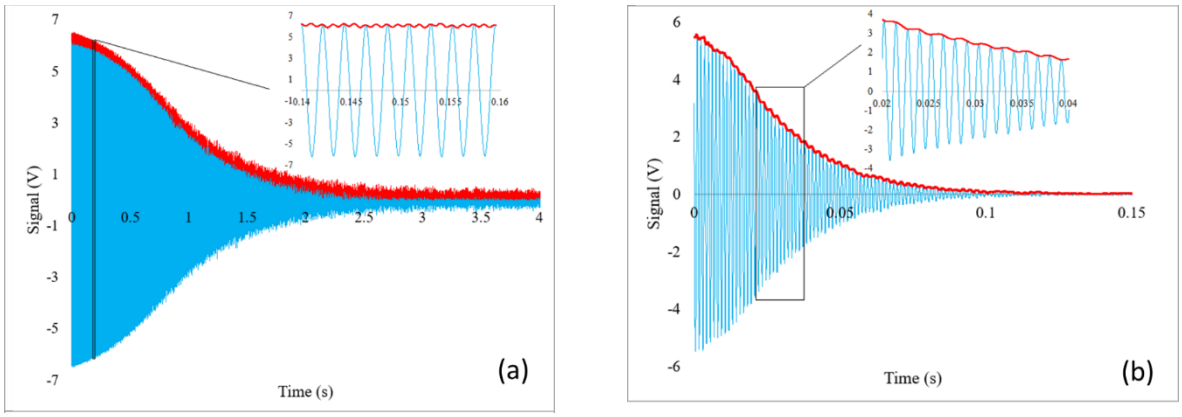

Figure 5.6 Typical vibration signals and the representative signal envelopes for (a) aluminum and (b) 1% GNP-reinforced 3D-FML specimens (GNP in both core and interface).

5.7.3 Vibration Signal Extraction and Analysis

As mentioned earlier, GS and LDV were used to obtain the fundamental frequency of the beam. The software associated with each instrument calculates the fundamental frequency by measuring the time elapsed between two peak amplitudes of a decaying vibration signal. The results from the instruments were compared against the values obtained from the power spectrum of the entire signal using the 'Spectral Measurements' subroutine of LabVIEW, which is based on

the aforementioned analytical equations. In other words, the subroutine takes the vibration signal from GS and LDV, and yields the amplitude of each frequency of the signal spectrum by employing the Fast Fourier Transform algorithm. The fundamental frequency of the signal spectrum is indicated by the peak amplitude, as illustrated in Figure 5.7.

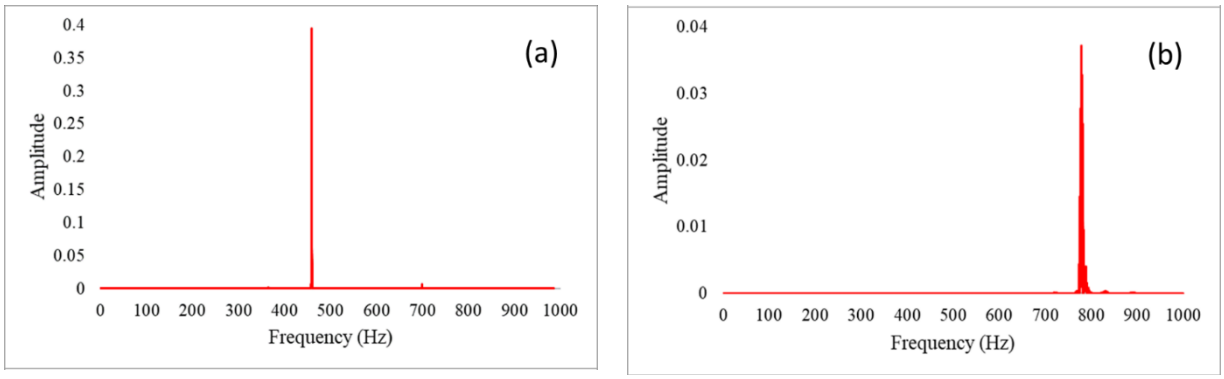

Figure 5.7 Power spectrum of: (a) Aluminum; (b) 3D-FML specimens with 1% GNP-reinforced core and interfaces.

To calculate the damping coefficient, the signals were first filtered in LabVIEW with a bandpass of ±30 Hz to mitigate noise. Then the filtered signal envelope was retrieved using the Hilbert transform through the procedure described by Cheraghi et al. [175], using the following mathematical operation:

$$H(t) = \frac{1}{\pi}\int_{-\infty}^{+\infty} u(\tau)\frac{\chi(\tau)}{t-\tau}d\tau \tag{5.7}$$

where $H(t)$ is the Hilbert transform of the function $u(t)$. In practice, if the envelope being considered has a complex number, its real part includes the signal amplitude and the imaginary part contains the Hilbert operator (as it has been explained and implemented in LabVIEW by Yang et al. [204]). Finally, the averaged damping coefficient was calculated based on the logarithmic decrement of 50 successive oscillatory points of the signal within the envelope. Since the damping coefficient of aluminum is significantly smaller than that of 3D-FML, the logarithmic decrement

of the signals within two different periods were used in calculating the damping coefficient. In other words, the signal within a 3-second window was considered for the aluminum specimens while the signals within a window of 0.1 seconds was considered for the other specimen types.

5.7.4 Bending Rigidity

The specimen bending rigidity was calculated based on the experimental data and compared to analytical results. Equations (5.8) and (5.9) relate the displacement of a simply-supported 3- and 4-point bending specimens to the applied load, respectively [205].

$$\delta_{\max} = \frac{Pa}{48EI}(3L_S^2 - 4a^2) \tag{5.8}$$

$$\delta_{\max} = \frac{Pa}{24EI}(3L_S^2 - 4a^2) \tag{5.9}$$

where P is the actual total applied load to the specimen in case of 3-point bending, and one-half of the actual total load applied to the specimen in case of 4-point bending; L_S is the span length; and a is the distance between the load P and the nearest support.

Substituting for $EI = D_{11}b$ (for the composite specimens), and $a = L/2$ in Equation (5.8) and $a = L/3$ in Equation (5.9), and solving for D_{11}, we obtain Equations (5.10) and (5.11).

$$D_{11} = \frac{1}{48}\left(\frac{L^3}{b}\right)\alpha \tag{5.10}$$

$$D_{11} = \frac{23}{1296}\left(\frac{L^3}{b}\right)\alpha \tag{5.11}$$

where α is $\boldsymbol{P}/\boldsymbol{\delta}$, or the slope of load-displacement curve.

On the other hand, one can also calculate the analytical value of the flexural modulus of the face-sheets based on bending rigidity (per unit width) employing the mechanics of material-based expression in Equation (5.12) [170]:

$$D_{11} = \frac{E_f t_f^3}{6} + \frac{E_f t_f d^2}{2} + \frac{E_c t_c^3}{12} \tag{5.12}$$

where t_f, t_c, E_f and E_c are the thicknesses and flexural modulus of the face-sheets and core, respectively, and d is the distance between the centroid of the face sheets (i.e., $d = t_f + t_c$).

Substituting Equation (5.11) into Equation (5.12) and solving for E_f yields the flexural modulus of the face sheets as per Equation (5.13), used to complete Table 5.3. The detail of testing method to identify α has been explained in Section 5.6.2. In this Equation, the value of E_c has been obtained from [82].

$$E_f = \frac{\frac{23}{1296}\frac{L^3}{b}\alpha - \frac{E_c t_c^3}{12}}{\frac{t_f^3}{6} + \frac{t_f (t_f + t_c)^2}{2}} \tag{5.13}$$

5.8 Finite Element Modeling

The commercial software package LS-DYNA was used to conduct finite element analyses and to identify the frequency response (**f_{FEM} (Hz)**) of homogenous (aluminum) and non-homogenous (3D-FGF and 3D-FML) beam specimens mentioned in this study. Eight-node isoparametric (brick) elements with reduced integration were used to simulate all specimens. To obtain the fundamental frequency of each specimen, a linear eigenvalue analyses was carried out.

A finer mesh size typically improves the accuracy of modeling results, and hence, a mesh refinement study should be performed to establish acceptable accuracy while maintaining

computational efficiency. In the present study, the mesh size, as seen in Figure 5.8, was adopted based on the De Cicco and Taheri's work [44].

In case of 3D-FGF or 3D-FML all components were modeled individually, giving the entire model orthotropic properties, i.e., in case of 3D-FMLs, plies, pillars, magnesium skins and bonding adhesives were simulated to build up the whole model. To demonstrate perfect bonding between each layer forming a specimen, all constituent layers were tied to each other at their contact nodes. In the case of plies and pillars consisting of fiberglass fabric, actual orthotropic material properties, calibrated with De Cicco and Taheri's work [44], were implemented (where applicable) to account for material anisotropy of 3D-FGFs and 3D-FMLs. An example of a K-file used to conduct finite element analyses and to identify the frequency response (f_{FEM} **(Hz))** of homogenous (aluminum) and non-homogenous (3D-FGF and 3D-FML) beam specimens mentioned in this study is provided in Appendix III.

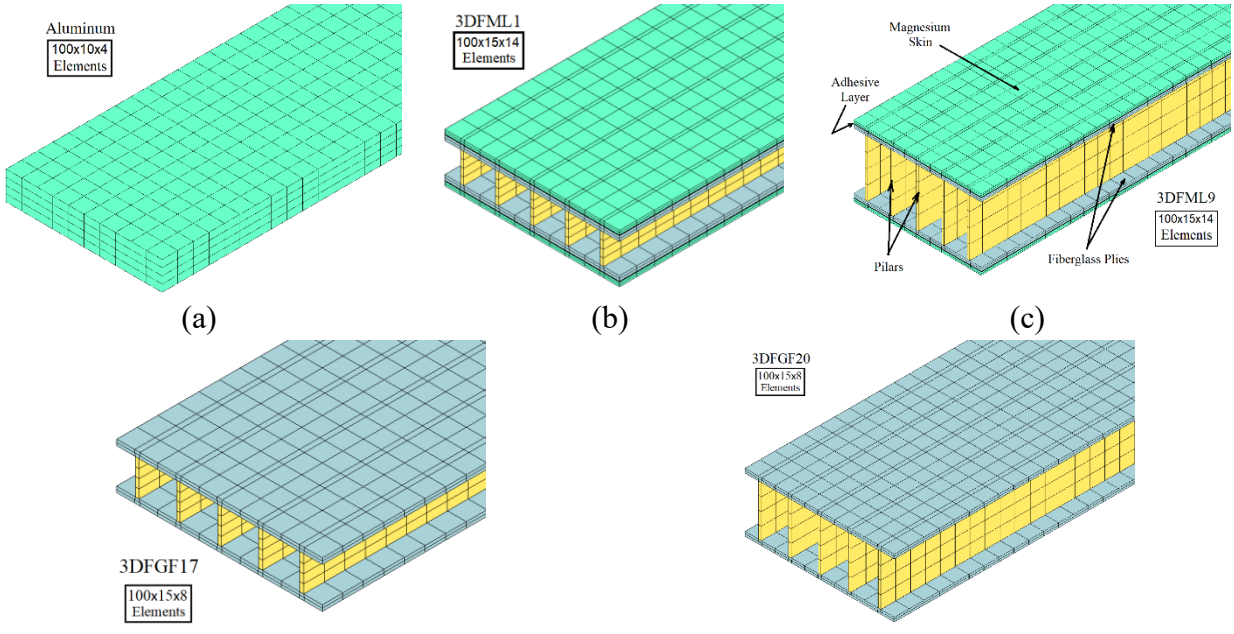

Figure 5.8 Mesh representation used for finite element analyses: (a) Aluminum (b) 3D-FML1 (c) 3D-FML9 (d) 3D-FGF17 (e) 3D-FGF20

5.9 Results and Discussion

The results of the experiments and related analyses are presented in the present section. It should be noted that at least nine vibration tests (modal experiments) were conducted on each specimen; therefore, the presented results for each group of specimens are the average of at least 27 tests (test were performed at least in triplicate per specimen group).

5.9.1 Bending Rigidities

The results of 3-point bending rigidity were used as a parameter to normalize the main results of this investigation, i.e., frequency and damping ratio values. The D_{11} values (apparent stiffness (Equation (5.10)) and shear-free stiffness (Equation (5.14))) obtained from the experimental load-deflection data (i.e., load-deflection curves of 3-point bending tests), and theoretically calculated values of D_{11} (dynamic stiffness), back-calculated from Equation (5.2), knowing fundamental frequencies obtained experimentally using GS, are illustrated in Figure 5.9.

It should be noted that Equation (5.10), which was used to give apparent stiffness based on empirical solutions for the flexural modulus, is based on a formulation that homogenizes the face sheets and core constituents of the 3D-FGF, yet, both the face sheets and core are inhomogeneous materials. In fact, in preform 3D-FGFs, the fibers (or pillars) in the core region of the 3D-FGF, that attach the two biaxial facial fabrics (on either side), have varying distribution in the two orthogonal directions. This degree of inhomogeneity increases in case of resin impregnated 3D-FGFs reinforced with or without NCP, especially when only one of the core or face sheets are NCP reinforced. Moreover, the equation does not consider the presence of any voids or non-uniformity in resin distributions and potential resin-rich pockets. Therefore, the simplifying assumptions used in developing the empirical solution affect the calculated value of the flexural rigidity of the complex hybrid composites considered in this study and are seen to be the cause for discrepancies

noted in Figure 5.9. Moreover, the approach described above is based on Euler-Bernoulli theory and does not account for potential shear deformation. In general, short span sandwich beams may experience shear deformation depending on the span to depth ratio and also the degree of orthotropy of the overall beam material. Therefore, when ignoring shear deformation, relatively large discrepancies were produced when calculating the bending rigidity of the thicker beams via Equation (5.10). To rectify this issue, Equation (5.14), which is provided in a NASA report [191] and accounts for shear effects, may be employed for calculating the shear-free D_{11} (solving equation (31) on page 12 of the NASA report). This D_{11} parameter represents the deflection of a material with equal moduli in both tension and compression [191].

$$D_{11} = \frac{0.2083\alpha L^3 Gh}{10Gbh - 3\alpha L} \tag{5.14}$$

where h is the total thickness of the specimen; and G is the shear modulus of the thick 3D-FGF or thick 3D-FML beam calculated based on G_P and G_C, i.e., the shear moduli of the pillars and core, respectively, with the values provided in [82].

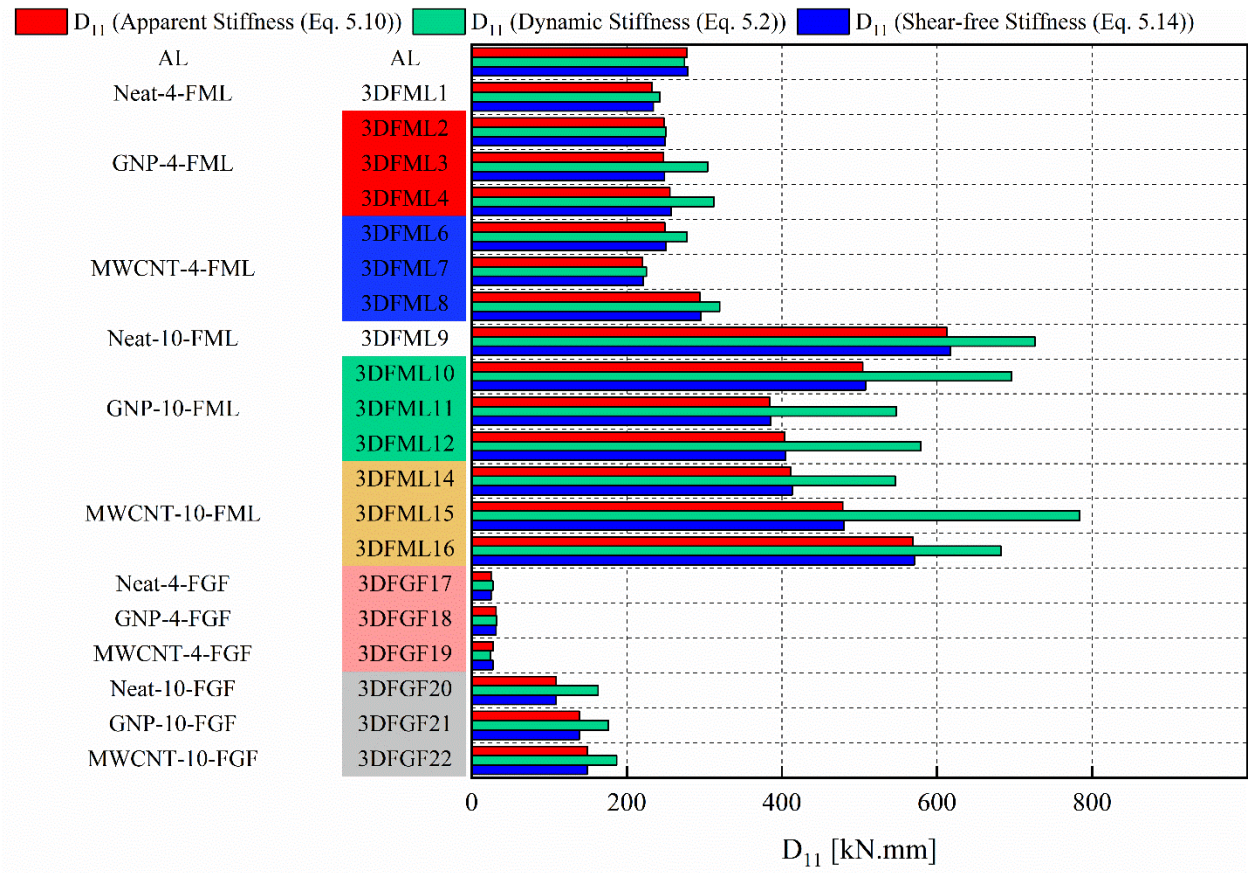

Figure 5.9 Specimen flexural bending rigidity obtained theoretically and experimentally via Eqs. (5.2), (5.10) and (5.14).

Values of D_{11} for dynamic stiffness were calculated through back substituting the experimental values of frequencies, directly obtained using GS, into Eq. (5.2). In contrast, D_{11} for apparent stiffness from Eq. (5.10) and shear-free stiffness from Eq. (5.14) were determined based on experimental values of α which is P/δ (the slope of load-displacement curve) obtained through 3-point bending tests.

It is also worth mentioning that other researchers studied vibration of SWCNT reinforced composite beams resting on Winkler-Pasternak elastic foundation considering first-order shear

deformation theory (FSDT), using shear correction factor [206–208]. The equivalent properties of nano-reinforced composite polymers can be calculated using a rule of mixture approach.

As stated earlier, sandwich specimens were also constructed for the purpose of establishing the flexural elastic modulus of the biaxial face sheets of the 3D-FGF in their original (neat) form and when the fabric is reinforced with GNP and MWCNT. The values of the evaluated modulus of elasticity are reported in Table 5.3. This information is required for conducting further analyses, e.g., in finite element modeling.

Table 5.3 Modulus of elasticity of baseline aluminum material and 3D-FGF facial fabrics with and without NCP reinforcement.

Material	E_f **(GPa)**
Al	70.00 ± 0.00
Neat fabric	9.32 ± 1.07
GNP-reinforced fabric	12.93 ± 3.38
MWCNT-reinforced fabric	18.05 ± 6.16

5.9.2 Fundamental Frequencies

The results of the experimentally measured frequencies by GS and LDV are tabulated in Table 5.4, along with values calculated using the analytical approach. The analytical results are in agreement with the experimental data. In addition, normalized results are depicted in Figure 5.10. To provide a better perspective of the relative and unbiased performance of the materials, data were normalized in the following manner. Results were first divided by their respective bending rigidity, and then normalized with respect to the value for the 3D-FML with neat resin (non-reinforced) and 4 mm thickness. Moreover, due to the good correlation amongst the frequency results seen in Table 5.4, only normalized frequency results obtained by GS are included in Figure 5.10 for clarity.

The normalized fundamental frequency of 3D-FMLs shown in Figure 5.10 is lower than that of 3D-FGFs, because in the case of 3D-FML its 3D-FGF component has been sandwiched and bonded between two thin sheets of magnesium. The data further indicates that the influence of NCP reinforcement on the fundamental frequencies, *f*, is marginal in 3D-FML specimens. In few cases, the inclusion of NCP slightly affected the fundamental frequencies negatively, i.e., *f* values were slightly reduced in case of MWCNT inclusion. This can be attributed to agglomeration of NPs as it is shown in Figure 5.12 (b). To further examine the influence of NCP reinforcement in 3D-FML specimens, resultant fundamental frequencies are presented as a function of the constituent(s) that was/were reinforced, and compared to the frequency of aluminum, as illustrated in Figure 5.11. The results presented in this figure indicate that NCP reinforcement affected the fundamental frequency of specimens marginally for 3D-FML specimens with 4 mm thickness, and detrimentally in the case of 3D-FML specimens with 10 mm thickness. As for 3D-FML specimens with 4 mm thickness, GNP-reinforced samples marginally outperformed MWCNT-reinforced samples, except in the case of interface reinforcement. Nevertheless, interface reinforcement remains important option from a fabrication and cost perspective owing to its lower material and labor requirements.

At this juncture, it is of interest to consider the morphology of NCP reinforced polymer phases, with the objective of exploring the effects that NCP addition had on the observed material responses. The examinations of samples using FESEM clearly confirmed the presence of dispersed NCP but also evidenced the existence of particle agglomerations and/or voids, as illustrated by the images shown in Figure 5.12. One of the reasons that NCP inclusion affects the vibration characteristics can be attributed to energy dissipation property of NCPs.

Table 5.4 Fundamental frequencies obtained experimentally (via GS and LDV) and analytically

Specimen ID	f_{GS} (Hz)	f_{LDV} (Hz)	$F_{Empirical.-SF}$ (Hz)
Al	460.66	460.00	463.75
3D-FML1	711.11	705.55	698.73
3D-FML2	716.44	716.66	714.47
3D-FML3	758.66	751.11	685.95
3D-FML4	787.77	785.55	714.27
3D-FML6	714.66	713.88	677.99
3D-FML7	677.66	676.66	671.71
3D-FML8	755.44	752.22	726.35
3D-FML9	1067.77	1065.55	984.63
3D-FML10	1050.00	1045.55	895.67
3D-FML11	933.77	946.66	783.64
3D-FML12	972.11	947.55	812.96
3D-FML14	923.77	922.22	802.45
3D-FML15	1046.44	1052.22	758.07
3D-FML16	1054.11	1056.66	1017.7
3D-FGF17	355.66	363.33	340.86
3D-FGF18	405.11	406.66	402.21
3D-FGF19	344.44	345.00	367.63
3D-FGF20	683.11	682.22	559
3D-FGF21	695.44	690.00	617.17
3D-FGF22	674.44	673.33	602.01

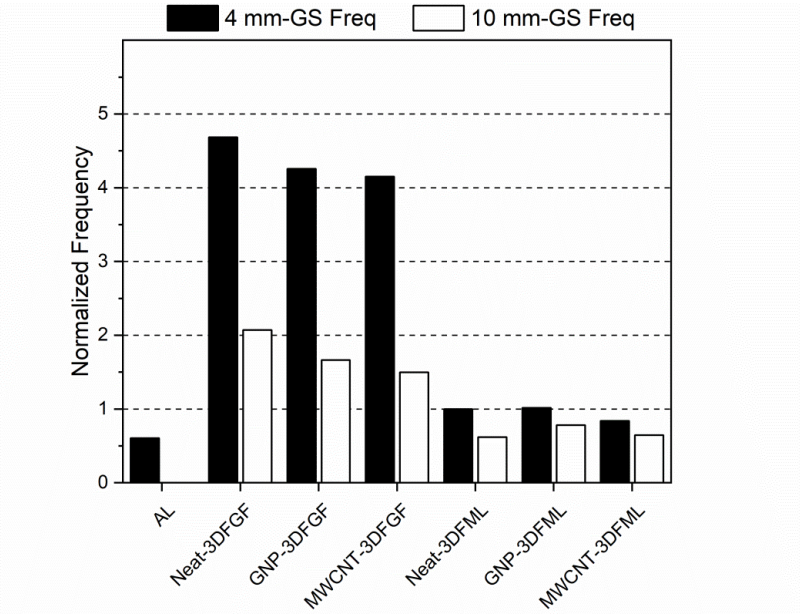

Figure 5.10 Influence of NCP reinforcement on fundamental frequencies of 3D-FGF and 3D-FML.

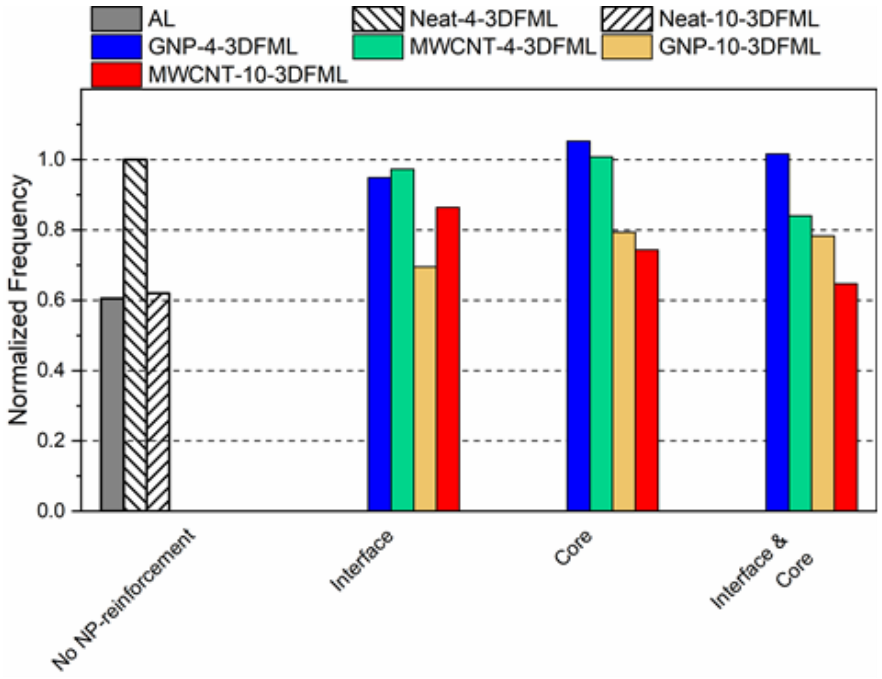

Figure 5.11 Influence of NCP reinforcement on the fundamental frequencies of 3D-FMLs as a function reinforced constituent(s).

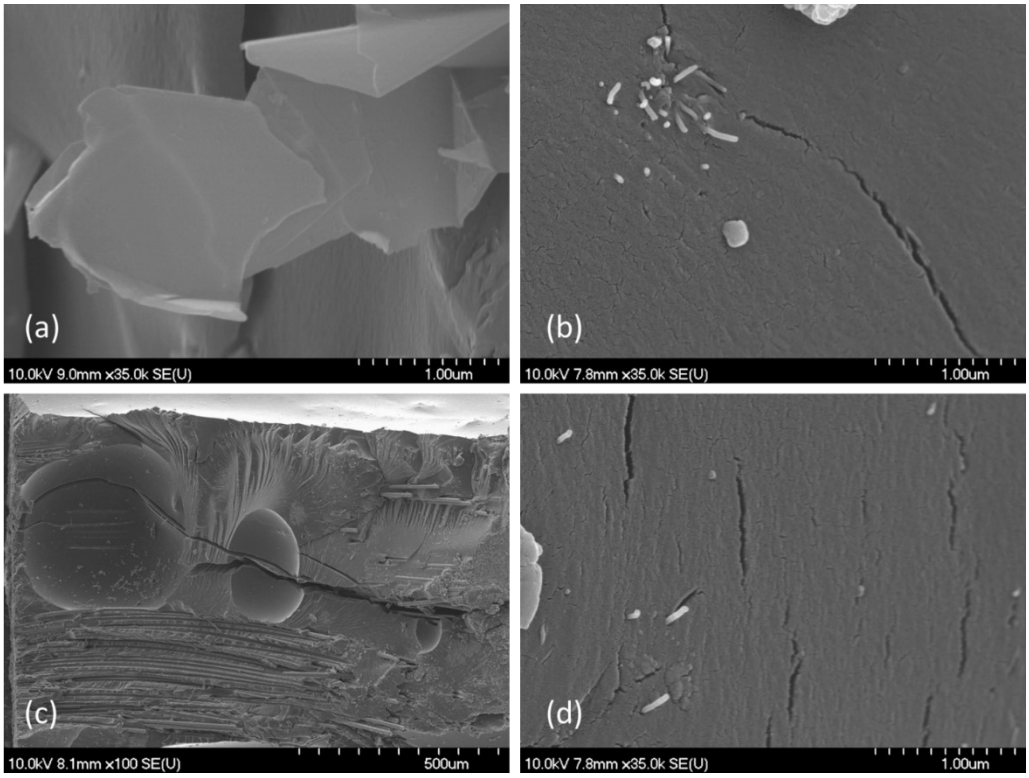

Figure 5.12 FESEM images of NCP reinforced 3D-FML resin phase: (a) GNP; (b) MWCNT agglomeration; (c) voids; and (d) well-dispersed MWCNT reinforcement.

5.9.3 Damping Ratio

A high damping ratio is a desirable property for sandwich panels, and as stated earlier, other researchers have reported exemplary damping characteristics for novel sandwich panel configurations, see e.g. [19,27]. Part of the present study's objectives are (a) evaluating the damping characteristic of 3D-FMLs and (b) assessing whether damping can be improved by the inclusion of NPs. Damping ratios, ξ, for all the tested material configurations are tabulated in Table 5.5, which shows that the calculated results based on GS and LDV measurements agree quite closely.

Table 5.5 Comparison of damping ratios obtained from GS and LDV measurements.

Specimen ID	ξ_{GS}	ξ_{LDV}
Al	4.79E-04	4.98E-04
3D-FML1	7.17E-04	7.38E-04
3D-FML2	3.42E-03	3.45E-03
3D-FML3	4.01E-03	3.82E-03
3D-FML4	2.42E-03	2.35E-03
3D-FML6	2.62E-03	2.55E-03
3D-FML7	1.68E-03	1.70E-03
3D-FML8	2.54E-03	2.57E-03
3D-FML9	2.15E-03	2.29E-03
3D-FML10	2.31E-03	2.32E-03
3D-FML11	2.84E-03	2.83E-03
3D-FML12	2.30E-03	2.35E-03
3D-FML14	1.92E-03	1.98E-03
3D-FML15	2.24E-03	2.26E-03
3D-FML16	1.86E-03	1.85E-03
3D-FGF17	5.78E-03	5.67E-03
3D-FGF18	6.57E-03	6.66E-03
3D-FGF19	6.89E-03	6.96E-03
3D-FGF20	4.14E-03	4.26E-03
3D-FGF21	4.29E-03	4.43E-03
3D-FGF22	4.89E-03	4.85E-03

Damping ratios were further analyzed as shown in Figure 5.13, which depicts data that were normalized with respect to the damping ratio of the 3D-FML with neat resin (non-reinforced) and 4 mm thickness. As discussed in the previous section, NCP reinforcement did not significantly affect the fundamental frequency of 3D-FML specimens. However, a significant influence of NCP reinforcement on damping ratios was observed in certain sandwich specimens. In general, damping ratios are much higher for 3D-FGFs than for 3D-FMLs, which can be attributed to an inherently lower damping capacity in metal-faced sandwich specimens. NCP modified resins affect the damping characteristics of GNP-reinforced 3D-FGFs but no clear trend can be ascertained as shown in Figure 5.13(a), that is, GNP seems to reduce the damping capacity of 3D-FGFs while MWCNT have only a minor influence on damping capacity of 3D-FGFs. Among the 3D-FMLs, GNP-reinforcement yields remarkable results for the 4 mm panels as shown in Figure 5.13(b). When reinforcing the interface with GNP a notable increase in damping ratio by 234 % was ascertained. Improvements were even higher when the resin phase in both the interface and core was modified with GNP. However, from a fabrication and cost perspective, the additional increase in damping ratio afforded by the NCP modification of the 3D-FML core must be weighed against the significant effort required for processing a NCP modified resin and applying it to the core. Conversely, the use of a modified resin for bonding at the 3D-FML interface is rather straightforward proposition.

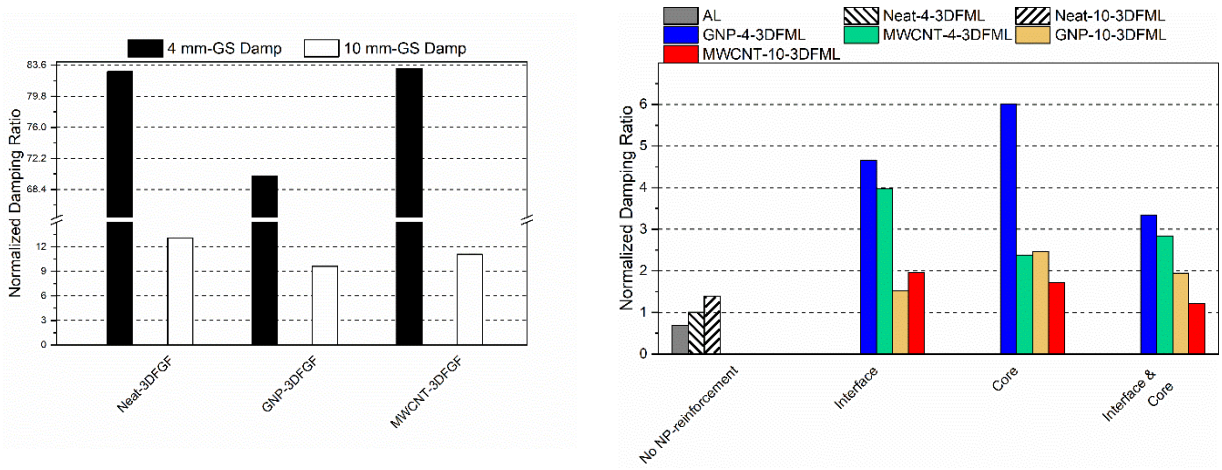

Figure 5.13 Influence of NC-reinforcement on the damping ratio of (a) 3D-FGF and (b) 3D-FML hybrid materials

5.9.4 Finite Element Results

The fundamental frequencies obtained through finite element analyses using the LS-DYNA software were compared to the experimental and empirical results. As shown in Figure 5.14, the FEM results are in agreement with ones obtained experimentally and using the developed empirical model.

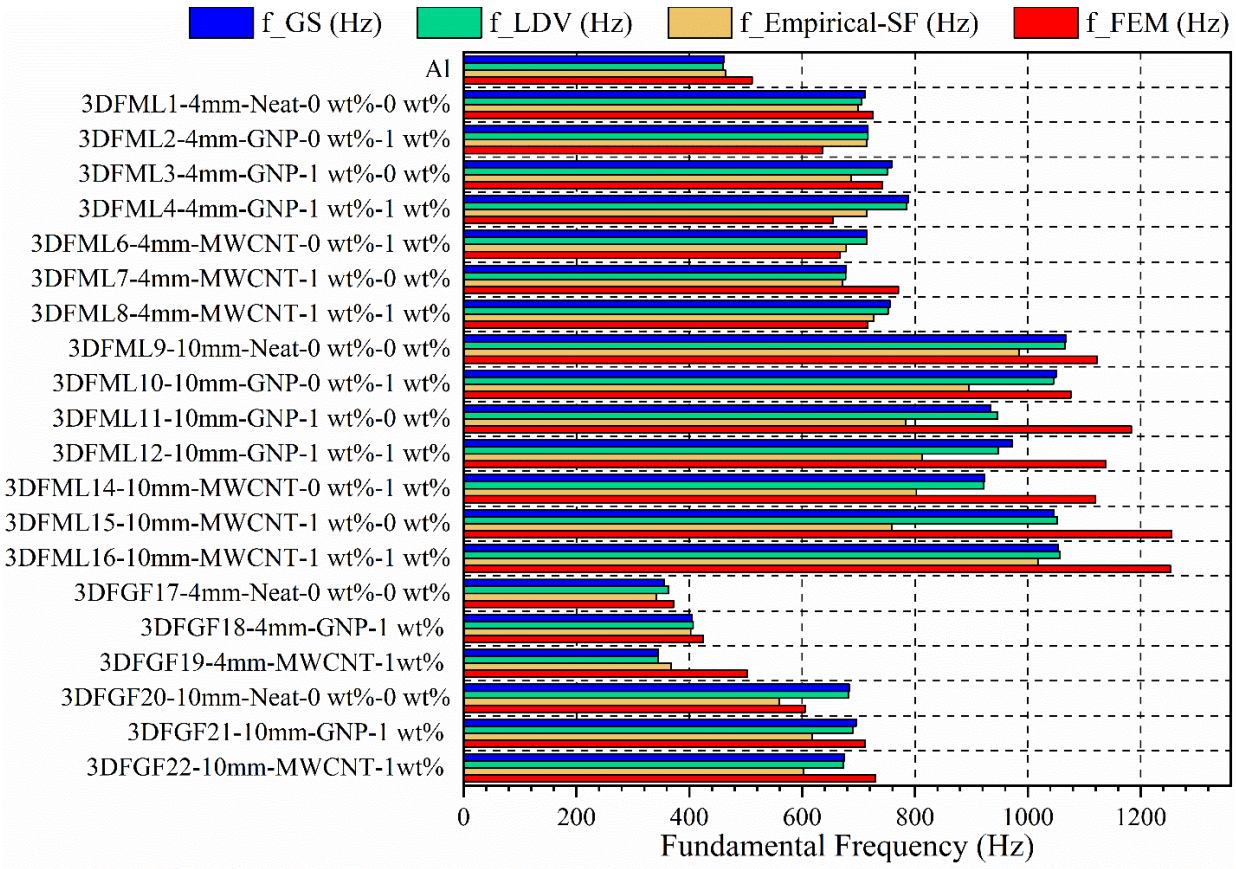

Figure 5.14 Fundamental frequencies obtained through finite element analyses using LS-DYNA commercial software versus experimental and empirical measurements

5.10 Conclusions

In this study, the vibration characteristics of 3D-FGF and 3D-FMLs were experimentally investigated. In addition, the effects of modifying the resin phase with GNP and MWCNT in the 3D-FML and at the interface in 3D-FMLs were explored. It was observed that the employed measurement systems, i.e., a GrindoSonic and a laser-Doppler vibrometer device, produced repeatable results that were in good agreement. The results of finite element analyses were in good agreement with the experiment and theoretical results. The experiments revealed that the inclusion of nanoparticles did not have an appreciable influence on increasing the fundamental frequencies of the hybrid material systems. However, nanofiller addition greatly augmented the damping ratio

of certain sample types. In fact, a 1 wt% inclusion of GNP in the interface of 4 mm thick 3D-FMLs led to a significant gain of 234% in the damping ratio of the hybrid system. It was also observed that in all cases, normalized fundamental frequency and normalized damping ratio of 3D-FGFs were higher than for 3D-FMLs. Moreover, specimens with 4 mm core thickness exhibited higher fundamental frequency and normalized damping ratio compared to specimens with 10 mm core thickness. It should be noted that the substantial gain in damping offered by nanoparticle reinforced 3D fabrics must be considered in light of their much lower bending rigidity compared 3D-FMLs (being approximately 10 times lower), which limits utilizing 3D-FGF for many structural applications. In light of the findings made in this study, the 3D-FML with 4 mm core thickness and 1 wt% GNP modified resin for bonding at the metal-interface proves to be an attractive material system that offers superior performance and cost-effectiveness among the system considered in this study.

Chapter 6

Vibration Characteristics of Thermally Cycled Graphene Nanoplatelet (GNP) Reinforced 3D-Fiber Metal Laminates (3D-FML)

6.1 Publication Statement

This chapter has been presented and published in the proceedings of the 37th Annual Technical Conference of Canadian Machinery Vibration Association by B. Soltannia as the 1st author. The title is "Vibration Characteristics of Thermally Cycled Graphene Nanoplatelet (GNP) Reinforced 3D-Fiber Metal Laminates (3D-FML)". The paper consists of 11 single-spaced single-column pages and received Student Award for Article and Presentation [5]. Sections '6.4. Results and Discussion', and '6.5. Conclusions' of this chapter have been updated.

6.2 Introduction

The superior strength- and stiffness-to-weight ratios of fiber-reinforced composite materials (FRPs) have increased their applications as load-bearing structural components in automobiles, trains, airplanes and even pipelines. Fiber-metal laminates (FMLs) also possess similar, and in some cases, even more positive attributes than FRP, thus making them even more attractive for incorporation in such potential applications. Therefore, several researchers have explored techniques that would ensure the safe and reliable performance of such materials when used under harsh environmental conditions [84,149,167–169,183,209]. A new rendition of FMLs, in the form of a new class of three-dimensional FMLs (3D-FMLs), exhibiting superior static and dynamic attributes and excellent crashworthiness was recently introduced by Asaee and Taheri [81]. Good damping properties are also an important feature of this class of materials, since unwanted and unharnessed vibrations in structures could result in undesirable noise and potential mechanical failure, or even worse, coupled with harsh environmental conditions, could cause the material to degrade and eventually result in the permanent failure of the system. De Cicco and Taheri [44], and Soltannia et al. [4], experimentally investigated the vibration characteristics of laminated and sandwich composite beams using non-destructive testing techniques (NDT). Other researchers have also examined the vibration characterizes of composites with innovative techniques. For instance, Cheraghi et al. [175] used the impulse excitation technique to establish material damping characteristics of polyvinyl chloride pipes by using piezoelectric sensors to record the vibration response. Hajikhani et al. [43] used an acoustic emission NDT technique to determine the presence and extent of defects.

The technical literature addressing the issue of thermal fatigue in conventional 2D-, and 3D-fiber metal laminates is quite scarce. In fact, only a few works have studied the influence of thermal

fatigue on honey-comb sandwich structures or FMLs. Addressing this issue is essential and inevitable for the aerospace, automotive, and other industrial sectors that use FML composites. The following is a summary of the notable studies.

Khosravani and Weinberg [210] studied loading and aging effects on honeycomb sandwich T-joints subject to thermal fatigue in the range of -35 °C up to 70 °C. They studied the failure behavior of the T-joints using fractographic analysis. They contrasted their results to 3D finite element analysis using cohesive zone modelling. They observed specimens to experience brittle failure. They also noticed that the application of 25 and 100 cycles degrade critical fracture stress (σ_c) of specimens by 2% and 40%, respectively. Their results show that the exposure time has greater influence compared to the exposed temperature. They also reported that specimens sustained 60% less load because of thermal fatigue, and the mode of failure changed in the thermally cycled specimens. Li et al. [211] studied the effect of thermal fatigue on 2D-FML, which had aluminum-lithium alloy as its metallic constituent. They observed no degradation or sign of failure after 1000 cycles. Notably, they found that the tensile and flexural strengths of their specimens increased after the application of thermal cycles due to a positive age-hardening response of the aluminum–lithium laminate. Khalili et al. [212] also studied the thermal effect on hybrid single-lap joints (SLJs) made of fiber metal laminate and stainless steel adherends both bonded and bolted. They investigated the influence of thermal cycles on the mechanical properties of hybrid SLJs by conducting a series of tensile tests. Their specimens were subjected to 40 °C to 100 °C and -40 °C to -100 °C cycles. Their results showed 52% and 50% strength recovery after heating and cryogenic cycles, respectively. Mosse et al. [213] showed that a glass fiber-reinforced thermoplastic fiber metal laminate (GFRT-FML) system had better formability (stamp forming) compared to aluminum, so long as the GFRT-FML was pre-annealed and rapidly transferred to

heated casting process tool (punch-die tool). Muller et al. [214] studied the effect of thermal cycling on interlaminar shear strength (ILSS) or bending rigidity (BR) of heater element-integrated glass-FML used in anti- or de-icing applications. Having heater elements embedded in FMLs gives the opportunity of thermally cycling (heating up) the specimens internally while cooling them down externally. They found that the ILSS of specimens subjected to a thermal gradient of 120 °C slightly increased by 6.9% after 8000 cycles of 60-90 sec., compared to the non-cycled specimens' response. In contrast, ILSS of internally heated and externally heated/cooled specimens was reduced by 7.8% after 12000 cycles. Jakubczak et al. [215] also studied thermal cycling effects on ILSS of 2D aluminum-carbon fiber laminates, by applying 1500 thermal cycles. As per their findings, thermal cycles did not affect the strength of their specimens. Da Costa et al. [216] studied the effect of thermal-shock cycles on the mechanical characteristics of aluminum-glass fiber-reinforced polymer FML composites, bonded using an epoxy adhesive tape. They exposed specimens to a 130 °C temperature gradient with a rapid transition and cycled the specimens to 1000 and 2000 cycles, stating that 2000 cycles would mimic a typical C check interval for a commercial aircraft maintenance program. They observed that thermal-shock cycles did not have a significant effect on the mechanical properties of FML. Majerski et al. [217] studied the hygrothermal effect on the mechanical properties of 2D FMLs and FRPs. They exposed specimens to 60 °C and 99% relative humidity (RH) to investigate the combined effect of elevated temperature and moisture. They identified that moisture absorption in the FMLs was significantly lower than in FRPs. They also found that the ILSS of FMLs and FRPs was degraded 9% to 11% and 27%, respectively;tensile strength decreased by 1% to 15% and 7% to 30%, respectively. Hu et al. [218] studied the effect of cyclic temperature on mechanical properties of adhesively bonded joints, and they reported a severe weakening effect due to a post-curing process. Through the

'response surface' method (a statistical-based technique of design of experiment), they determined that exposure to lower temperatures could cause greater and steeper degradation compared to degradation due to exposure to elevated temperatures. Brewis et al. [219] studied the effect of heating (16 °C to 85 °C) and moisture exposure for 2500 hours on mechanical properties of SLJs. They reported that moisture resulted in plasticization of the bonding adhesive and consequently degradation of mechanical properties of the SLJs.

The damping characteristics of 3D-FMLs may be improved using nanoparticles (NPs) as a passive technique for enhancing the dynamic damping properties of composite materials and structures. The advantages of including small amounts of NPs to improve the mechanical and electrical properties of resins used as the matrix in composite structures, as well as for adhesives, have also been investigated extensively by several researchers in the past [1,124,125,184,185]. Mohamed and Taheri [220,221] investigated the contribution of graphene nanoplatelets (GNP) in fracture toughness enhancement of a commonly used room-cured epoxy resin, and its performance and degradation, using double cantilever beam specimens subjected to various numbers of thermal cycles (to a maximum of 1000 heating/cooling cycles). They observed that in general, GNP improved the performance of the adhesive. They observed that the adhesive performance degraded initially (up to 300-400 cycles), and then the response was improved after exposure to a higher number of cycles (up to nearly 600 cycles), after which the performance suffered upon increased numbers of thermal cycles.

In this work, an investigation was conducted to assess the damping characteristics of GNP-reinforced 3D-FMLs subjected to thermal fatigue. It is demonstrated that the inclusion of 1 wt% GNP within the interface layers of the hybrid system improved the fundamental frequency of the 3D-FML specimens marginally and their damping ratio quite significantly at room temperature.

However, when the specimens were subjected to thermal fatigue, the gain in the properties reverted back to the values observed for the non-reinforced FML. Similar to work presented in [222], a maximum number of cycles performed was 999.

6.3 Materials and Methods

6.3.1 Materials

A three-dimensional fiberglass fabric (3D-FGF) was obtained from China Beihai Fiberglass Co. (Jiujiang City, Jiangxi, China). Magnesium alloy sheets (AZ31B-H24; 0.5 mm thick) were acquired from MetalMart International (Commerce, CA, USA). As a benchmark for test comparison, 6061-T6 aluminum sheets with 4mm thickness were obtained from a local distributer. The hot-cure epoxy resin used to fabricate the 3D-FGF and the core part of the 3D-FMLs composed of two parts (bisphenol-A-based Araldite LY 1564 resin and Aradur 2954 (cycloaliphatic polyamine) hardener) was purchased from Huntsman Co. (West Point, GA, USA). A two-part cold-cure thermoset epoxy resin (the West System (WS) 105 resin, and 206 hardener (Bay City, MI, USA)) was used for bonding the magnesium sheets to the core. The NP filler to be dispersed into the epoxy resin was GNP with an average diameter of 25 μm, thickness of 6 nm, surface area of 100 m^2 /g, and more than 95% purity (XG Science Ltd., Lansing, MI).

6.3.2 Specimen Preparation

The different specimen categories are listed in Table 6.1 along with the abbreviations used to identify samples throughout this study. 3D-FGF sheets (plates) for the core part of 3D-FMLs were fabricated in situ using the hot-cure epoxy resin system, by a hand brushing technique. Each plate was then cured in an oven at 60 °C for 2 hours and at 120°C for 8 hours. At least five beam specimens with dimensions of 200 mm × 20 mm × 4 mm (length × width × thickness) were cut from each plate prepared to study the effect of thermal fatigue (6 categories × 5 specimens = 30

specimens, as shown in Figure 6.1). In addition, three specimens for each control category were tested at room temperature, i.e., aluminum, Neat-4-3D-FML-0 Cycle and GNP-4-3D-FML-0 Cycle (3 categories × 3 specimens = 9 specimens). Hence, 39 samples were tested in total.

For the magnesium skins the bonding surfaces were roughened by grit-blasting, cleaned with an air gun, acetone washed and air-dried. The skins were then bonded to the core panels either using the neat cold-cure epoxy resin or a NP-modified version of this resin and kept under vacuum for at least 24 hours at room temperature to assure proper bonding. More details on the fabrication of 3D-FMLs can be found in De Cicco and Taheri [44] and Soltannia et al. [3].

For the NP dispersion, NPs were first distributed in the cold-cure resin system using a mechanical stirrer set at a speed of 2000 rpm for 10 minutes. Then, the NP-resin slurry was calendered using a three-roll mill homogenizer (Torrey Hills Technologies LLC, San Diego, CA, USA). The roller gap was adjusted at 30 μm using a filler gauge for a 1 wt% (by weight) concentration of GNP. In this study, the roller speed and calendering frequency were set constant at 174 rpm. To maximize the dispersion quality, calendering was conducted seven times. The curing agent was subsequently added to the slurry and mixed for 4–6 minutes using a stirrer set at a speed of 400 rpm. The mixture was then degassed under 28″ Hg vacuum for 2 to 3 minutes.

6.3.3 Cyclic Thermal Fatigue Test

As stated earlier, cyclic thermal fatigue is a common and critical loading scheme experienced by structures and materials. In service, materials often experience temperature fluctuation (warm-cold and vice versa). Table 6.2 summarizes the results of some studies that considered the influence of temperature fluctuations on the response of various composite materials and structural configurations.

Table 6.1 Specimen configurations and nomenclature.

Specimen ID *	Interface resin modification	NP filler loading
Al		
Neat-4-3D-FML-0 Cycle	Neat	0 wt%
GNP-4-3D-FML-0 Cycle	GNP	1 wt%
Neat-4-3D-FML-333 Cycles	Neat	0 wt%
GNP-4-3D-FML-333 Cycles	GNP	1 wt%
Neat-4-3D-FML-666 Cycles	Neat	0 wt%
GNP-4-3D-FML-666 Cycles	GNP	1 wt%
Neat-4-3D-FML-999 Cycles	Neat	0 wt%
GNP-4-3D-FML-999 Cycles	GNP	1 wt%

*"4" indicates the 3D-FML thickness of 4mm, and "0 Cycle", "333 Cycles", "666 Cycles" and "999 Cycles" refers to specimens without, after 333, 666 and 999 thermal cycles, respectively.

Table 6.2 Temperature range, type of specimens and results.

Ref. #	Type of specimen	Temp. range (°C)	# of Cycles	RH %	Results
[210]	T-joint honeycomb	-35 to +70	0, 25, 100	N/A	-2% and -40% reduction in strength at 25 and 100 cycles, respectively
[211]	FML	-65 to +135	0, 250, 500, 750, 1000	N/A	Qualitative study
[212]	FML	-100 to -40 & +40 to +100	0, 5, 10	50%	50% increase in tensile strength
[215]	FML	-50 to +80	1500	N/A	Qualitative study
[216]	FML	-50 to +80	1000 & 2000	100 %	12% reduction in tensile and ILSS
[217]	FML	+60	0	99%	1% - 15% reduction in tensile strength 9% - 11% reduction in ILSSS

In the present investigation, the specimens were exposed to −60 °C to +60 °C thermal cycles with 55 % relative humidity. This thermal fluctuation is often experienced by transport vehicles in a given year. Note that the exposure cycle was limited to +60 °C as the glass transition temperature (T_g) of the WS cold-cure epoxy resin used for bonding the magnesium sheets to 3D-FGF of 3D-FML is 65 °C. Cyclic thermal testing was conducted within an environmental chamber (Associated

Environmental Systems, Model ZBHD-205 benchtop humidity chamber, Acton, MA, USA). The temperature within the chamber was monitored continuously.

Each heating/cooling cycle included four stages, as illustrated in Figure 6.1(a). A typical thermal cycle consisted of a 30-minute hold period for each the high and low temperature level of +60 °C and -60 °C, respectively, with 30-minute intervals for ramping linearly between hold periods. For each test, the initial heating cycle started at room temperature.

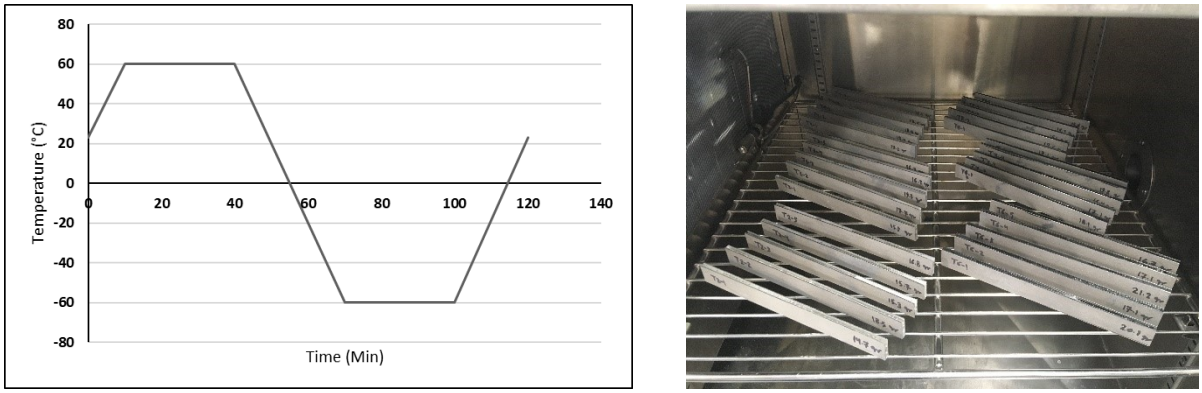

Figure 6.1 (a) Typical heating/cooling cycle, and (b) specimens in the environmental chamber.

In summary, five specimens were tested per specimen group in order to investigate the influence of thermal fatigue on vibration characteristics of 1 wt% GNP-reinforced 3D-FMLs at the interface (20 samples were tested only for the thermal fatigue study of 1 wt% GNP-reinforced 3D-FMLs at the interface). Overall, nine groups of specimens were tested, each being subjected to a different total number of cycles, as reported in Table 6.1.

6.3.4. Bending Rigidity Testing

The flexural bending rigidity (FBR) of the various specimens was evaluated employing three-point bending tests according to the pertinent ASTM standard [199]. A servo-hydraulic testing machine equipped with a digital electronic controller was employed for this purpose (2518-610, MTS, Eden Prairie, MN, USA). Figure 6.2 illustrates the experimental setup. Experimental data in terms of load and deflection was recorded using a PC.

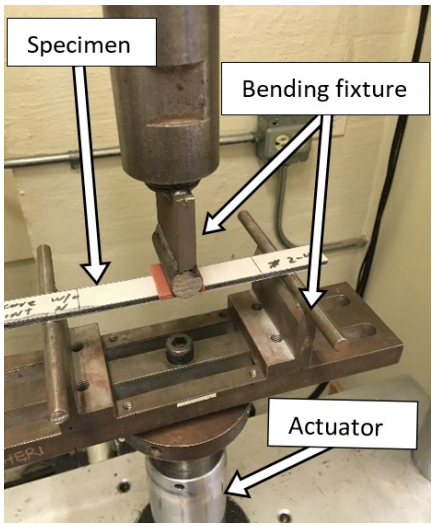

Figure 6.2 Three-point bending rigidity test setup.

6.3.5 Testing and Analysis Procedures

The experimental instruments used to acquire vibration signals are shown in Figure 6.3. Vibration data were recorded using a contact type device, i.e., a GrindoSonic (GS) instrument model MK5i (Leuven, Belgium). Two prismatic pieces of low-density foam were used as supports to resemble free-free boundary conditions. A lightweight hammer, consisting of a steel ball as the stiff tip attached to a thin wooden rod ('steel-wood hammer') was used to excite the specimens.

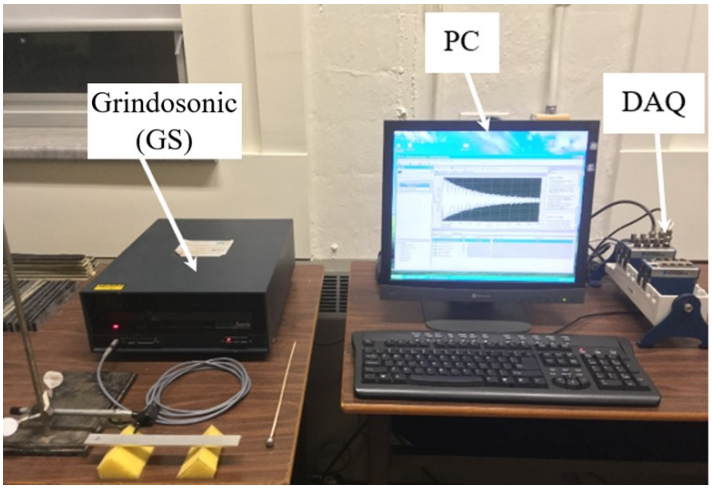

Figure 6.3 Experimental test setup for recording vibration signals of specimens with free-free boundary conditions using a Grindosonic device.

To extract the fundamental frequency (f_1) and damping ratio (ξ), one should capture the entire vibration oscillation spectrum. Hence, the GS was connected to a data-acquisition system, and the Signal Express software (National Instruments, Austin, TX, USA) was used to record the entire oscillation spectrum of each specimen at a 100 kHz sampling rate. The recorded data was then processed using LabVIEW (National Instruments).

6.3.6 Vibration Signal Extraction and Analysis

The frequency obtained from each complete vibration signal spectrum and more particularly, the power spectrum, was computed using the Spectral Measurements subroutine of LabVIEW. This subroutine takes the vibration signal from the GS and provides the amplitude of each frequency within the signal spectrum by subjecting the signal to a Fast Fourier Transform algorithm. Subsequently, the fundamental frequency is the frequency corresponding to the one with the largest amplitude, as shown in Figure 6.4(b).

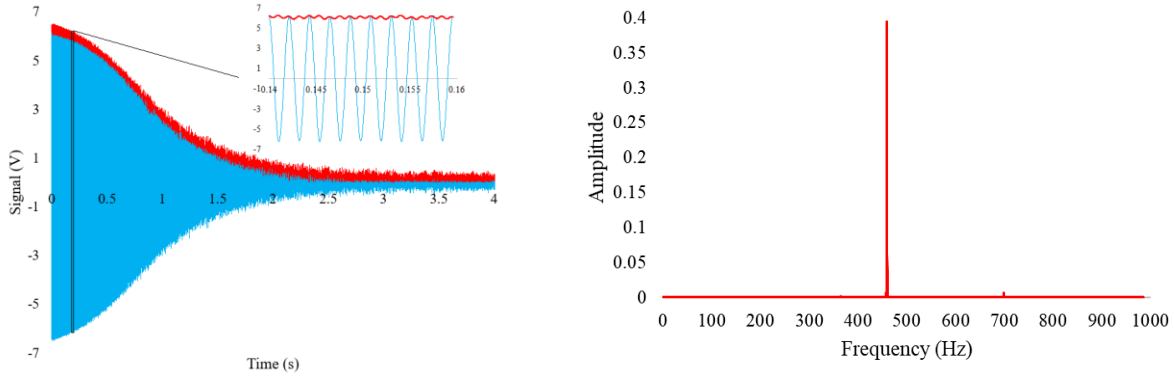

(a) (b)

Figure 6.4 (a) Typical vibration signal and its representative envelope; (b) power spectrum (aluminum specimen).

To calculate the damping coefficient, first, the signal was filtered in LabVIEW with a bandpass of ±30 Hz to mitigate noise. The envelope was then retrieved from the filtered signals using the Hilbert transform through the procedure described by Cheraghi et al. [175], as schematically illustrated in Figure 6.4(a), using the following mathematical operation:

$$H(t) = \frac{1}{\pi}\int_{-\infty}^{+\infty} u(\tau)\frac{\chi(\tau)}{t-\tau}d\tau \tag{6.1}$$

In practice, if the envelope contains a complex number, its real part includes the signal's amplitude and its imaginary part contains the Hilbert operator, as it has been explained by Yang and Song [204], as implemented in LabVIEW. In the end, the averaged damping coefficient was calculated based on the logarithm decrement method over 50 successive oscillatory points of the signal within the envelope. Using 50 successive oscillatory points ensured acceptable accuracy of the results while maintaining computational efficiency. As the damping coefficient of the aluminum specimens is relatively low compared to that of the 3D-FML specimens, a cut-off value of a 3-second time period was applied to aluminum specimen signals while a 0.1-second long signal duration was considered for 3D-FML specimens as the time period through which the decremental logarithm (and hence the damping coefficient) were calculated.

6.4 Results and Discussion

In the following, the results of the experiments and analyses are presented. It is worth mentioning that due to the nondestructive nature of vibration testing, at least nine vibration tests (modal experiments) were conducted per specimen and the reported results are the average of at least 45 tests and analyses for at least five specimens within each category of thermal fatigue study. Regarding bending rigidity tests, at least five specimens per category were tested for bending rigidity (at least 30 tests and analyses were conducted in total, for at least five specimens within

each category of thermal fatigue study). External noise was minimized during impulse excitation. Specimens were excited by tapping each specimen on the same location between the two supports, close to the center span of each specimen. Tapping on a different location could cause excitation of a different vibration mode and frequency.

Figure 6.5 shows experimental and theoretical flexural bending rigidity of thermally cycled and non-cycled specimens. The reported results indicate that the inclusion of 1 wt% GNP in the interface of the 3D-FMLs resulted in enhancement of their flexural bending rigidity regardless of thermal cycling number. However, thermal cycling in general degraded flexural bending rigidity of the specimens after 666 and 999 cycles in contrast to 333 cycles. These finding may be attributed to the state of crosslinking, as reported about the stiffness and ultimate tensile strength of the employed WS 105 epoxy resin system as well as its unidirectional fiber-reinforced composites by Mohamed et al. [222]. The authors claim that additional curing, i.e., crosslinking, of the resin occurred during the initial thermal cycling (to around 300 cycles), which may have counteracted degradation effects. Then, upon further thermal cycling, mechanical properties degradation occurred at a higher rate [222–225].

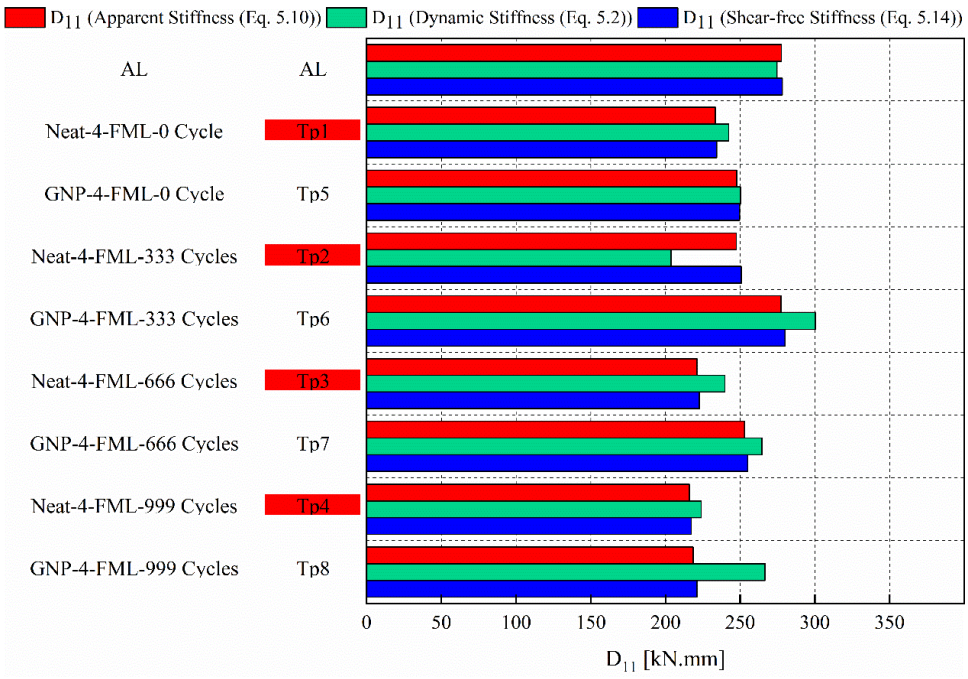

Figure 6.5 Experimental and theoretical flexural bending rigidity of thermally cycled specimens in comparison with non-cycled ones (Eq. 5.10, Eq. 5.2 and Eq. 5.14 have been explained in detail in Sections 5.7.4, 5.7.1 and 5.9.1, respectively)

Figure 6.6(a) shows all normalized fundamental frequency values of each category obtained experimentally through the use of the GS. Results were normalized by dividing them by their respective bending rigidity first, and then dividing the obtained values by the one obtained for the 3D-FML with neat resin. The reported results indicate that the inclusion of 1 wt% GNP in the interface of the 3D-FMLs undergone 333 and 666 thermal cycles resulted in lower normalized fundamental frequency, in contrast to the result of normalized fundamental frequency of the 3D-FMLs undergone 999 thermal cycles. Thermal cyclic loading also had a significant degrading influence on the normalized damping ratio of the specimens; however, NP-reinforced specimens exhibited higher damping compared to the non-NP-reinforced specimens without thermal cycling or long-run thermal cycling (666 and 999 cycles), see Figure 6.6(b).

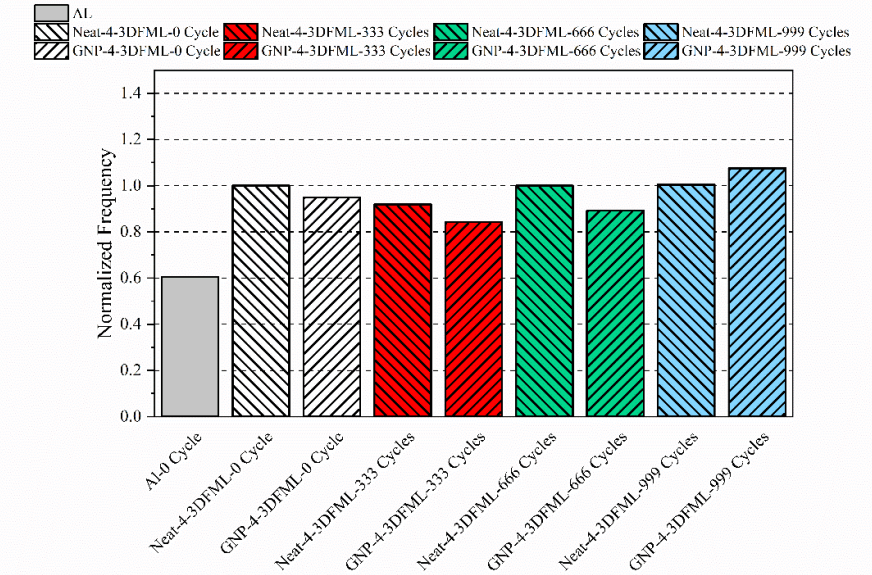

(a)

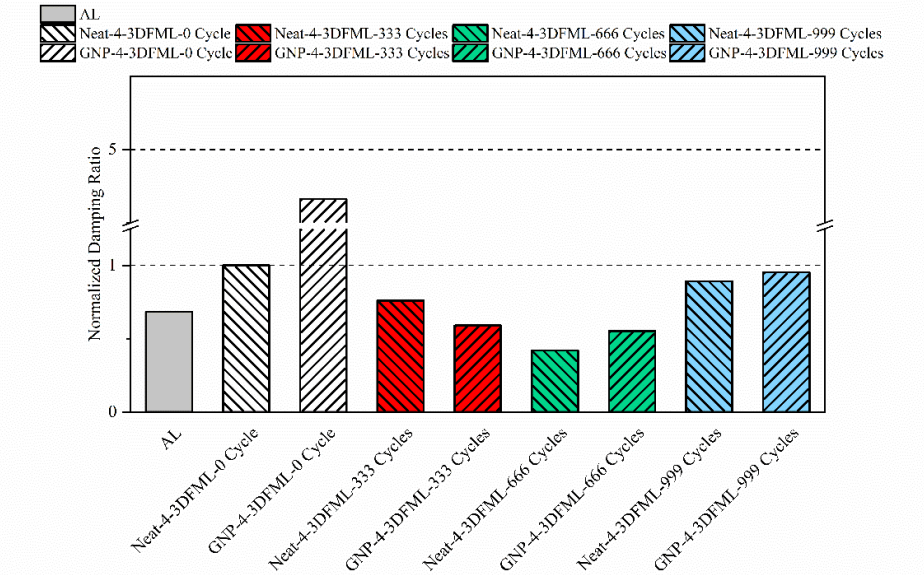

(b)

Figure 6.6 (a) Specimen averaged normalized fundamental frequencies, and (b) damping ratios.

6.5 Conclusions

The presented research explored the frequency response of 3D-fiber metal laminates undergoing cyclic thermal loading and the effect of nanoparticle modification of the interface layers of the hybrid system. In general, the inclusion of GNP in the interface of specimens enhanced their flexural bending rigidity compared to specimens fabricated using neat adhesive. However, thermal cycling degraded flexural bending rigidity of the specimens after 666 and 999 cycles in contrast to 333 cycles. This can be attributed to the resin's crosslinking capacity which first stiffens the resin then degrades it, as it has been extensively discussed in Mohamed and Taheri's work [222].

It can also be concluded that the inclusion of GNP in the interface of specimens decreased the frequency response, after 333 and 666 cycles in contrast to 999 cycles. The frequency response of specimens fabricated with neat adhesive remained almost unchanged. In general, thermal cycling lowered the damping ratio, however, NP-reinforced specimens exhibited higher damping compared to specimens made of pure resin except when 333 times thermally cycled.

Chapter 7

Summary and Conclusion

7.1 Summary

The thesis is built on the outcome of a series of experimental, statistical and numerical studies on the effect of nanoparticle (NP) incorporation in thermoset resin (adhesive) used in the fabrication of NP-reinforced polymers and their composites with application in single-lap joints (SLJs) as well as 3D Fiber Metal Laminates (3D-FMLs), and their structural performance, static and dynamic characteristics, and possible causes for their enhanced performance. SLJs were investigated in this research as they are considered a simpler yet somewhat similar geometry to 3D-FMLs.

7.2 Conclusions

Chapter 3 presented the results of parametric (systematic numerical) studies on the static and dynamic behavior of NP-reinforced thermoset resin (adhesive) and their composites with application in SLJs as well as 3D-FMLs. This study provided some indication of the effects of NP modification on structural performance, static and dynamic characteristics of NP-reinforced polymers and their composites with application in SLJs (as a simpler yet somewhat similar geometry to 3D-FMLs) and 3D-FMLs, and possible causes for their enhanced performance. The effect of load and time on neat and NP-modified thermoset polymer was also explored. This work served to obtain a deeper understanding of temporal aspects in the context of the thesis.

In this chapter, it was demonstrated that the combination of a strain rate dependent mechanical (SRDM) model (in this case, the Goldberg et al. model [104–106]) and a micromechanical model (in this case, the Halpin-Tsai model [111]) could predict the stress-strain response of neat and NP-reinforced epoxy resins with good accuracy. The predicted results also revealed that the response of the resin was improved when it was reinforced with the relatively inexpensive type of nano-carbon particles (i.e., Graphene Nano Platelets (GNP)), in comparison

to the more expensive carbon nanotubes (CNTs). It was also demonstrated that the increase in strain rate resulted in higher apparent strength of NP-reinforced resin. Comparatively, this increase was even more significant than the enhancement obtained by inclusion of the nano-carbon particles.

Further, comparison of the results obtained for the resin reinforced with 0.5 wt% of GNP and that reinforced with 0.5 wt% of CNF, subjected to the quasi-static strain rate, revealed that the inclusion of the GNP produced a greater average ultimate tensile strength and modulus of elasticity than inclusion of CNF could. Outcomes of a numerical study on vibration behavior of pure and NP-reinforced thermoset resin (adhesive) based on structural dynamics were also presented. It was shown that NP-reinforced thermoset resin (adhesive) has a higher damping ratio compared to the pure adhesive.

Finally, a transient response analysis of pure and GNP-reinforced polymer composite beams at room temperature indicated that the inclusion of GNP mitigates the settling-time response of the vibration and increases the damping ratio.

Chapter 4 contains statistical studies on the effect of NP-reinforcement on mechanical properties of the thermoset resin (adhesive), considering different variables, included, but not limited to, the feasible range of nanoparticles types, the filler content used in fabrication of NP-reinforced polymers (thermoset resin / adhesive) and their composites with application in SLJ and 3D-FMLs. Similar to Chapter 3, this work also serves to obtain a deeper understanding of temporal aspects in the context of SLJs as a simpler yet somewhat similar geometry to 3D-FMLs.

It was shown that improved results were obtained when the relatively inexpensive nano-carbon (i.e., GNP) was added to the resin. It was also observed that the addition of carbon

nanofibers (CNF) or multi-walled carbon nanotubes (MWCNTs) to a widely used epoxy resin improved the resin's mechanical properties, but not to the same degree as the GNP did.

It was demonstrated that the increase in loading rate resulted in a higher apparent strength of the SLJs. This enhancement was even more significant than the enhancement obtained by inclusion of GNP in the resin.

As expected, SLJs with graphite/epoxy adherends exhibited higher strength compared to those formed by glass/epoxy adherends. This increase is attributed to the fact that graphite/epoxy adherends are in general stiffer than glass/epoxy adherends, and consequently, the bending moments at the overlap region (hence the shear and peel stresses) are comparatively lower.

Moreover, this study demonstrated the influence of some parameters such as NP loading (wt%), adherend type, and strain rate on the mechanical response of SLJs, particularly on their averaged ultimate shear strength (AUSS). It was shown that the inclusion of GNP in the adhesive forming SLJs with carbon fiber-reinforced polymer (CFRP) adherends under the highest strain rate (HSR) produced the most enhancement in the load-bearing capacity. Moreover, the effective utility of the design of experiment (DOE) approach to study the augmentation of the response variables within a desired experimental investigation was also demonstrated. It should also be mentioned that SLJs would exhibit higher load-bearing capacity when subjected to a load that is applied at a high rate.

Chapter 5 was the first chapter dealing with rather complex hybrid system of material and geometry that constitutes a 3D-FML. This chapter is the core part of the thesis and provides the outcomes of systematic studies on processing, fabrication, and behavior of NP-reinforced polymers (thermoset resin (adhesive)) and their composites with application in 3D-FMLs. Their static and dynamic characteristics were investigated experimentally based on a non-destructive

testing (NDT) method and were compared with proposed empirical model. At the end the results of finite element analyses (FEA) were compared to experimental and empirical findings.

In this study, the vibration characteristics of 3D-FGF and 3D-FMLs were experimentally investigated. In addition, the effects of modifying the resin phase with GNP and MWCNT in the 3D-FML and at the interface in 3D-FMLs were explored. It was observed that the employed measurement systems, i.e., a Grindosonic (GS) and a laser-Doppler vibrometer (LDV) device, produced repeatable results that were in good agreement. The results of finite element analyses were in good agreement with the experiment and theoretical results. The experiments revealed that the inclusion of nanoparticles did not have an appreciable influence on increasing the fundamental frequencies of the hybrid material systems. However, nanofiller addition greatly augmented the damping ratio of certain sample types. In fact, a 1 wt% inclusion of GNP in the interface of 4 mm thick 3D-FMLs led to a significant gain of 234% in the damping ratio of the hybrid system. It was also observed that in all cases, normalized fundamental frequency and normalized damping ratio of 3D-FGFs were higher than for 3D-FMLs. Moreover, specimens with 4 mm core thickness exhibited a comparative higher fundamental frequency and normalized damping ratio compared to specimens with 10 mm core thickness. It should be noted that the substantial gain in damping offered by nanoparticle reinforced 3D fabrics must be considered in light of their much lower bending rigidity compared 3D-FMLs (being approximately 10 times lower), which limits utilizing 3D-FGF for many structural applications. In light of the findings made in this study, the 3D-FML with 4 mm core thickness and 1 wt% GNP modified resin for bonding at the metal-interface proves to be an attractive material system that offers the best performance and cost-effectiveness among the system considered in this study.

Chapter 6 is an extension of the work in Chapter 5 as it expands into environmental effects. The presented research study explored the frequency response of 3D-fiber metal laminates undergoing cyclic thermal loading and the effect of nanoparticle modification of the interface layers of the hybrid system. In general, the inclusion of GNP in the interface of specimens enhanced their flexural bending rigidity compared to specimens fabricated using neat adhesive. However, thermal cycling degraded flexural bending rigidity of the specimens after 666 and 999 cycles in contrast to 333 cycles, due to resin's crosslinking capacity which first stiffens the resin then degrades it [222].

It can also be concluded that the inclusion of GNP in the interface of specimens decreased the frequency response, after 333 and 666 cycles in contrast to 999 cycles. Frequency response of the specimens fabricated with neat adhesive almost remained unchanged. In general, thermal cycling lowers the damping ratio, however, NP-reinforced specimens exhibited higher damping compared to specimens made of pure resin except when 333 times thermally cycled.

In general, it can be concluded that although NP inclusion enhances overall stiffness of the composite material system in room temperature and under harsh environmental conditions, however, damping properties of such a material system are enhanced only in room temperature, and only in long-run harsh environmental condition.

7.3 Recommendations

Based on overall conclusion of this work, to enhance the performance of 3D-FML structures and specifically their stiffness-to-weight ratio and damping behavior, it is recommended to reinforce the interface section between the laminates of two face sheets using nano-reinforced polymer materials. On this basis, one may suggest to further explore the effect of functionally graded nano-reinforced polymer composites on the static and dynamic response of 3D-FML material systems.

The findings of this thesis provide the opportunity for further research and investigation on:

1. Experimental investigation of dynamic characteristics of neat and GNP-reinforced adhesive at room temperature, as well as after being thermally cycled, using non-destructive testing techniques (DMA and GrindoSonic tests) and validating the numerical results with the experimental results.
2. Damping modeling of neat and GNP-reinforced adhesives, as well as 3D-FMLs using LS-Dyna, and validating extracted damping ratios with the experimental values.
3. Partially/interleaved layer damping (P/ILD) studies by just applying epoxy resin to SMACWRAP® (SMAC® Group MontBlanc Tecnologies, Toulon, France) to embed it between skin and ply layers, instead of using 3M™-VHB™ (3M™, Ontario, Canada) adhesive transfer tape.
4. Fatigue behavior of 3D-FMLs under dynamic loading condition (forced vibration)
5. Static and dynamic characteristics of 3D Fiber Metal Laminate Tubes (3D-FMLTs)
6. Static and dynamic characteristic of 3D-FML joints (SLJs, DBJs, T-joints, etc.) at room temperature, as well as at elevated temperature or under cryogenic conditions.
7. Implementing/utilizing the same concept or other similar non-destructive techniques into defect/crack detection of tubular 3D-FML composite pipes.
8. Also, besides the potential of modifying the system by strategically reinforcing sections of the 3D-FML using nano-reinforced polymer materials as a passive method of damping, one may suggest and work on active methods, i.e., implementing piezoelectric functionality (sensors/actuators) for active damping purposes. Also, filling the empty columns separated by pillars using foam and/or viscoelastic materials may be a feasible means for performance improvements.

Bibliography

[1] B. Soltannia, I. Haji Gholami, S. Masajedian, P. Mertiny, D. Sameoto, F. Taheri, Parametric Study of Strain Rate Effects on Nanoparticle-Reinforced Polymer Composites, J. Nanomater. 2016 (2016) 1–9. doi:10.1155/2016/9841972.

[2] B. Soltannia, K. Duke, F. Taheri, P. Mertiny, Quantification of the Effects of Strain Rate and Nano-Reinforcement on the Performance of Adhesively Bonded Single-Lap Joints, Rev. Adhes. Adhes. 8 (2020) 19. doi:10.7569/RAA.2019.097305.

[3] B. Soltannia, P. Mertiny, F. Taheri, Static and dynamic characteristics of nano-reinforced 3D-fiber metal laminates using non-destructive techniques, J. Sandw. Struct. Mater. (2020). doi:10.1177/1099636220924585.

[4] B. Soltannia, P. Mertiny, F. Taheri, Vibration Characteristics of Multi-Wall Carbon Nanotubes (MWCNT) Reinforced 3D-Fiber Metal Laminates (3D-FML), in: 11th Can. Conf. Compos., Kelowna, 2019: pp. 1–8.

[5] Soltannia B, Mertiny P, Taheri F, VIBRATION CHARACTERISTICS OF THERMALLY CYCLED GRAPHENE NANOPLATELET (GNP) REINFORCED 3D-FIBER METAL LAMINATES (3D-FML), in: 37th Annu. Tech. Conf. Can. Mach. Vib. Assoc., Canadian Machinery Vibration Association, Halifax, 2019: pp. 1–11.

[6] E.F.F. Chladni, Die akustik, Breitkopf und Härtel, Leipzig, 1802.

[7] D. Ullmann, Life and work of E.F.F. Chladni, Eur. Phys. J. Spec. Top. 145 (2007) 25–32. doi:10.1140/epjst/e2007-00145-4.

[8] H.J. Stöckmann, Chladni meets Napoleon, Eur. Phys. J. Spec. Top. 145 (2007) 15–23. doi:10.1140/epjst/e2007-00144-5.

[9] S.O. Papkov, Vibrations of a rectangular orthotropic plate with free edges: Analysis and solution of an infinite system, Acoust. Phys. 61 (2015) 136–143. doi:10.1134/S106377101501008X.

[10] A.W. Leissa, Vibration of Plates, The National Aeronautics and Space Administration (NASA), Columbus, 1969.

[11] A.W. Leissa, The free vibration of rectangular plates, J. Sound Vib. 31 (1973) 257–293. doi:10.1016/S0022-460X(73)80371-2.

[12] Y.F. Xing, B. Liu, New exact solutions for free vibrations of thin orthotropic rectangular plates, Compos. Struct. 89 (2009) 567–574. doi:10.1016/j.compstruct.2008.11.010.

[13] S. Iguchi, Die Eigenschwingungen und Klangfiguren der vierseitig freien rechteckigen Platte, Ingenieur-Archiv. 21 (1953) 303–322. doi:10.1007/BF00535853.

[14] D.J. Gorman, Accurate Free Vibration Analysis of the Completely Free Orthotropic Rectangular Plate by the Method of Superposition, J. Sound Vib. 165 (1993) 409–420. doi:10.1006/jsvi.1993.1267.

[15] W. Ritz, Über eine neue Methode zur Lösung gewisser Variationsprobleme der mathematischen Physik, J. Für Die Reine Und Angew. Math. (1909). doi:10.1515/crll.1909.135.1.

[16] W. Weaver, S. Timoshenko, D. Young, Vibration problems in engineering, Fifth, John Wiley & Sons, Ltd, 1990.

[17] В.В. М Е Л Е Ш К О, С.О. П А П К О В, ИЗГИБНЫЕ КОЛЕБАНИЯ УПРУГИХ ПРЯМОУГОЛЬНЫХ ПЛАСТИН СО СВОБОДНЫМИ КРАЯМИ: ОТ ХЛАДНИ (1809) И РИТЦА (1909) ДО НАШИХ ДНЕЙ, Акустичний Вісник. 12 (2009) 34–51.

[18] П. Шакери Мобараке, В.Т. Гринченко, В.В. Попов, Б. Солтанниа, Г.М. Зражевский,

Современные методы численно-аналитического решения краевых задач для неканонических областей, Мат. Методи Та Фіз.-Мех. Поля. 60 (2017) 75–89.

[19] P.S. Mobarakeh, V.T. Grinchenko, Construction Method of Analytical Solutions to the Mathematical Physics Boundary Problems for Non-Canonical Domains, Reports Math. Phys. 75 (2015) 417–434. doi:10.1016/S0034-4877(15)30014-8.

[20] P. Shakeri Mobarakeh, V.T. Grinchenko, S. Iranpour Mobarakeh, B. Soltannia, Influence of acoustic screen on directional characteristics of cylindrical radiator, in: 5th Int. Conf. Acoust. Vib., Tehran, 2015.

[21] P. Shakeri Mobarakeh, V. Grinchenko, B. Soltannia, Directional characteristics of cylindrical radiators with an arc-shaped acoustic screen, J. Eng. Math. 103 (2017) 97–110. doi:10.1007/s10665-016-9863-9.

[22] P. Shakeri Mobarakeh, V.T. Grinchenko, H. Ahmadi, B. Soltannia, The amplitude-frequency characteristics of piezoceramic plates depending on the shape of the boundaries, in: 7th Int. Conf. Acoust. Vib., Tehran, 2017.

[23] P. Shakeri Mobarakeh, V.T. Grinchenko, B. Soltannia, Effect of Boundary Form Disturbances on the Frequency Response of Planar Vibrations of Piezoceramic Plates. Analytical Solution, Strength Mater. 50 (2018) 376–386. doi:10.1007/s11223-018-9981-x.

[24] P. Shakeri Mobarakeh, V.T. Grinchenko, B. Soltannia, V.A. Andrushchenko, Effect of Boundary Form Disturbances on the Frequency Response of Planar Vibrations of Piezoceramic Plates. Experimental Investigation, Strength Mater. 51 (2019) 214–220. http://link.springer.com/10.1007/s11223-018-9981-x (accessed March 17, 2020).

[25] P. Shakeri Mobarakeh, V.T. Grinchenko, B. Soltannia, Bending Vibrations of Bimorph Piezoceramic Plates of Noncanonical Shape, Int. Appl. Mech. 55 (2019) 321–331.

doi:10.1007/s10778-019-00958-y.

[26] P.S. Mobarakeh, V.T. Grinchenko, V. V. Popov, B. Soltannia, G.M. Zrazhevsky, Contemporary Methods for the Numerical-Analytic Solution of Boundary-Value Problems in Noncanonical Domains, J. Math. Sci. (United States). 247 (2020) 88–107. doi:10.1007/s10958-020-04791-4.

[27] M. Barnyak, B. Soltannia, Projection method of solving the problem of the natural vibrations of a clamped plate, Akust. Visn. 12 (2009) 11–18.

[28] М.Я. Б А Р Н Я К, Б. С О Л Т А Н Н И А, ПРОЕКЦИОННЫЙ МЕТОД РЕШЕНИЯ ЗАДАЧИ О СОБСТВЕННЫХ КОЛЕБАНИЯХ ЖЕСТКО ЗАЩЕМЛЕННОЙ ПЛАСТИНКИ, Акустичний Вісник. 12 (2009) 11–18. http://dspace.nbuv.gov.ua/xmlui/handle/123456789/87269 (accessed September 28, 2020).

[29] L.O.M.F.R.S. Rayleigh, XXIV. On the calculation of Chladni's figures for a square plate, London, Edinburgh, Dublin Philos. Mag. J. Sci. 22 (1911) 225–229. doi:10.1080/14786440808637121.

[30] M.M. Kaldas, S.M. Dickinson, Vibration and buckling calculations for rectangular plates subject to complicated in-plane stress distributions by using numerical integration in a rayleigh-ritz analysis, J. Sound Vib. 75 (1981) 151–162. doi:10.1016/0022-460X(81)90336-9.

[31] D.J. Dawe, T.J. Craig, The vibration and stability of symmetrically-laminated composite rectangular plates subjected to in-plane stresses, Compos. Struct. 5 (1986) 281–307. doi:10.1016/0263-8223(86)90038-3.

[32] X.X. Hu, T. Sakiyama, C.W. Lim, Y. Xiong, H. Matsuda, C. Morita, Vibration of angle-ply laminated plates with twist by Rayleigh-Ritz procedure, Comput. Methods Appl. Mech.

Eng. 193 (2004) 805–823.

[33] Z.X.X. Lei, L.W.W. Zhang, K.M.M. Liew, Free vibration analysis of laminated FG-CNT reinforced composite rectangular plates using the kp-Ritz method, Compos. Struct. 127 (2015) 245–259. doi:10.1016/j.compstruct.2015.03.019.

[34] C.-S. Chen, C.-P. Fung, R.-D. Chien, Nonlinear vibration of an initially stressed laminated plate according to a higher-order theory, Compos. Struct. 77 (2007) 521–532.

[35] T. Kant, K. Swaminathan, Analytical solutions for free vibration of laminated composite and sandwich plates based on a higher-order refined theory, Compos. Struct. 53 (2001) 73–85. doi:10.1016/S0263-8223(00)00180-X.

[36] T.M. Tu, L.N. Thach, T.H. Quoc, Finite element modeling for bending and vibration analysis of laminated and sandwich composite plates based on higher-order theory, Comput. Mater. Sci. 49 (2010) S390–S394. doi:10.1016/j.commatsci.2010.03.045.

[37] N.S. Bardell, J.M. Dunsdon, R.S. Langley, Free vibration analysis of thin coplanar rectangular plate assemblies - Part I: Theory, and initial results for specially orthotropic plates, Compos. Struct. 34 (1996) 129–143. doi:10.1016/0263-8223(95)00139-5.

[38] C.S. Tsay, J.N. Reddy, Bending, stability and free vibration of thin orthotropic plates by simplified mixed finite elements, J. Sound Vib. 59 (1978) 307–311. doi:10.1016/0022-460X(78)90511-4.

[39] H. Ahmadi Moghaddam, P. Mertiny, Stochastic finite element analysis framework for modelling thermal conductivity of particulate modified polymer composites, Results Phys. 11 (2018) 905–914. doi:10.1016/j.rinp.2018.10.045.

[40] H. Ahmadi Moghaddam, P. Mertiny, Stochastic Finite Element Analysis Framework for Modelling Mechanical Properties of Particulate Modified Polymer Composites, Materials

(Basel). 12 (2019) 2777. doi:10.3390/ma12172777.

[41] H. Ahmadi Moghaddam, P. Mertiny, Stochastic Finite Element Analysis Framework for Modelling Electrical Properties of Particle-Modified Polymer Composites, Nanomaterials. 10 (2020) 1754. doi:10.3390/nano10091754.

[42] G.P. Zou, M. Naghipour, F. Taheri, A nondestructive method for evaluating natural frequency of glued-laminated beams reinforced with GRP, Nondestruct. Test. Eval. 19 (2003) 53–65.

[43] M. Hajikhani, B. Soltannia, A. Refahi Oskouei, M. Ahmadi, Monitoring of delamination in composites by use of Acoustic Emission, in: 3rd Cond. Monit. Fault Diagnosis Conf., Tehran, 2009. https://scholar.google.ca/scholar?hl=en&as_sdt=0,5&cluster=16525731675275268808.

[44] D. Cicco, F. Taheri, Use of a Simple Non-Destructive Technique for Evaluation of the Elastic and Vibration Properties of Fiber-Reinforced and 3D Fiber-Metal Laminate Composites, Fibers. 6 (2018) 14. doi:10.3390/fib6010014.

[45] B. Soltannia, CHARACTERIZATION OF NANOCARBON-REINFORCED AND NEAT ADHESIVES IN BONDED SINGLE LAP JOINTS UNDER STATIC AND IMPACT LOADINGS, Dalhousie University, 2013.

[46] A. Kinloch, Adhesion and Adhesives, First, Springer Netherlands, 1987. doi:10.1007/978-94-015-7764-9_1.

[47] R.D. Adams, J. Comyn, W.C. Wake, Structural adhesive joints in engineering, Chapman & Hall, 1997. https://www.springer.com/gp/book/9780412709203 (accessed November 29, 2018).

[48] W. Possart, Experimental and theoretical description of the electrostatic component of

adhesion at polymer/metal contacts, Int. J. Adhes. Adhes. 8 (1988) 77–83. doi:10.1016/0143-7496(88)90027-9.

[49] B. Soltannia, D. Sameoto, Strong, reversible underwater adhesion via gecko-inspired hydrophobic fibers, ACS Appl. Mater. Interfaces. 6 (2014) 21995–22003. doi:10.1021/am5075375.

[50] B. Soltannia, D. Sameoto, Switchable Dry Adhesion Using Shape Memory Polymer, in: 38th Annu. Meet. Adhes. Soc., Curran Associates, Inc., Savannah, GA, 2015. http://toc.proceedings.com/27419webtoc.pdf (accessed September 25, 2020).

[51] D. Bareth, B. Soltannia, D. Sameoto, Evaluation of Space Qualified Dry Adhesives for Orbital Debris Capture, 203AD. http://nusil.com/product/scv1-2590_ultra-low- (accessed September 25, 2020).

[52] B. Soltannia, M.A. Islam, J.Y. Cho, F. Mohammadtabar, R. Wang, V.A. Piunova, Z. Almansoori, M. Rastgar, A.J. Myles, Y.H. La, M. Sadrzadeh, Thermally stable core-shell star-shaped block copolymers for antifouling enhancement of water purification membranes, J. Memb. Sci. 598 117686. doi:10.1016/j.memsci.2019.117686.

[53] B. Khorshidi, B. Soltannia, T. Thundat, M. Sadrzadeh, Synthesis of thin film composite polyamide membranes: Effect of monohydric and polyhydric alcohol additives in aqueous solution, J. Memb. Sci. 523 (2017) 336–345. doi:10.1016/j.memsci.2016.09.062.

[54] D. Bhattacharjee, H. Nazaripoor, B. Soltannia, M.F. Ismail, M. Sadrzadeh, An experimental and numerical study of droplet spreading and imbibition on microporous membranes, Colloids Surfaces A Physicochem. Eng. Asp. 615 (2021) 126191. doi:10.1016/j.colsurfa.2021.126191.

[55] D. Bhattacharjee, B. Soltannia, H. Nazaripoor, M. Sadrzadeh, Effect of surface roughness

on contact line dynamics of a thin droplet, in: 70th Annu. Meet. APS Div. Fluid Dyn. Bull. Am. Phys. Soc., The American Physical Society, Denver, Colorado, 2017: p. Q11.004. https://ui.adsabs.harvard.edu/abs/2017APS..DFDQ11004B/abstract (accessed September 26, 2020).

[56] R. Eslami-Farsani, H. Aghamohammadi, S.M.R. Khalili, H. Ebrahimnezhad-Khaljiri, H. Jalali, Recent trend in developing advanced fiber metal laminates reinforced with nanoparticles: A review study, J. Ind. Text. (2020). doi:10.1177/1528083720947106.

[57] J. Li, Y. Li, M. Huang, Y. Xiang, R. Bi, C. Tu, B. Wang, Surface Treatment for Improving Durability of Aluminum-Lithium Adhesive-Bonded Joints under Hot-Humid Exposure, Coatings. 9 (2019) 346. doi:10.3390/coatings9060346.

[58] S.G. Prolongo, A. Ureña, Effect of surface pre-treatment on the adhesive strength of epoxy-aluminium joints, Int. J. Adhes. Adhes. 29 (2009) 23–31. doi:10.1016/j.ijadhadh.2008.01.001.

[59] H. Aghamohammadi, S.N. Hosseini Abbandanak, R. Eslami-Farsani, S.M.H. Siadati, Effects of various aluminum surface treatments on the basalt fiber metal laminates interlaminar adhesion, Int. J. Adhes. Adhes. 84 (2018) 184–193. doi:10.1016/j.ijadhadh.2018.03.005.

[60] S.Y. Park, W.J. Choi, H.S. Choi, H. Kwon, Effects of surface pre-treatment and void content on GLARE laminate process characteristics, J. Mater. Process. Technol. 210 (2010) 1008–1016. doi:10.1016/j.jmatprotec.2010.01.017.

[61] A.F. Harris, A. Beevers, Effects of grit-blasting on surface properties for adhesion, Int. J. Adhes. Adhes. 19 (1999) 445–452. doi:10.1016/S0143-7496(98)00061-X.

[62] Y. Xu, H. Li, Y. Shen, S. Liu, W. Wang, J. Tao, Improvement of adhesion performance

between aluminum alloy sheet and epoxy based on anodizing technique, Int. J. Adhes. Adhes. 70 (2016) 74–80. doi:10.1016/j.ijadhadh.2016.05.007.

[63] M. Konstantakopoulou, G. Kotsikos, Effect of MWCNT filled epoxy adhesives on the quality of adhesively bonded joints, Plast. Rubber Compos. 45 (2016) 166–172. doi:10.1080/14658011.2016.1165788.

[64] A.A. Khurram, R. Hussain, H. Afzal, A. Akram, T. Subhanni, Carbon nanotubes for enhanced interface of fiber metal laminate, Int. J. Adhes. Adhes. 86 (2018) 29–34. doi:10.1016/j.ijadhadh.2018.08.008.

[65] J.S. Kim, D.H. Reneker, Mechanical properties of composites using ultrafine electrospun fibers, Polym. Compos. 20 (1999) 124–131. doi:10.1002/pc.10340.

[66] C. DeArmitt, R. Rothon, Particulate Fillers, Selection, and Use in Polymer Composites, in: 2017: pp. 3–27. doi:10.1007/978-3-319-28117-9_1.

[67] R. Sengupta, M. Bhattacharya, S. Bandyopadhyay, A.K. Bhowmick, A review on the mechanical and electrical properties of graphite and modified graphite reinforced polymer composites, Prog. Polym. Sci. 36 (2011) 638–670. doi:10.1016/j.progpolymsci.2010.11.003.

[68] S. Iijima, Helical microtubules of graphitic carbon, Nature. 354 (1991) 56–58. doi:10.1038/354056a0.

[69] S. Iijima, T. Ichihashi, Single-shell carbon nanotubes of 1-nm diameter, Nature. 363 (1993) 603–605. doi:10.1038/363603a0.

[70] S.C. Tjong, Structural and mechanical properties of polymer nanocomposites, Mater. Sci. Eng. R Reports. 53 (2006) 73–197. doi:10.1016/j.mser.2006.06.001.

[71] A.K.T. Lau, C. Gu, G.-H.H. Gao, H.Y. Ling, S.R. Reid, Stretching process of single- and

multi-walled carbon nanotubes for nanocomposite applications, Carbon N. Y. 42 (2004) 426–428. doi:10.1016/j.carbon.2003.10.040.

[72] B.G. Demczyk, Y.M. Wang, J. Cumings, M. Hetman, W. Han, A. Zettl, R.O. Ritchie, Direct mechanical measurement of the tensile strength and elastic modulus of multiwalled carbon nanotubes, Mater. Sci. Eng. A. 334 (2002) 173–178. doi:10.1016/S0921-5093(01)01807-X.

[73] D. Qian, E.C. Dickey, R. Andrews, T. Rantell, Load transfer and deformation mechanisms in carbon nanotube-polystyrene composites, Appl. Phys. Lett. 76 (2000) 2868–2870. doi:10.1063/1.126500.

[74] A. Liu, K.W. Wang, C.E. Bakis, Effect of functionalization of single-wall carbon nanotubes (SWNTs) on the damping characteristics of SWNT-based epoxy composites via multiscale analysis, Compos. Part A Appl. Sci. Manuf. 42 (2011) 1748–1755. doi:10.1016/j.compositesa.2011.07.030.

[75] A. Yasmin, I.M. Daniel, Mechanical and thermal properties of graphite platelet/epoxy composites, Polymer (Guildf). 45 (2004) 8211–8219. doi:10.1016/j.polymer.2004.09.054.

[76] B. Ahmadi-Moghadam, M. Sharafimasooleh, S. Shadlou, F. Taheri, Effect of functionalization of graphene nanoplatelets on the mechanical response of graphene/epoxy composites, Mater. Des. 66 (2015) 142–149. doi:10.1016/j.matdes.2014.10.047.

[77] A. Asundi, A.Y.N. Choi, Fiber Metal Laminates: An Advanced Material for Future Aircraft, J. Mater. Process. Technol. 63 (1997) 384–394.

[78] C.A.J.R. Vermeeren, An Historic Overview of the Development of Fibre Metal Laminates, Appl. Compos. Mater. 10 (2003) 189–205.

[79] A. Vlot, Glare history of the development of a new aircraft material, Kluwer Academic

Publishers, 2004.

[80] R. Marissen, Fatigue crack growth in ARALL: A hybrid aluminium-aramid composite material: Crack growth mechanisms and quantitative predictions of the crack growth rates, Delft University of Technology, 1988.

[81] Z. Asaee, F. Taheri, Experimental and numerical investigation into the influence of stacking sequence on the low-velocity impact response of new 3D FMLs, Compos. Struct. 140 (2016) 136–146. doi:10.1016/j.compstruct.2015.12.015.

[82] D. De Cicco, F. Taheri, Robust numerical approaches for simulating the buckling response of 3D fiber-metal laminates under axial impact – Validation with experimental results, J. Sandw. Struct. Mater. (2018) 1–30.

[83] M.R. Wisnom, Mechanisms to create high performance pseudo-ductile composites, in: IOP Conf. Ser. Mater. Sci. Eng., Institute of Physics Publishing, 2016.

[84] A.S. Sayyad, Y.M. Ghugal, On the free vibration analysis of laminated composite and sandwich plates: A review of recent literature with some numerical results, Compos. Struct. 129 (2015) 177–201. doi:10.1016/j.compstruct.2015.04.007.

[85] M. Ganapathi, D.P. Makhecha, Free vibration analysis of multi-layered composite laminates based on an accurate higher-order theory, Compos. Part BEngineering. 32 (2001) 535–543. doi:10.1016/S1359-8368(01)00028-2.

[86] M.K. Rao, Y.M. Desai, Analytical solutions for vibrations of laminated and sandwich plates using mixed theory, Compos. Struct. 63 (2004) 361–373. doi:10.1016/S0263-8223(03)00185-5.

[87] P.K. Parhi, S.K. Bhattacharyya, P.K. Sinha, Finite Element Dynamic Analysis of Laminated Composite Plates with Multiple Delaminations, J. Reinf. Plast. Compos. 19 (2000) 863–

882. doi:10.1177/073168440001901103.

[88] M.R. Loos, K. Schulte, Is It Worth the Effort to Reinforce Polymers With Carbon Nanotubes?, Macromol. Theory Simulations. 20 (2011) 350–362. doi:10.1002/mats.201100007.

[89] O. Breuer, U. Sundararaj, Big returns from small fibers: A review of polymer/carbon nanotube composites, Polym. Compos. 25 (2004) 630–645. doi:10.1002/pc.20058.

[90] G. Choudalakis, A.D. Gotsis, Permeability of polymer/clay nanocomposites: A review, Eur. Polym. J. 45 (2009) 967–984. doi:10.1016/j.eurpolymj.2009.01.027.

[91] J.J. Luo, I.M. Daniel, Characterization and modeling of mechanical behavior of polymer/clay nanocomposites, Compos. Sci. Technol. 63 (2003) 1607–1616. doi:10.1016/S0266-3538(03)00060-5.

[92] P.-G. Ren, D.-X. Yan, T. Chen, B.-Q. Zeng, Z.-M. Li, Improved properties of highly oriented graphene/polymer nanocomposites, J. Appl. Polym. Sci. 121 (2011) 3167–3174. doi:10.1002/app.33856.

[93] T.D. Fornes, D.R. Paul, Modeling properties of nylon 6/clay nanocomposites using composite theories, Polymer (Guildf). 44 (2003) 4993–5013. doi:10.1016/S0032-3861(03)00471-3.

[94] L. Datashvili, H. Baier, Membranes and Thin Shells for Space Reflectors, in: Earth & Sp. 2006, American Society of Civil Engineers, Reston, VA, 2006: pp. 1–8. doi:10.1061/40830(188)7.

[95] J.K. Lee, Prediction of thermal conductivity of composites with spherical fillers by successive embedding, Arch. Appl. Mech. 77 (2007) 453–460. doi:10.1007/s00419-006-0108-7.

[96] J. Rotrekl, L. Matějka, … A.Z.-E.P., undefined 2012, Epoxy/PCL nanocomposites: Effect of layered silicate on structure and behavior., Pdfs.Semanticscholar.Org. (n.d.). doi:10.3144/expresspolymlett.2012.103.

[97] M.A. Rafiee, J. Rafiee, Z. Wang, H. Song, Z.Z. Yu, N. Koratkar, Enhanced mechanical properties of nanocomposites at low graphene content, ACS Nano. 3 (2009) 3884–3890. doi:10.1021/nn9010472.

[98] R. Saito, G. Dresselhaus, M.S. Dresselhaus, Physical Properties of Carbon Nanotubes, London, 1998. doi:10.1142/p080.

[99] M. Alexandre, P. Dubois, Polymer-layered silicate nanocomposites: Preparation, properties and uses of a new class of materials, Mater. Sci. Eng. R Reports. 28 (2000) 1–63. doi:10.1016/S0927-796X(00)00012-7.

[100] V.K. Srivastava, P.J. Hogg, Moisture effects on the toughness, mode-I and mode-II of particles filled quasi-isotropic glass-fibre reinforced polyester resin composites, J. Mater. Sci. 33 (1998) 1129–1136. doi:10.1023/A:1004305104964.

[101] R.A. Schapery, Nonlinear Viscoelastic and Viscoplastic Constitutive Equations Based on Thermodynamics, Mech. Time-Dependent Mater. 1 (1997) 209–240. doi:10.1023/A:1009767812821.

[102] A. Plaseied, A. Fatemi, Deformation response and constitutive modeling of vinyl ester polymer including strain rate and temperature effects, J. Mater. Sci. 43 (2008) 1191–1199. doi:10.1007/s10853-007-2297-z.

[103] O.A. Hasan, M.C. Boyce, A constitutive model for the nonlinear viscoelastic viscoplastic behavior of glassy polymers, Polym. Eng. Sci. 35 (1995) 331–344. doi:10.1002/pen.760350407.

[104] R.K. Goldberg, D.C. Stouffer, Strain Rate Dependent Analysis of a Polymer Matrix Composite Utilizing a Micromechanics Approach, J. Compos. Mater. 36 (2002) 773–793. doi:10.1177/0021998302036007613.

[105] R.K. Goldberg, G.D. Roberts, A. Gilat, Implementation of an Associative Flow Rule Including Hydrostatic Stress Effects into the High Strain Rate Deformation Analysis of Polymer Matrix Composites, J. Aerosp. Eng. 18 (2005) 18–27. doi:10.1061/(ASCE)0893-1321(2005)18:1(18).

[106] A. Gilat, R.K. Goldberg, G.D. Roberts, Strain Rate Sensitivity of Epoxy Resin in Tensile and Shear Loading, J. Aerosp. Eng. 20 (2007) 75–89. doi:10.1061/(ASCE)0893-1321(2007)20:2(75).

[107] S.P. Bao, S.C. Tjong, Mechanical behaviors of polypropylene/carbon nanotube nanocomposites: The effects of loading rate and temperature, Mater. Sci. Eng. A. 485 (2008) 508–516. doi:10.1016/j.msea.2007.08.050.

[108] J. Ingram, Y. Zhou, S. Jeelani, T. Lacy, M.F. Horstemeyer, Effect of strain rate on tensile behavior of polypropylene and carbon nanofiber filled polypropylene, Mater. Sci. Eng. A. 489 (2008) 99–106. doi:10.1016/j.msea.2008.01.010.

[109] S. Peter, E. Woldesenbet, Nanoclay syntactic foam composites-High strain rate properties, Mater. Sci. Eng. A. 494 (2008) 179–187. doi:10.1016/j.msea.2008.04.009.

[110] M.M. Shokrieh, R. Mosalmani, M.J. Omidi, Strain rate dependent micromechanical modeling of reinforced polymers with carbon nanotubes, J. Compos. Mater. 48 (2014) 3381–3393. doi:10.1177/0021998313509864.

[111] J.C. Halpin, J.L. Kardos, The Halpin-Tsai equations: A review, Polym. Eng. Sci. 16 (1976) 344–352.

[112] P. Sharma, A. Gupta, A. Kumar Jain, V. Rastogi, Dynamic Modelling and validation of Continuous Beam with Free-Free Boundary Conditions, Int. Adv. Res. J. Sci. Eng. Technol. 4 (2017) 47–53. doi:10.17148/IARJSET.

[113] L.S. Al-Ansari, A.M.H. Al-Hajjar, H. Jawad, Calculating the natural frequency of cantilever tapered beam using classical Rayleigh, modified Rayleigh and finite element methods, Int. J. Eng. Technol. 7 (2018) 4866–4872. doi:10.14419/ijet.

[114] J.K. Sharma, Theoretical and experimental modal analysis of beam, in: Lect. Notes Electr. Eng., Springer Verlag, 2019: pp. 177–186. doi:10.1007/978-981-13-1642-5_16.

[115] M. Caresta, Vibrations of a Free-Free Beam, n.d.

[116] J.N. Reddy, On the dynamic behaviour of the Timoshenko beam finite elements, Sadhana - Acad. Proc. Eng. Sci. 24 (1999) 175–198. doi:10.1007/BF02745800.

[117] D. Younesian, A. Hosseinkhani, H. Askari, E. Esmailzadeh, Elastic and viscoelastic foundations: a review on linear and nonlinear vibration modeling and applications, Nonlinear Dyn. 97 (2019) 853–895. doi:10.1007/s11071-019-04977-9.

[118] H. Rajoria, N. Jalili, Passive vibration damping enhancement using carbon nanotube-epoxy reinforced composites, Compos. Sci. Technol. 65 (2005) 2079–2093. doi:10.1016/j.compscitech.2005.05.015.

[119] R. Shokri-Oojghaz, R. Moradi-Dastjerdi, H. Mohammadi, K. Behdinan, Stress distributions in nanocomposite sandwich cylinders reinforced by aggregated carbon nanotube, Polym. Compos. 40 (2019) E1918–E1927. doi:10.1002/pc.25206.

[120] M. Mirzaalian, F. Aghadavoudi, R. Moradi-Dastjerdi, Bending behavior of sandwich plates with aggregated CNT-reinforced face sheets, J. Solid Mech. 11 (2019) 26–38. doi:10.22034/JSM.2019.664214.

[121] R. Moradi-Dastjerdi, A. Radhi, K. Behdinan, Damped dynamic behavior of an advanced piezoelectric sandwich plate, Compos. Struct. 243 (2020) 112243. doi:10.1016/j.compstruct.2020.112243.

[122] M. Mohammadimehr, A.A. Monajemi, H. Afshari, Free and forced vibration analysis of viscoelastic damped FG-CNT reinforced micro composite beams, Microsyst. Technol. 26 (2020) 3085–3099. doi:10.1007/s00542-017-3682-4.

[123] M. Bouamama, A. Elmeiche, A. Elhennani, T. Kebir, Dynamic Stability Analysis of Functionally Graded Timoshenko Beams with Internal Viscous Damping Distribution, J. Eur. Des Systèmes Autom. 52 (2019) 341–346. doi:10.18280/jesa.520402.

[124] B. Soltannia, F. Taheri, Static, quasi-static and high loading rate effects on graphene nano-reinforced adhesively bonded single-lap joints, Int. J. Compos. Mater. 3 (2013) 181–190. doi:10.5923/j.cmaterials.20130306.07.

[125] B. Soltannia, F. Taheri, Influence of nano-reinforcement on the mechanical behavior of adhesively bonded single-lap joints subjected to static, quasi-static, and impact loading, J. Adhes. Sci. Technol. 29 (2015) 424–442. doi:10.1080/01694243.2014.991060.

[126] R.N. Rothon, Particulate-filled polymer composites, Longman Scientific & Technical, Harlow, Essex, England :, 1995. https://searchworks.stanford.edu/view/3067479.

[127] A.S.D. 10 on Mechanical, Standard Test Method for Tensile Properties of Plastics, (1998).

[128] ASTM D897 - 01 Standard Test Method for Tensile Properties of Adhesive Bonds, (n.d.).

[129] A.D.-03-A. D950–03, undefined 2011, Standard test method for impact strength of adhesive bonds, (n.d.).

[130] A. Tabiei, S.B. Aminjikarai, A strain-rate dependent micro-mechanical model with progressive post-failure behavior for predicting impact response of unidirectional

composite laminates, Compos. Struct. 88 (2009) 65–82. doi:10.1016/j.compstruct.2008.02.017.

[131] A. Tabiei, I. Ivanov, Micro-mechanical model with strain-rate dependency and damage for impact simulation of woven fabric composites, Mech. Adv. Mater. Struct. 14 (2007) 365–377. doi:10.1080/15376490601084624.

[132] R. Moradi-Dastjerdi, F. Aghadavoudi, Static analysis of functionally graded nanocomposite sandwich plates reinforced by defected CNT, Compos. Struct. 200 (2018) 839–848. doi:10.1016/j.compstruct.2018.05.122.

[133] A.J.M. Ferreira, N. Fantuzzi, MATLAB Codes for Finite Element Analysis, Springer International Publishing, Cham, 2020. doi:10.1007/978-3-030-47952-7.

[134] Z. Song, C. Su, Computation of Rayleigh Damping Coefficients for the Seismic Analysis of a Hydro-Powerhouse, Shock Vib. 2017 (2017). doi:10.1155/2017/2046345.

[135] D.R. Pant, A.C. Wijeyewickrema, M.A. ElGawady, Appropriate viscous damping for nonlinear time-history analysis of base-isolated reinforced concrete buildings, Earthq. Eng. Struct. Dyn. 42 (2013) 2321–2339. doi:10.1002/eqe.2328.

[136] M.H. Rahman, C. Gupta, Computation of Rayleigh damping coefficient of a rectangular submerged floating tunnel (SFT), SN Appl. Sci. 2 (2020) 1–10. doi:10.1007/s42452-020-2629-z.

[137] MATLAB Codes for Finite Element Analysis, Springer Netherlands, 2009. doi:10.1007/978-1-4020-9200-8.

[138] J. N. Reddy, An Introduction to Nonlinear Finite Element Analysis (2004, Oxford University Press, USA), (n.d.). doi:10.1093/acprof:oso/9780198525295.001.0001.

[139] P.D. J. N. Reddy, Introduction to the Finite Element Method, Fourth Edition, (2019).

[140] C. Cai, H. Zheng, K.C. Hung, Modeling of Material Damping Properties in ANSYS, n.d.

[141] material damping and modal analysis, (n.d.). https://studentcommunity.ansys.com/thread/material-damping-and-modal-analysis/ (accessed October 23, 2019).

[142] A. Pizzi, K.L. Mittal, Handbook of Adhesive Technology, 2020. https://www-taylorfrancis-com.login.ezproxy.library.ualberta.ca/books/9781498736473.

[143] E.M. Petrie, Handbook of adhesives and sealants, McGraw-Hill, 2007. https://www.accessengineeringlibrary.com/browse/handbook-of-adhesives-and-sealants-second-edition (accessed November 29, 2018).

[144] D.A. Dillard, Advances in structural adhesive bonding, 2010. doi:10.1533/9781845698058.

[145] L.F.M. da Silva, A. Öchsner, R.D. Adams, Handbook of Adhesion Technology, Cambridge University Press, Cambridge, 2010. doi:10.1088/1751-8113/44/8/085201.

[146] J.-M. Berthelot, Composite Materials: Mechanical Behavior and Structural Analysis, Springer, Netherlands, 1999.

[147] A.J. Kinloch, Adhesion and Adhesives, Springer Netherlands, Dordrecht, 1987. doi:10.1007/978-94-015-7764-9.

[148] M.D. Banea, L.F.M. da Silva, Adhesively bonded joints in composite materials: An overview, Proc. Inst. Mech. Eng. Part L J. Mater. Des. Appl. 223 (2009) 1–18. doi:10.1243/14644207JMDA219.

[149] M.W. Hyer, Stress Analysis of Fibre-Reinforced Composite Materials, DEStech Publication Inc., Lancaster, PA, 2009. https://www.destechpub.com/wp-content/uploads/2016/09/Stress-Analysis-Preview2.pdf (accessed November 29, 2018).

[150] Standard Test Method for Tensile Properties of Adhesive Bonds, (n.d.).

doi:10.1520/D0897-08R16.

[151] K.-T. Hsiao, J. Alms, S.G. Advani, Use of epoxy/multiwalled carbon nanotubes as adhesives to join graphite fibre reinforced polymer composites, Nanotechnology. 14 (2003) 791–793. doi:10.1088/0957-4484/14/7/316.

[152] J.A. Harris, R.D. Adams, An Assessment of the Impact Performance of Bonded Joints for Use in High Energy Absorbing Structures, Proc. Inst. Mech. Eng. Part C J. Mech. Eng. Sci. 199 (1985) 121–131. doi:10.1243/PIME_PROC_1985_199_102_02.

[153] C. Galliot, J. Rousseau, G. Verchery, Drop weight tensile impact testing of adhesively bonded carbon/epoxy laminate joints, Int. J. Adhes. Adhes. 35 (2012) 68–75. doi:10.1016/j.ijadhadh.2012.02.002.

[154] K.A. Brown, R. Brooks, N.A. Warrior, The static and high strain rate behaviour of a commingled E-glass/polypropylene woven fabric composite, Compos. Sci. Technol. 70 (2010) 272–283. doi:10.1016/j.compscitech.2009.10.018.

[155] D. Montgomery, Design and Analysis of Experiments, 2013.

[156] H. Rokni, A.S. Milani, R.J. Seethaler, M. Omidi, Quantification of Matrix and Reinforcement Effects on the Young's Modulus of Carbon Nanotube/Epoxy Composites using a Design of Experiments Approach, Int. J. Compos. Mater. 3 (2013) 45–57. doi:10.5923/s.cmaterials.201309.05.

[157] Standard Test Method for Lap Shear Adhesion for Fiber Reinforced Plastic (FRP) Bonding, (n.d.). doi:10.1520/D5868-01R14.

[158] Standard Terminology of Adhesives, (n.d.). doi:10.1520/D0907-15.

[159] Standard Guide for Use of Adhesive-Bonded Single Lap-Joint Specimen Test Results, (n.d.). doi:10.1520/D4896-01R16.

[160] Standard Test Method for Strength Properties of Adhesive Bonds in Shear by Compression Loading, (n.d.). doi:10.1520/D0905-08R13.

[161] Standard Test Method for Apparent Shear Strength of Single-Lap-Joint Adhesively Bonded Metal Specimens by Tension Loading (Metal-to-Metal), (n.d.). doi:10.1520/D1002-10.

[162] O. Burtovyy, V. Klep, T. Turel, Y. Gowayed, I. Luzinov, Polymeric membranes: Surface modification by "grafting to" method and fabrication of multilayered assemblies, in: ACS Symp. Ser., 2009: pp. 289–305. doi:10.1021/bk-2009-1016.ch022.

[163] S. Alimirzaei, M. Mohammadimehr, A. Tounsi, Nonlinear analysis of viscoelastic micro-composite beam with geometrical imperfection using FEM: MSGT electro-magneto-elastic bending, buckling and vibration solutions, Struct. Eng. Mech. 71 (2019) 485–502.

[164] S. Abrate, Impact on Composite Structures, Cambridge University Press, 1998.

[165] S. Abrate, Impact on laminated composites: Recent advances, Appl. Mech. Rev. 47 (1994) 517–544.

[166] M. Al-Haik, A.Y. Borujeni, M. Tehrani, Ballistic damage of hybrid composite materials, in: Adv. Fibrous Compos. Mater. Ballist. Prot., Elsevier Inc., 2016: pp. 121–143.

[167] I.M. Daniel, O. Ishai, Engineering mechanics of composite materials, 2nd ed., Oxford University Press, New York, 2006.

[168] P.K. Mallick, Fiber-Reinforced Composites: Materials, Manufacturing, and Design, 3rd ed., CRC Press, Boca Raton, FL, 2007. doi:10.1016/0010-4361(89)90651-4.

[169] J.N. Reddy, Mechanics of Laminated Composite Plates and Shells, CRC Press, Boca Raton, FL, 2004.

[170] D. Zenkert, An introduction to sandwich construction, Engineering Materials Advisory Services Ltd., Warrington, UK, 1995.

[171] A.K. Noor, Free vibrations of multilayered composite plates., AIAA J. 11 (1973) 1038–1039.

[172] V. Faires, Design of machine elements., 4th ed., Macmillan, New York, 1965. http://ualberta.worldcat.org/title/design-of-machine-elements/oclc/501288?referer=di&ht=edition (accessed December 4, 2018).

[173] G. Anlas, G. Göker, Vibration analysis of skew fibre-reinforced composite laminated plates, J. Sound Vib. 242 (2001) 265–276.

[174] C. Adam, Moderately large flexural vibrations of composite plates with thick layers, Int. J. Solids Struct. 40 (2003) 4153–4166.

[175] N. Cheraghi, M.J. Riley, F. Taheri, Application of Hilbert-Huang transform for evaluation of vibration characteristics of plastic pipes using piezoelectric sensors, Struct. Eng. Mech. 25 (2007) 653–674.

[176] M.J. Viens, J.J. Johnson, Determination of Elastic Moduli of Fiber Resin Composites Using an Impulse Excitation Technique, Greenbelt, MD, USA, 1996. https://ntrs.nasa.gov/archive/nasa/casi.ntrs.nasa.gov/19960015949.pdf.

[177] M. Braem, P. Lambrechts, V. Van Doren, G. Vanherle, The Impact of Composite Structure on Its Elastic Response, J. Dent. Res. 65 (1986) 648–653.

[178] J.-M. Berthelot, Damping Analysis of Orthotropic Composites with Interleaved Viscoelastic Layers: Modeling, J. Compos. Mater. 40 (2006) 1889–1909.

[179] E. Piollet, E.R. Fotsing, A. Ross, G. Michon, High damping and nonlinear vibration of sandwich beams with entangled cross-linked fibres as core material, Compos. Part B Eng. 168 (2019) 353–366. doi:10.1016/j.compositesb.2019.03.029.

[180] E.R. Fotsing, M. Sola, A. Ross, E. Ruiz, Dynamic characterization of viscoelastic materials

used in composite structures, J. Compos. Mater. 48 (2014) 3815–3825.

[181] E.R. Fotsing, C. Leclerc, M. Sola, A. Ross, E. Ruiz, Mechanical properties of composite sandwich structures with core or face sheet discontinuities, Compos. Part B Eng. 88 (2016) 229–239. doi:10.1016/j.compositesb.2015.10.037.

[182] J.J. Sargianis, H.I. Kim, E. Andres, J. Suhr, Sound and vibration damping characteristics in natural material based sandwich composites, Compos. Struct. 96 (2013) 538–544. doi:10.1016/j.compstruct.2012.09.006.

[183] F. Taheri, Applications of Nanoparticles in Adhesives: Current status, in: A. Pizzi, K.L. Mittal (Eds.), Handb. Adhes. Technol., 3rd ed., CRC Press, Boca Raton, FL, 2017: pp. 95–141.

[184] B. Soltannia, B. Ahmadi-Moghadam, F. Taheri, Influence of tensile impact and strain rate on the response of adhesively bonded single lap joints, in: Proc 19th Int. Conf. Compos. Mater., 2013: pp. 1410–1417.

[185] B. Ahmadi-Moghadam, B. Soltannia, F. Taheri, Interlaminar crack detection in graphene nanoplatelet/CFRP composites u sing electric resistance change, in: Proc 19th Int. Conf. Compos. Mater., 2013: pp. 3597–3607.

[186] C. DeValve, R. Pitchumani, Experimental investigation of the damping enhancement in fiber-reinforced composites with carbon nanotubes, Carbon N. Y. 63 (2013) 71–83. doi:10.1016/j.carbon.2013.06.041.

[187] S.U. Khan, C.Y. Li, N.A. Siddiqui, J.K. Kim, Vibration damping characteristics of carbon fiber-reinforced composites containing multi-walled carbon nanotubes, Compos. Sci. Technol. 71 (2011) 1486–1494. doi:10.1016/j.compscitech.2011.03.022.

[188] M. Balubaid, A. Tounsi, B. Dakhel, S.R. Mahmoud, Free vibration investigation of FG

nanoscale plate using nonlocal two variables integral refined plate theory, Comput. Concr. 24 (2019) 579–586.

[189] M. Kaddari, A. Kaci, A.A. Bousahla, A. Tounsi, F. Bourada, A. Tounsi, E.A.A. Bedia, M.A. Al-Osta, A study on the structural behaviour of functionally graded porous plates on elastic foundation using a new quasi-3D model: Bending and free vibration analysis, Comput. Concr. 25 (2020) 37–57.

[190] S. Boutaleb, K.H. Benrahou, A. Bakora, A. Algarni, A.A. Bousahla, A. Tounsi, A. Tounsi, S.R. Mahmoud, Dynamic analysis of nanosize FG rectangular plates based on simple nonlocal quasi 3D HSDT, Adv. Nano Res. 7 (2019) 189–206.

[191] C.C. Chamis, Analysis of the Three-Point-Bend Test for Materials With Unequal Tension and Compression Properties, Cleveland, Ohio, 1974. https://ntrs.nasa.gov/search.jsp?R=19740010415 (accessed April 8, 2019).

[192] ASTM E756 - Standard Test Method for Measuring Vibration-Damping Properties of Materials, Philadelphia, USA, 2017. http://www.ansi.org. (accessed April 8, 2019).

[193] ASTM D3039 - Standard Test Method for Tensile Properties of Polymer Matrix Composite Materials, Philadelphia, USA, 2017. www.astm.org, (accessed April 9, 2019).

[194] GrindoSonic: The Impulse Excitation Technique with Applications for Composites and Plastics, (n.d.). http://www.grindosonic.com/applications/composites_plastics.html.

[195] P. V. Straznicky, J.F. Laliberté, C. Poon, A. Fahr, Applications of fiber-metal laminates, Polym. Compos. 21 (2000) 558–567. doi:10.1002/pc.10211.

[196] R. Alderliesten, C. Rans, R. Benedictus, The applicability of magnesium based Fibre Metal Laminates in aerospace structures, Compos. Sci. Technol. 68 (2008) 2983–2993. doi:10.1016/j.compscitech.2008.06.017.

[197] P. Cortés, W.J. Cantwell, The fracture properties of a fibre-metal laminate based on magnesium alloy, Compos. Part B Eng. 37 (2005) 163–170. doi:10.1016/j.compositesb.2005.06.002.

[198] China Beihai Fiberglass Co. Ltd., (n.d.). http://www.fiberglassfiber.com/Item/Show.asp?m=5&d=345 (accessed January 16, 2020).

[199] ASTM D790-17, Standard Test Methods for Flexural Properties of Unreinforced and Reinforced Plastics and Electrical Insulating Materials, ASTM International, West Conshohocken, PA, 2017. www.astm.org.

[200] ASTM D7249/D7249M-20, Standard Test Method for Facesheet Properties of Sandwich Constructions by Long Beam Flexure, ASTM International, West Conshohocken, PA, 2020. www.astm.org,.

[201] J.W. Tedesco, W.G. McDougal, C. Allen Ross, Structural dynamics : theory and applications, Addison Wesley Longman, Menlo Park, CA, 1999.

[202] S.G. Kelly, Fundamentals Of Mechanical Vibration, 2nd ed., McGraw-Hill Education, New York, 1992.

[203] M. Naghipour, M. Mehrzadi, F. Taheri, G.P. Zou, Polynomial correction function for half-power bandwidth (HPB) method of damping of glulam beams reinforced with E-glass reinforced epoxy polymer (GRP), Can. J. Civ. Eng. 36 (2009) 241–252.

[204] X. Yang, S. Ji, L. Song, Signal Analysis and Processing Platform Based on LabVIEW, Sensors & Transducers. 172 (2014) 165–171.

[205] J.M. Gere, Mechanics of Materials, Sixth, Brooks/Cole –Thomson Learning, Belmont, CA, 2004.

[206] H. Hellal, M. Bourada, H. Hebali, F. Bourada, A. Tounsi, A.A. Bousahla, S.R. Mahmoud,

B. Abbes, B. Sidi, A. Abbes, Dynamic and stability analysis of functionally graded material sandwich plates in hygro-thermal environment using a simple higher shear deformation theory, (n.d.).

[207] A. Anis Bousahla, F. Bourada, S.R. Mahmoud, A. Tounsi, A. Algarni, E.A. Adda Bedia, A. Tounsi, Buckling and dynamic behavior of the simply supported CNT-RC beams using an integral-first shear deformation theory, Comput. Concr. 25 (2020) 155–166.

[208] A. Mahmoudi, S. Benyoucef, A. Tounsi, A. Benachour, E. Abbas, A. Bedia, S.R. Mahmoud, A refined quasi-3D shear deformation theory for thermo-mechanical behavior of functionally graded sandwich plates on elastic foundations, J. Sandw. Struct. Mater. 21 (2019) 1906–1929. doi:10.1177/1099636217727577.

[209] J.-M. Berthelot, Mechanics of composite materials and structures, 3rd ed., Vallouise, France, 2005.

[210] M.R. Khosravani, K. Weinberg, Characterization of sandwich composite T-joints under different ageing conditions, Compos. Struct. 197 (2018) 80–88. doi:10.1016/j.compstruct.2018.05.043.

[211] H. Li, Y. Hu, C. Liu, X. Zheng, H. Liu, J. Tao, The effect of thermal fatigue on the mechanical properties of the novel fiber metal laminates based on aluminum-lithium alloy, Compos. Part A Appl. Sci. Manuf. 84 (2016) 36–42. doi:10.1016/j.compositesa.2016.01.004.

[212] S.M.R. Khalili, M. Sharafi, R. Eslami-Farsani, A. Saeedi, Effect of thermal cycling on tensile properties of degraded FML to metal hybrid joints exposed to sea water, Int. J. Adhes. Adhes. 79 (2017) 95–101. doi:10.1016/j.ijadhadh.2017.09.011.

[213] L. Mosse, P. Compston, W.J. Cantwell, M. Cardew-Hall, S. Kalyanasundaram, The effect

of process temperature on the formability of polypropylene based fibre-metal laminates, Compos. Part A Appl. Sci. Manuf. 36 (2005) 1158–1166. doi:10.1016/j.compositesa.2005.01.009.

[214] B. Müller, M. Hagenbeek, J. Sinke, Thermal cycling of (heated) fibre metal laminates, Compos. Struct. 152 (2016) 106–116. doi:10.1016/j.compstruct.2016.05.020.

[215] P. Jakubczak, J. Bienias, B. Surowska, Interlaminar shear strength of fibre metal laminates after thermal cycles, Compos. Struct. 206 (2018) 876–887. doi:10.1016/j.compstruct.2018.09.001.

[216] A.A. da Costa, D.F.N.R. da Silva, D.N. Travessa, E.C. Botelho, The effect of thermal cycles on the mechanical properties of fiber-metal laminates, Mater. Des. 42 (2012) 434–440. doi:10.1016/j.matdes.2012.06.038.

[217] K. Majerski, B. Surowska, J. Bienias, The comparison of effects of hygrothermal conditioning on mechanical properties of fibre metal laminates and fibre reinforced polymers, Compos. Part B Eng. 142 (2018) 108–116. doi:10.1016/j.compositesb.2018.01.002.

[218] P. Hu, X. Han, W.D. Li, L. Li, Q. Shao, Research on the static strength performance of adhesive single lap joints subjected to extreme temperature environment for automotive industry, Int. J. Adhes. Adhes. 41 (2013) 119–126. doi:10.1016/j.ijadhadh.2012.10.010.

[219] D.M. Brewis, J. Comyn, R.J.A. Shalash, The effect of moisture and temperature on the properties of an epoxide-polyamide adhesive in relation to its performance in single lap joints, Int. J. Adhes. Adhes. 2 (1982) 215–222. doi:10.1016/0143-7496(82)90028-8.

[220] M. Mohamed, F. Taheri, Influence of graphene nanoplatelets (GNPs) on mode I fracture toughness of an epoxy adhesive under thermal fatigue, J. Adhes. Sci. Technol. 31 (2017)

2105–2123. doi:10.1080/01694243.2016.1264659.

[221] M. Mohamed, F. Taheri, Fracture response of double cantilever beam subject to thermal fatigue, J. Strain Anal. Eng. Des. 53 (2018) 504–516. doi:10.1177/0309324718791095.

[222] M. Mohamed, M. Johnson, F. Taheri, On the Thermal Fatigue of a Room-Cured Neat Epoxy and Its Composite, Open J. Compos. Mater. 09 (2019) 145–163. doi:10.4236/ojcm.2019.92007.

[223] B.G. Kumar, R.P. Singh, T. Nakamura, Degradation of Carbon Fiber-reinforced Epoxy Composites by Ultraviolet Radiation and Condensation, (n.d.). doi:10.1106/002199802028682.

[224] R. Hardis, J.L.P. Jessop, F.E. Peters, M.R. Kessler, Cure kinetics characterization and monitoring of an epoxy resin using DSC, Raman spectroscopy, and DEA, Compos. Part A Appl. Sci. Manuf. 49 (2013) 100–108. doi:10.1016/j.compositesa.2013.01.021.

[225] S. Cabral-Fonseca, J.R. Correia, M.P. Rodrigues, F.A. Branco, Artificial Accelerated Ageing of GFRP Pultruded Profiles Made of Polyester and Vinylester Resins: Characterisation of Physical-Chemical and Mechanical Damage, Strain. 48 (2012) 162–173. doi:10.1111/j.1475-1305.2011.00810.x.

Appendices

Appendix I

The second step of the R-K-4 using the results of the first step takes the following form:

$$d\varepsilon_{ij}^{I(step2)} = d\varepsilon_{ij}^{I}, \quad dZ^{(step2)} = dZ, \quad d\alpha^{(step2)} = d\alpha \tag{I-1}$$

$$\varepsilon_{ij}^{I} = \varepsilon_{ij}^{I(n)} + \frac{1}{2} d\varepsilon_{ij}^{I(step2)} \tag{I-2}$$

$$\{\sigma\} = [C_m]\left(\{\varepsilon\}^{n+1} - \{\varepsilon\}^{I}\right) \tag{I-3}$$

$$Z = Z^{m(n)} + \frac{1}{2} dZ^{(step2)} \tag{I-4}$$

$$\alpha = \alpha^{m(n)} + \frac{1}{2} d\alpha^{(step2)} \tag{I-5}$$

And the 3rd step can be obtained using the results of the 2nd step:

$$d\varepsilon_{ij}^{I(step3)} = d\varepsilon_{ij}^{I}, \quad dZ^{(step3)} = dZ, \quad d\alpha^{(step3)} = d\alpha \tag{I-6}$$

$$\varepsilon_{ij}^{I} = \varepsilon_{ij}^{I(n)} + \frac{1}{2} d\varepsilon_{ij}^{I(step3)} \tag{I-7}$$

$$\{\sigma\} = [C_m]\left(\{\varepsilon\}^{n+1} - \{\varepsilon\}^{I}\right) \tag{I-8}$$

$$Z = Z^{m(n)} + \frac{1}{2} dZ^{(step3)} \tag{I-9}$$

$$\alpha = \alpha^{m(n)} + \frac{1}{2} d\alpha^{(step3)} \tag{I-10}$$

Similar to pervious steps, results of the third step are used in the final step:

$$d\varepsilon_{ij}^{I(step4)} = d\varepsilon_{ij}^{I}, \quad dZ^{(step4)} = dZ, \quad d\alpha^{(step4)} = d\alpha \tag{I-11}$$

Then the magnitude of stress and inelastic strain in the next time step can be calculated throw the

final step of the Rang-Kutta method as follow:

$$\varepsilon_{ij}^{I(n+1)} = \varepsilon_{ij}^{I(n)} + \frac{1}{6} d\varepsilon_{ij}^{I(step1)} + \frac{1}{3} d\varepsilon_{ij}^{I(step2)} + \frac{1}{3} d\varepsilon_{ij}^{I(step3)} + \frac{1}{6} d\varepsilon_{ij}^{I(step4)} \tag{I-12}$$

$$\{\sigma\}^{m(n+1)} = [C_m]\left(\{\varepsilon\}^{n+1} - \{\varepsilon\}^{I(n+1)}\right) \tag{I-13}$$

$$Z^{m(n+1)} = Z^{m(n)} + \frac{1}{6} dZ^{(step1)} + \frac{1}{3} dZ^{(step2)} + \frac{1}{3} dZ^{(step3)} + \frac{1}{6} dZ^{(step4)} \tag{I-14}$$

$$\alpha^{m(n+1)} = \alpha^{m(n)} + \frac{1}{6} d\alpha^{(step1)} + \frac{1}{3} d\alpha^{(step2)} + \frac{1}{3} d\alpha^{(step3)} + \frac{1}{6} d\alpha^{(step4)} \tag{I-15}$$

Consequently, based on abovementioned equations the tensile stress-strain curve of the neat polymer under an arbitrary strain rate can be obtained.

Appendix II

Developed MATLAB codes used to calculate strain-rate and nano-reinforcement effects on polymer composites:

```
%=========================%Main-Strain Rate%==============================%
clc
clear
sample_loader;

%change i for different rates
for i=1:1


%========Specification of Experiment
SW                          %the material specification
str_rate= 1e-3*10^i;        %strain rate
dt=0.01/(10^i);
max_str=0.03;               %the max strain rate



N=round((max_str/str_rate)/dt);
%_________define the matrixes___
STR_I(1:N,1:6)=0;
STR(1:N,1:6)=0;
dSTR_I(1:N,1:6)=0;
dSTR(1:N,1:6)=0;
SIG(1:N,1:6)=0;
Z(1:N)=0;
a(1:N)=0;

%_____________________________________

%_________Initiation_________________
STR_I(1:N,1:6)=0;
dSTR(1,1)=str_rate;dSTR(1,2)=-str_rate*nou;dSTR(1,3)=-str_rate*nou;
SIG(1,1)= 1e2;
STR(1,1)=SIG(1,1)/E;STR(1,2)=-nou*SIG(1,1)/E;STR(1,3)=-nou*SIG(1,1)/E;
Z(1)=Z_0;
a(1)=a_0;

%________Stifness matrix__________=


C_mat=zeros(6);
C_mat(1,1)=1-nou;C_mat(2,2)=1-nou;C_mat(3,3)=1-nou;
C_mat(4,4)=(1-2*nou)/2;C_mat(5,5)=(1-2*nou)/2;C_mat(6,6)=(1-2*nou)/2;
C_mat(1,2)=nou;C_mat(1,3)=nou;
C_mat(2,1)=nou;C_mat(2,3)=nou;
C_mat(3,1)=nou;C_mat(3,2)=nou;
C_mat=C_mat*E/(1+nou)/(1-2*nou);
%_____________________________________=
```

```
STR(1,:)=transpose(inv(C_mat)*transpose(SIG(1,:)));
STR(1,:);
STR_I(1,:);
SIG(1,:);
Z(1);
a(1);
%gh=input('Initiation has been done');


%_________=Strain rate Matrix_____________________________
n=1;
while STR(1:n)<max_str
%while n<1000

%
%gh=input('Kutta Step 1')
[ sig_new,str_new,str_I_new,z_new,a_new,dz_new,da_new ] =...
                 Solver_1(
SIG(n,:),STR_I(n,:),STR(n,:),a(n),Z(n),D_0,Z_1,a_1,
n_u,q,C_mat,dSTR(n,:),dt,str_rate );

str_I_new_1=transpose(mat_col(str_I_new));
str_new_1=str_new;
sig_new_1=transpose(sig_new);
z_new_1=z_new;
a_new_1=a_new;
dz_new_1=dz_new;
da_new_1=da_new;


%gh=input('Kutta Step 2')
[ sig_new,str_new,str_I_new,z_new,a_new,dz_new,da_new ]=...

Solver_1(sig_new_1,str_I_new_1,str_new_1,a_new_1,z_new_1,D_0,Z_1,a_1,
n_u,q,C_mat,dSTR(n,:),dt,str_rate );


str_I_new_2=transpose(mat_col(str_I_new));
str_new_2=str_new;
sig_new_2=transpose(sig_new);
z_new_2=z_new;
a_new_2=a_new;
dz_new_2=dz_new;
da_new_2=da_new;


%gh=input('Kutta Step 3')
[ sig_new,str_new,str_I_new,z_new,a_new,dz_new,da_new ]=...

Solver_1(sig_new_2,str_I_new_2,str_new_2,a_new_2,z_new_2,D_0,Z_1,a_1,
n_u,q,C_mat,dSTR(n,:),dt,str_rate );


str_I_new_3=transpose(mat_col(str_I_new));
str_new_3=str_new;
sig_new_3=transpose(sig_new);
```

```
z_new_3=z_new;
a_new_3=a_new;
dz_new_3=dz_new;
da_new_3=da_new;

%gh=input('Kutta Step 4')
[ sig_new,str_new,str_I_new,z_new,a_new,dz_new,da_new ] =...

Solver_1(sig_new_3,str_I_new_3,str_new_3,a_new_3,z_new_3,D_0,Z_1,a_1,
n_u,q,C_mat,dSTR(n,:),dt,str_rate );


str_I_new_4=transpose(mat_col(str_I_new));
str_new_4=str_new;
sig_new_4=transpose(sig_new);
z_new_4=z_new;
a_new_4=a_new;
dz_new_4=dz_new;
da_new_4=da_new;


STR_I(n+1,:)=STR_I(n,:)+str_I_new_1/6+str_I_new_2/3+str_I_new_3/3+str_I_new_
4/6;
%-------------STR-----------------
STR(n+1,1)=str_rate*dt+STR(n,1);
Temp(1,1)=C_mat(2,2)*STR_I(n,2)+C_mat(2,3)*STR_I(n,3)-C_mat(2,1)*(STR(n,1)-
STR_I(n,1));
Temp(2,1)=C_mat(3,2)*STR_I(n,2)+C_mat(3,3)*STR_I(n,3)-C_mat(2,1)*(STR(n,1)-
STR_I(n,1));
A(1,1)=C_mat(2,2);
A(1,2)=C_mat(2,3);
A(2,1)=C_mat(3,2);
A(2,2)=C_mat(3,3);
Temp2=inv(A)*Temp;
STR(n+1,2)=Temp2(1,1);
STR(n+1,3)=Temp2(2,1);
STR(n+1,4)=0;
STR(n+1,5)=0;
STR(n+1,6)=0;
%-------------STR-----------------


SIG(n+1,:)=transpose(C_mat*transpose(STR(n+1,:)-STR_I(n+1,:)));


Z(n+1)=Z(n)+dz_new_1/6+dz_new_2/3+dz_new_3/3+dz_new_4/6;
a(n+1)=a(n)+da_new_1/6+da_new_2/3+da_new_3/3+da_new_4/6;


%================================
STR_I(n+1,:)
STR(n+1,:)
SIG(n+1,:)
Z(n+1)
a(n+1)

%================================
```

```
%gh=input('pause');
%}
%
%==========Solver===============
%this is descrit solver
[ sig_new,str_new,str_I_new,z_new,a_new ] =...
                  Solver_2(
SIG(n,:),STR_I(n,:),STR(n,:),a(n),Z(n),D_0,Z_1,a_1,
n_u,q,C_mat,dSTR(n,:),dt,str_rate );

STR_I(n+1,:)=transpose(mat_col(str_I_new));
STR(n+1,:)=str_new;
SIG(n+1,:)=transpose(sig_new);
Z(n+1)=z_new;
a(n+1)=a_new;
dSTR(n+1,1)=dSTR(n,1);
dSTR(n+1,2)=(STR(n+1,2)-STR(n,2))/dt;
dSTR(n+1,3)=(STR(n+1,3)-STR(n,3))/dt;
%}
%{
%}
n=n+1;
end
% CNF
% CNT
% GNP
Plot
end
Plot13
Plot14
Plot15
Plot16
```

```
%=========================%Function-Solver 1%==============================%
function [ sig_new,str_new,str_I_new,z_new,a_new,dz_new,da_new ] = Solver_1(
sig,str_I,str,a,z,D_0,Z_1,a_1,n_u,q,C_mat,dstr,dt,str_rate)
%UNTITLED5 Summary of this function goes here
%   Detailed explanation goes here
sig_mat=row_mat(sig);

S_mat=sig_mat-(sig_mat(1,1)+sig_mat(2,2)+sig_mat(3,3))/3*eye(3);
J_2=1/6*(sig_mat(1,1)-sig_mat(2,2))^2+1/6*(sig_mat(1,1)-sig_mat(3,3))^2+...
        1/6*(sig_mat(3,3)-sig_mat(2,2))^2+sig_mat(1,2)^2+sig_mat(2,3)^2+...
        sig_mat(3,1)^2;


sig_kk=sig_mat(1,1)+sig_mat(2,2)+sig_mat(3,3);
%==========================================================================
sig_e=sqrt(3*J_2)+sqrt(3)*a*sig_kk;
dSTR=(2*D_0*exp(-0.5*(z/sig_e)^(2*n_u))*(S_mat/2/sqrt(J_2)+a*eye(3)))*dt;
de_1=dSTR-1/3*trace(dSTR)*eye(3);
de_e_1=(2/3*(de_1(1,1)^2+de_1(1,2)^2+de_1(1,3)^2+...
            de_1(2,1)^2+de_1(2,2)^2+de_1(2,3)^2+...
            de_1(3,1)^2+de_1(3,2)^2+de_1(3,3)^2))^.5;

%============================Answers=======================================
dz_1=q*(Z_1-z)*de_e_1;
da_1=q*(a_1-a)*de_e_1;

str_I_new=row_mat(str_I)+0.5*dSTR;

str_new(1,1)=str_rate*dt+str(1,1);
Temp(1,1)=C_mat(2,2)*str_I_new(2,2)+C_mat(2,3)*str_I_new(3,3)-
C_mat(2,1)*(str_new(1,1)-str_I_new(1,1));
Temp(2,1)=C_mat(3,2)*str_I_new(2,2)+C_mat(3,3)*str_I_new(3,3)-
C_mat(2,1)*(str_new(1,1)-str_I_new(1,1));
A(1,1)=C_mat(2,2);
A(1,2)=C_mat(2,3);
A(2,1)=C_mat(3,2);
A(2,2)=C_mat(3,3);
Temp2=inv(A)*Temp;

str_new(1,2)=Temp2(1,1);
str_new(1,3)=Temp2(2,1);
str_new(1,4)=0;
str_new(1,5)=0;
str_new(1,6)=0;

sig_new=C_mat*(transpose(str_new)-mat_col(str_I_new));
z_new=z+0.5*dz_1;
a_new=a+0.5*da_1;
dz_new=dz_1;
da_new=da_1;

end
```

```
%=========================%Function-Solver 2%==============================%
function [ sig_new,str_new,str_I_new,z_new,a_new ] = Solver_2(
sig,str_I,str,a,z,D_0,Z_1,a_1,n_u,q,C_mat,dstr,dt,str_rate)
%UNTITLED5 Summary of this function goes here
%   Detailed explanation goes here
sig_mat=row_mat(sig);

S_mat=sig_mat-(sig_mat(1,1)+sig_mat(2,2)+sig_mat(3,3))/3*eye(3);
J_2=1/6*(sig_mat(1,1)-sig_mat(2,2))^2+1/6*(sig_mat(1,1)-sig_mat(3,3))^2+...
        1/6*(sig_mat(3,3)-sig_mat(2,2))^2+sig_mat(1,2)^2+sig_mat(2,3)^2+...
        sig_mat(3,1)^2;


sig_kk=sig_mat(1,1)+sig_mat(2,2)+sig_mat(3,3);
%=========================================================================
sig_e=sqrt(3*J_2)+sqrt(3)*a*sig_kk;
str_dot_I=(2*D_0*exp(-0.5*(z/sig_e)^(2*n_u))*(S_mat/2/sqrt(J_2)+a*eye(3)));

e_dot_ij=str_dot_I-1/3*trace(str_dot_I)*eye(3);

ee_dot_I=(2/3*(e_dot_ij(1,1)^2+e_dot_ij(1,2)^2+e_dot_ij(1,3)^2+...
            e_dot_ij(2,1)^2+e_dot_ij(2,2)^2+e_dot_ij(2,3)^2+...
            e_dot_ij(3,1)^2+e_dot_ij(3,2)^2+e_dot_ij(3,3)^2))^.5;

z_dot=q*(Z_1-z)*ee_dot_I;
a_dot=q*(a_1-a)*ee_dot_I ;
z_new=z+z_dot*dt;
a_new=a+a_dot*dt;

str_I_new=str_dot_I*dt+row_mat(str_I);

str_new(1,1)=str_rate*dt+str(1,1);
Temp(1,1)=C_mat(2,2)*str_I_new(2,2)+C_mat(2,3)*str_I_new(3,3)-
C_mat(2,1)*(str_new(1,1)-str_I_new(1,1));
Temp(2,1)=C_mat(3,2)*str_I_new(2,2)+C_mat(3,3)*str_I_new(3,3)-
C_mat(2,1)*(str_new(1,1)-str_I_new(1,1));
A(1,1)=C_mat(2,2);
A(1,2)=C_mat(2,3);
A(2,1)=C_mat(3,2);
A(2,2)=C_mat(3,3);
Temp2=inv(A)*Temp;
str_new(1,2)=Temp2(1,1);
str_new(1,3)=Temp2(2,1);
str_new(1,4)=0;
str_new(1,5)=0;
str_new(1,6)=0;

sig_new=C_mat*(transpose(str_new)-mat_col(str_I_new));

%============================Answers=======================================
%gh=input('pasue')
end
```

```
%=======%ML-526%=======%

material='ML-526';
nou=0.38;
E=3.00e9;
D_0=1e6;
n_u=0.83;
Z_0=396.09e6;
Z_1=800.82e6;
q=239.26;
a_0=0.568;
a_1=0.156;
```

```
%=======%PR-520%=======%

material='PR520';
nou=0.38;
E=3.54e9;
D_0=1e6;
n_u=0.93;
Z_0=396.09e6;
Z_1=753.82e6;
q=279.26;
a_0=0.568;
a_1=0.126;
```

```
%=======%WS-105%=======%

material='WS';
nou=0.30;
E=3.1e9;
D_0=5e6;
n_u=0.745;
Z_0=200e6;
Z_1=1130e6;
q=610;
a_0=0.202;
a_1=0.430;
```

```
%================================% CNF %================================%
d=4000e-9;
l=20000e-9
E_f=220e9;
si=0.0055;

E_m=diff(SIG(:,1))./diff(STR(:,1));

zeta=.3*2*l/d;
for i=1:n-1
eta(i)=(E_f/E_m(i,1)-1)/(E_f/E_m(i,1)+zeta);
E_c(i,1)=E_m(i,1)*(1+zeta*eta(i)*si)/(1-eta(i)*si);
end

sig_c(1,1)=SIG(1,1);
est_c(1,1)=STR(1,1);
for i=2:n-1

sig_c(i,1)=sig_c(i-1,1)+E_c(i)*(STR(i,1)-STR(i-1,1));
end

% for i=1:n-1
% eta(i)=(E_f/E_m(i,1)-d/4/t)/(E_f/E_m(i,1)+d/2/t);
%                             E_c(i,1)=E_m(i,1)*((3/8)*(1+2*l/d*eta(i)*si)/(1-
eta(i)*si)+(5/8)*((1+2*eta(i)*si)/(1-eta(i)*si)));
% end
% sig_c(1,1)=SIG(1,1);
% est_c(1,1)=STR(1,1);
% for i=2:n-1
%
% sig_c(i,1)=sig_c(i-1,1)+E_c(i)*(STR(i,1)-STR(i-1,1));
% end
```

```
%==================================% GNP %====================================%
l=500e-9;
t=0.34e-9;
E_f=250e9;
si=0.0055;

%  l=1e-6;
%  t=5e-9;
%  E_f=250e9;
%  si=0.011;

E_m=diff(SIG(:,1))./diff(STR(:,1));

zeta=15;%2*l/t;

for i=1:n-1
eta(i)=(E_f/E_m(i,1)-1)/(E_f/E_m(i,1)+zeta);
E_c(i,1)=E_m(i,1)*(1+zeta*eta(i)*si)/(1-eta(i)*si);
end

sig_c(1,1)=SIG(1,1);
est_c(1,1)=STR(1,1);
for i=2:n-1

sig_c(i,1)=sig_c(i-1,1)+E_c(i)*(STR(i,1)-STR(i-1,1));
end
```

```
%==================================% CNT %====================================%
d=20e-9;
l=20000e-9
E_f=1e12;
si=0.0055;
t=1.5e-9

E_m=diff(SIG(:,1))./diff(STR(:,1));

zeta=5%2*l/d;
for i=1:n-1
eta(i)=(E_f/E_m(i,1)-1)/(E_f/E_m(i,1)+zeta);
E_c(i,1)=E_m(i,1)*(1+zeta*eta(i)*si)/(1-eta(i)*si);
end

sig_c(1,1)=SIG(1,1);
est_c(1,1)=STR(1,1);
for i=2:n-1
sig_c(i,1)=sig_c(i-1,1)+E_c(i)*(STR(i,1)-STR(i-1,1));
end
% for i=1:n-1
% eta(i)=(E_f/E_m(i,1)-d/4/t)/(E_f/E_m(i,1)+d/2/t);
%                               E_c(i,1)=E_m(i,1)*((3/8)*(1+2*l/d*eta(i)*si)/(1-
eta(i)*si)+(5/8)*((1+2*eta(i)*si)/(1-eta(i)*si)));
% end
```

```
%============================%sample_loader%================================
%
%=============Sample_1=====================
A = csvread('Neat(0-0%)(1-5).csv');
sample1=A;
sample1(:,2)=A(:,2)*1.02
clear A;
%==========================================
%=================Sample_2=================
A = load('WS-(15)neat-No1.mat');
sample2=A.A;
%sample2(:,2)=sample2(:,2)
clear A;
%==========================================
%=================Sample_3=================
A = load('WS-(150)neat-No1.mat');
sample3=A.A;
%sample2(:,2)=sample2(:,2)
clear A;
%==========================================
%=================Sample_4=================
A = load('WS-(1500)neat-No1.mat');
sample4=A.A;
%sample2(:,2)=sample2(:,2)
clear A;
%==========================================
%===============Sample5====================
A = csvread('GNP(1.0%)(1.5).csv');
sample5=A;

clear A;
%==========================================
%===============Sample6====================
A = csvread('GNP(1.0%)(15).csv');
sample6=A;

clear A;
%==========================================
%===============Sample7====================
A = csvread('GNP(1.0%)(150).csv');
sample7=A;

clear A;
%==========================================
%===============Sample8====================
A = csvread('GNP(1.0%)(1500).csv');
sample8=A;

clear A;
%==========================================
%===============Sample9====================
A = csvread('GNP(0.5%)(1.5).csv');
sample9=A;

clear A;
```

```
%=============================================
%===============Sample10=====================
A = csvread('GNP(0.25%)(1.5).csv');
sample10=A;
clear A;
%=============================================
%=================Sample_111==================
A = csvread('CNT(0.5%)(1.5).csv');
sample111=A;
%sample2(:,2)=sample2(:,2)
clear A;
%=============================================
%=================Sample_112==================
A = csvread('CNF(0.5%)(1.5).csv');
sample112=A;
%sample2(:,2)=sample2(:,2)
clear A;
%=============================================
%=================Sample_121==================
A = load('sample121.mat');
sample121=A.sample121;
%sample2(:,2)=sample2(:,2)
clear A;
%=============================================
%Load Numerical
%
load sample15;
load sample16;
load sample17;
load sample18;

load sample19;
load sample11;
load sample121;
load sample122;
```

```
%==============================%row-mat%==================================%
function [ A ] = row_mat( B )
%UNTITLED2 Summary of this function goes here
%   Detailed explanation goes here
A=zeros(3);
A(1,1)=B(1,1);
A(2,2)=B(1,2);
A(3,3)=B(1,3);
A(1,2)=B(1,4);
A(2,1)=B(1,4);
A(1,3)=B(1,5);
A(3,1)=B(1,5);
A(2,3)=B(1,6);
A(3,2)=B(1,6);
end
```

```
%================================%mat_col%=================================
%
function [ A ] = mat_col( B )
%UNTITLED2 Summary of this function goes here
%   Detailed explanation goes here
A(1,1)=B(1,1);
A(1,2)=B(2,2);
A(1,3)=B(3,3);
A(1,4)=B(1,2);
A(1,5)=B(1,3);
A(1,6)=B(2,3);
A=transpose(A);
end
```

```
%============================%Tnag_modulus_calc%============================%
test=sample18;
differential1=diff(test(:,2))./diff(test(:,1))
%differential2=diff(sample1(:,2))./diff(sample1(:,1));
NNN=size(sample1);
clc
differential1(1:100,1)
```

```
%================================%output%==================================%
clear sample11
temp1=size(STR);
n=temp1(1,1);
sample11(:,1)=STR(:,1);
sample11(:,2)=SIG(:,1);
save ('sample11.mat','sample11');
```

```
%==================================%Plot%====================================%

figure(1)

 %subplot(2,2,1)

 grid on
 hold on
 %====================Numerical Graphs=========================

 plot(STR(:,1),SIG(:,1),'b', 'linewidth',2)
 %plot(STR(2:n,1),sig_c(:,1),'k', 'linewidth',2)

 %====================Experiment Graphs=========================
 plot(sample1(:,1),sample1(:,2)*1e6,'--bo', 'linewidth',2)
 %plot(sample15(:,1),sample15(:,2),'--r*', 'linewidth',2)
%  plot(sample3(:,1),sample3(:,2)*1e6,'--g', 'linewidth',2)
%  plot(sample4(:,1),sample4(:,2)*1e6,'--m', 'linewidth',2)
%

 xlim([0 0.03])
 set(gca,'FontSize',14)
 ttl_temp=' with strain rate ';
 ttl=[material ttl_temp num2str(str_rate)];
 % title(ttl)
 %legend('Numerical','EXP-rate 1.5 mm/min','EXP-rate 15 mm/min','EXP-rate
150 mm/min','EXP-rate 1500 mm/min')
 %legend('Numerical','EXP-rate 1500 mm/min','')

 ylabel('Stress')
 xlabel('Strain')
```

```
%================================%Plot13%=================================%
hFig2 = figure(2);

set(gcf,'position',[0,0,500,300])
set(gcf,'units','centimeter')
set(gcf,'papersize',[10,6])
set(gcf,'paperposition',[0,0,10,6])

set(gca, 'XTick', [0:0.002:0.03]);
set(gca, 'fontsize', 14, 'linewidth', 1)
grid on
hold on

%====================Numerical Graphs=========================
mat_s1=size (sample11);
mat_s2=size (sample122);
mat_s3=size (sample121);
mat_s4=size (sample19);

plot(sample11(1:100:mat_s1(1,1),1),sample11(1:100:mat_s1(1,1),2)/1e6,'b',
'linewidth',1.5)
plot(sample1(:,1),sample1(:,2),'b:*', 'linewidth',1.5,'MarkerSize',8)

plot(sample122(1:mat_s2(1,1),1),sample122(1:mat_s2(1,1),2)/1e6,'g',
'linewidth',1.5)
plot(sample112(:,1),sample112(:,2),'g:s', 'linewidth',1.5,'MarkerSize',8)

plot(sample121(1:mat_s2(1,1),1),sample121(1:mat_s2(1,1),2)/1e6,'m',
'linewidth',1.5)
plot(sample111(:,1),sample111(:,2),'m:o', 'linewidth',1.5,'MarkerSize',8)

plot(sample19(1:20:mat_s4(1,1),1),sample19(1:20:mat_s4(1,1),2)/1e6,'r',
'linewidth',1.5)
plot(sample9(:,1),sample9(:,2),'r:^', 'linewidth',1.5,'MarkerSize',8)


 xlim([0 0.022])
 ylim([0 70])

 legend('Neat WS-Predicted','Neat WS',...
        'WS 0.5% CNF-Predicted','WS 0.5% CNF',...
       'WS 0.5% CNT-Predicted','WS 0.5% CNT ',...
        'WS 0.5% GNP-Predicted','WS 0.5% GNP ',...
       'Location','southeast');

 ylabel('Stress (MPa)')
 xlabel('Strain')
 print('-dtiff','-r300','new folder\res13.tiff');
```

```
%================================%Plot14%=================================%
hFig3 = figure(3);

 set(gcf,'position',[0,400,500,300])
 set(gcf,'units','centimeter')
 set(gcf,'papersize',[10,6])
 set(gcf,'paperposition',[0,0,10,6])
 set(gca, 'XTick', [0:0.002:0.03]);
 set(gca, 'fontsize', 14, 'linewidth', 1)
grid on
hold on
 %====================Numerical Graphs=========================
 mat_s1=size (sample11);
 mat_s2=size (sample19);
 mat_s3=size (sample15);


plot(sample11(1:100:mat_s1(1,1),1),sample11(1:100:mat_s1(1,1),2)/1e6,'b',
'linewidth',1.5)
plot(sample1(:,1),sample1(:,2),'b:*', 'linewidth',1.5,'MarkerSize',8)

plot(sample19(1:20:mat_s2(1,1),1),sample19(1:20:mat_s2(1,1),2)/1e6,'g',
'linewidth',1.5)
plot(sample9(:,1),sample9(:,2),'g:s', 'linewidth',1.5,'MarkerSize',8)

plot(sample15(1:mat_s3(1,1),1),sample15(1:mat_s3(1,1),2)/1e6,'m',
'linewidth',1.5)
plot(sample5(:,1),sample5(:,2),'m:o', 'linewidth',1.5,'MarkerSize',8)

legend('Neat WS-Predicted','Neat WS',...
       'WS 0.5% GNP-Predicted','WS 0.5% GNP',...
       'WS 1.0% GNP-Predicted','WS 1.0% GNP ',...
       'Location','southeast');


 xlim([0 0.02])
 ylim([0 70])


 ylabel('Stress (MPa)')
 xlabel('Strain')
 print('-dtiff','-r300','new folder\res14.tiff');
```

```
%==============================%Plot15%==================================%
hFig4 = figure(4);

 set(gcf,'position',[0,0,500,300])
 set(gcf,'units','centimeter')
 set(gcf,'papersize',[10,6])
 set(gcf,'paperposition',[0,0,10,6])
 set(gca, 'XTick', [0:0.002:0.03]);
 set(gca, 'fontsize', 14, 'linewidth', 1)

grid on
hold on
 %====================Numerical Graphs=======================
 mat_s1=size (sample15);
 mat_s2=size (sample16);
 mat_s3=size (sample17);
 mat_s4=size (sample18);


plot(sample15(1:mat_s1(1,1),1),sample15(1:mat_s1(1,1),2)/1e6,'b',
'linewidth',1.5)
plot(sample5(:,1),sample5(:,2),'b:*', 'linewidth',1.5,'MarkerSize',8)

plot(sample16(1:mat_s2(1,1),1),sample16(1:mat_s2(1,1),2)/1e6,'g',
'linewidth',1.5)
plot(sample6(:,1),sample6(:,2),'g:s', 'linewidth',1.5,'MarkerSize',8)

plot(sample17(1:mat_s3(1,1),1),sample17(1:mat_s3(1,1),2)/1e6,'m',
'linewidth',1.5)
plot(sample7(:,1),sample7(:,2),'m:o', 'linewidth',1.5,'MarkerSize',8)

plot(sample18(1:mat_s3(1,1),1),sample18(1:mat_s4(1,1),2)/1e6,'r',
'linewidth',1.5)
plot(sample8(:,1),sample8(:,2),'r:^', 'linewidth',1.5,'MarkerSize',8)

 %====================Experimental Graphs=======================

legend('WS  1.0% GNP 1e-3 1/s Predicted', 'WS  1.0% GNP 1e-3 1/s',...
       'WS  1.0% GNP 1e-2 1/s Predicted', 'WS  1.0% GNP 1e-2 1/s',...
       'WS  1.0% GNP 1e-1 1/s Predicted', 'WS  1.0% GNP 1e-1 1/s ',...
       'WS  1.0% GNP 1e0 1/s Predicted','WS  1.0% GNP 1e0 1/s',...
       'location','southeast')

 xlim([0 0.022])
 ylim([0 80])


 ylabel('Stress (MPa)')
 xlabel('Strain')

 print('-dtiff','-r300','new folder\res15.tiff');
```

```
%================================%Plot16%=================================%
hFig5 = figure(5);

set(gcf,'position',[600,400,500,300])
set(gcf,'units','centimeter')
set(gcf,'papersize',[10,6])
set(gcf,'paperposition',[0,0,10,6])

set(gca, 'XTick', [0:0.002:0.03]);
set(gca, 'fontsize', 14, 'linewidth', 1)
grid on
hold on

%====================Numerical Graphs=========================
mat_s1=size (sample11);

differential1=diff(sample11(:,2))./diff(sample11(:,1));
differential2=diff(sample1(:,2))./diff(sample1(:,1));
NNN=size(sample1);

plot(sample11(1:mat_s1(1,1)-1,1),differential1/1e9,'b', 'linewidth',1.5)
plot(sample1(1:NNN(1)-1,1),differential2/1e3,'ro',
'linewidth',1.5,'MarkerSize',8)


 xlim([0 0.022])


 legend('Neat WS-Predicted','Neat WS-Test Data',...
        'Location','northeast');

 ylabel('Tangential Modulus (GPa)')
 xlabel('Strain')
 print('-dtiff','-r300','new folder\differential.tiff');
```

Appendix III

Developed MATLAB codes used to calculate vibration response of prismatic beams with rectangular cross-section resting on Pasternak elastic foundation:

```
%======================%Main-Vibration Response%=========================%
%Timoshenko beam in free vibrations
clear; clc
% L: length,  bb: width,  hh: thickness, (m, AL)
E=70e9;       poisson = 0.33;     rho=2700;
L =0.2;     bb=0.02;            hh=0.0035;

nElem = 25;                 % Element Number
f0 = -1;                    % uniform pressure
BC=1;                       % boundary conditions 1: S-S,  2: C-C,  3: C-F
Ra=0.5;      Rb=1e-5;       % Rayleigh damping - Cr=Ra*M+Rb*K   (AL)

ti=0;    dt=5e-8;    tf=50e-3;   %tf=20e-3;


I=bb*hh^3/12;  EI=E*I;  kapa=5/6;   A=bb*hh;   t=ti:dt:tf;  nt=length(t);

% constitutive matrix
G=E/2/(1+poisson);   Cmat=[ EI 0; 0 kapa*hh*G];

% mesh
nodeCoordinates=linspace(0,L,nElem+1);   xx=nodeCoordinates';

Nodal=zeros(nElem,2);
for i=1:size(nodeCoordinates,2)-1
    Nodal(i,1)=i;    Nodal(i,2)=i+1;
end

% generation of coordinates and connectivities
nNodes=size(xx,1);

% GDof: global number of degrees of freedom
sdof=2*nNodes;   %%%% [1:nNodes for w ;  nNodes:2*nNodes for Tx]

% computation of the system stiffness, force, mass
[kk,ff,mm]=M_K_F_TimoshenkoBeam(sdof,nElem,Nodal,nNodes,xx,Cmat,f0,rho,I,A);

% BC application
[mm_b,kk_b,ff_b]=feaply_MKF(mm,kk,ff,BC,nNodes);

% Damping Matrix
cc=Ra*mm+Rb*kk;       cc_b=Ra*mm_b+Rb*kk_b;

%=========================================================================

% Static Response UNDER BOUNDARY CONDITIONS
SR=kk_b\ff_b;
W_max=max(abs(SR(1:length(xx))))
```

```
figure(1); hold on; plot(xx*1000,SR(1:length(xx))*1e6)
xlabel('x (mm)'); ylabel('deflection (\mum)');
title('Static response (initial condition) - Beam with BC');

%=========================================================================

% Natural frequencies and Mode shapes
[ss_free,NA_free]=eig(kk,mm);          na_free=sqrt(diag(NA_free));
nas_free=sort(na_free);                nas_Hz_free=nas_free/2/pi;

[ss_BC,NA_BC]=eig(kk_b,mm_b);          na_BC=sqrt(diag(NA_BC));
nas_BC=sort(na_BC);                    nas_Hz_BC=nas_BC/2/pi;

one_to_4=ModeShape_Ploter(ss_free,ss_BC,xx,BC,nNodes);

Omega_free_HZ=nas_Hz_free(3:6)'
Omega_BC_HZ=nas_Hz_BC(one_to_4)'
%=========================================================================%

% time history of vibrations
First=1;  Mid=ceil(nNodes/2);  Last=nNodes;
FF=zeros(sdof,1);   sv=zeros(sdof,1);

su_f(:,1)=SR;     % static response of the beam with a BC is initial
displacement

% compute displacement and acceleration

% free-free beams with
inv_mm_f=inv(mm);
sa_f=inv_mm_f*(FF(:,1)-cc*sv(:,1)-kk*su_f(:,1));     %%initial Acceleration
vector%%
su0_f=su_f(:,1)-dt*sv(:,1)+(dt^2)*sa_f/2;
M_ef_f=mm/(dt^2)+cc/(2*dt);    inv_Mef_f=inv(M_ef_f);

h1_f=kk-2*mm/(dt^2);  h2_f=mm/(dt^2)-cc/(2*dt);
FEt_f=FF(:,1)-h1_f*su_f(:,1)-h2_f*su0_f;   su_f(:,2)=inv_Mef_f*FEt_f;

uselect_f(1,:)=[su_f(First,1),su_f(Mid,1),su_f(Last,1)];
uselect_f(2,:)=[su_f(First,2),su_f(Mid,2),su_f(Last,2)];

%=================================================================%

% beams with BC
su_b(:,1)=SR;

inv_mm_b=inv(mm_b);
sa_b=inv_mm_b*(FF(:,1)-cc_b*sv(:,1)-kk_b*su_b(:,1)); %%initial Acceleration
vector%%
su0_b=su_b(:,1)-dt*sv(:,1)+(dt^2)*sa_b/2;
M_ef_b=mm_b/(dt^2)+cc_b/(2*dt);    inv_Mef_b=inv(M_ef_b);

h1_b=kk_b-2*mm_b/(dt^2);  h2_b=mm_b/(dt^2)-cc_b/(2*dt);
FEt=FF(:,1)-h1_b*su_b(:,1)-h2_b*su0_b;   su_b(:,2)=inv_Mef_b*FEt;

uselect_b(1,:)=[su_b(First,1),su_b(Mid,1),su_b(Last,1)];
uselect_b(2,:)=[su_b(First,2),su_b(Mid,2),su_b(Last,2)];
```

```
%=============================================================%

for it=2:nt-1

    FEt_f=FF(:,1)-h1_f*su_f(:,it)-h2_f*su_f(:,it-1);
    su_f(:,it+1)=inv_Mef_f*FEt_f;
    uselect_f(it+1,:)=[su_f(First,it+1),su_f(Mid,it+1),su_f(Last,it+1)];

    FEt_b=FF(:,1)-h1_b*su_b(:,it)-h2_b*su_b(:,it-1);
    su_b(:,it+1)=inv_Mef_b*FEt_b;
    uselect_b(it+1,:)=[su_b(First,it+1),su_b(Mid,it+1),su_b(Last,it+1)];
end


figure(21); hold on; plot(t*1000,uselect_f(:,1)*1e6); % first end
xlabel('t (ms)'); ylabel('first node deflection (\mum)');
title('first node - Free-Free Beam');

figure(22); hold on; plot(t*1000,uselect_f(:,2)*1e6); %mid surf
xlabel('t (ms)'); ylabel('mid node deflection (\mum)');
title('mid node - Free-Free Beam');

% figure(23); hold on; plot(t*1000,uselect_f(:,3)*1e6); % last node
% xlabel('t (ms)'); ylabel('last node deflection (\mum)');
% title('last node - Free-Free Beam');

%=============================================================%

figure(31); hold on; plot(t*1000,uselect_b(:,1)*1e6); % first end
xlabel('t (ms)'); ylabel('first node deflection (\mum)');
title('first node - Beam with BC');

figure(32); hold on; plot(t*1000,uselect_b(:,2)*1e6); %mid surf
xlabel('t (ms)'); ylabel('mid node deflection (\mum)');
title('mid node - Beam with BC');

% figure(33); hold on; plot(t*1000,uselect_b(:,3)*1e6); % last node
% xlabel('t (ms)'); ylabel('last node deflection (\mum)');
% title('last node -  Beam with BC');


% calculating of zeta

X=t;     Y_b=uselect_b(:,2);     Y_f=uselect_f(:,2);
Ave_Yf=sum(Y_f)/length(Y_f);     Y_f2=Y_f-Ave_Yf;

[pks_f,locs_f] = findpeaks(Y_f2,X,'MinPeakDistance',0.7/Omega_free_HZ(1));
figure(35); hold on; plot(t*1000,Y_f2*1e6,locs_f*1000,pks_f*1e6,'o')
xlabel('t (ms)'); ylabel('mid node deflection (\mum)');
title('mid node - Free-Free Beam');

[pks_b,locs_b] = findpeaks(Y_b,X,'MinPeakDistance',0.7/Omega_BC_HZ(1));
figure(32); hold on; plot(locs_b*1000,pks_b*1e6,'o')
xlabel('t (ms)'); ylabel('mid node deflection (\mum)');
title('mid node - Beam with BC');
```

```
%%% y=A0 e ^(-zeta * wn * t) or a*exp(b*t)

f_f = fit(locs_f',pks_f,'exp1')
f_b = fit(locs_b',pks_b,'exp1')


%======= after importing a and b values from the main window ========%

a1=1.545e-06
b1=-41.86
a2=4.161e-06
b2=-8.33
figure(35); hold on; plot(t*1000,a1*1e6*exp(b1*t))
zeta_free=-b1/1000/Omega_free_HZ(1)

figure(32); hold on; plot(t*1000,a2*1e6*exp(b2*t))
zeta_BC=-b2/1000/Omega_BC_HZ(1)
```

```
%==============================%feaply_MKF%================================%
function [M,K,F]=feaply_MKF(M,K,F,BC,nNodes)

if BC==1                                    % (simply-supported at both ends)
    fixedNodeW =[1 ; nNodes];    fixedNodeTX=[];
elseif BC==2                                % (clamped at both ends)
    fixedNodeW =[1 ; nNodes];    fixedNodeTX=fixedNodeW;
else                                        % (cantilever)
    fixedNodeW =1;    fixedNodeTX=1;
end

fixedDof=[fixedNodeW;fixedNodeTX+nNodes]; n=length(fixedDof); sdof=size(K);

for i=1:n
    c=fixedDof(i);
    for j=1:sdof
        K(c,j)=0;        K(j,c)=0;
        M(c,j)=0;        M(j,c)=0;
    end
    K(c,c)=1;    M(c,c)=1;    F(c,:)=0;
end
```

```
%========================%M_K_F_TimoshenkoBeam%=========================%
function [stiffness,force,mass]=M_K_F_TimoshenkoBeam(GDof,numberElements,...
elementNodes,numberNodes,xx,C,P,rho,I,AA)
% computation of stiffness matrix and force vector
% for Timoshenko beam element
stiffness=zeros(GDof);
mass=zeros(GDof);
force=zeros(GDof,1);
% stiffness matrix
gaussLocations=[0.577350269189626;-0.577350269189626];
gaussWeights=ones(2,1);
% bending contribution for stiffness matrix
for e=1:numberElements
```

```
indice=elementNodes(e,:);
elementDof=[ indice indice+numberNodes];
indiceMass=indice+numberNodes;
ndof=length(indice);
length_element=xx(indice(2))-xx(indice(1));
detJacobian=length_element/2;invJacobian=1/detJacobian;
for q=1:size(gaussWeights,1)
pt=gaussLocations(q,:);
[shape,naturalDerivatives]=shapeFunctionL2(pt(1));
Xderivatives=naturalDerivatives*invJacobian;
% B matrix
B=zeros(2,2*ndof);
B(1,ndof+1:2*ndof) = Xderivatives(:)';
% K
stiffness(elementDof,elementDof)=stiffness(elementDof,elementDof)+...
B'*B*gaussWeights(q)*detJacobian*C(1,1);

force(indice)=force(indice)+shape*P*detJacobian*gaussWeights(q);

mass(indiceMass,indiceMass)=mass(indiceMass,indiceMass)+...
shape*shape'*gaussWeights(q)*I*rho*detJacobian;

mass(indice,indice)=mass(indice,indice)+...
    shape*shape'*gaussWeights(q)*AA*rho*detJacobian;
end
end

% shear contribution for stiffness matrix
gaussLocations=[0.];  gaussWeights=[2.];

for e=1:numberElements
indice=elementNodes(e,:);
elementDof=[ indice indice+numberNodes];
ndof=length(indice);
length_element=xx(indice(2))-xx(indice(1));
detJ0=length_element/2;   invJ0=1/detJ0;
for q=1:size(gaussWeights,1)
pt=gaussLocations(q,:);
[shape,naturalDerivatives]=shapeFunctionL2(pt(1));
Xderivatives=naturalDerivatives*invJacobian;
% B
B=zeros(2,2*ndof);
B(2,1:ndof) = Xderivatives(:)';   B(2,ndof+1:2*ndof) = shape;
% K
stiffness(elementDof,elementDof)=stiffness(elementDof,elementDof)+...
B'*B*gaussWeights(q)*detJacobian*C(2,2);
end
end
```

```
%============================%ModeShape_Ploter%==============================%
function one_to_4=ModeShape_Ploter(ss_free,ss_BC,xx,BC,nNodes)

uf1=ss_free(1:nNodes,3);       uf2=ss_free(1:nNodes,4);
uf3=ss_free(1:nNodes,5);       uf4=ss_free(1:nNodes,6);
```

```
figure(11);plot(xx,uf1,xx,uf2,xx,uf3,xx,uf4);
legend('1^s^t','2^n^d','3^r^d','4^t^h')
title('Modeshapes of a Free-Free Beam');

%%%% modesapes of Beam with BC
if BC==2                                    % (clamped at both ends)
    ub1=ss_BC(1:nNodes,5);       ub2=ss_BC(1:nNodes,6);
    ub3=ss_BC(1:nNodes,7);       ub4=ss_BC(1:nNodes,8);
    one_to_4=5:8;
else                                         % (S-S OR cantilever)
    ub1=ss_BC(1:nNodes,3);       ub2=ss_BC(1:nNodes,4);
    ub3=ss_BC(1:nNodes,5);       ub4=ss_BC(1:nNodes,6);
    one_to_4=3:6;
end

figure(12);plot(xx,ub1,xx,ub2,xx,ub3,xx,ub4);
legend('1^s^t','2^n^d','3^r^d','4^t^h')
title('Modeshapes of a Beam with BC');
```

```
%============================%shapeFunctionL2%============================%
function [shape,naturalDerivatives]=shapeFunctionL2(xi)
% shape function and derivatives for L2 elements
% shape : Shape functions
% naturalDerivatives: derivatives w.r.t. xi
% xi: natural coordinates (-1 ... +1)
shape=([1-xi,1+xi]/2)';
naturalDerivatives=[-1;1]/2;
end % end function shapeFunctionL2
```

Appendix IV

LS-Dyna *.k-file used in finite element analysis to determine the frequencies of the beam with rectangular cross-section resting on Pasternak elastic foundation (in this case Neat-4-FML (3D-FML1) with free-free boundary condition); to avoid boredom and to save the space only first- and last-ten nodes and elements have been mentioned here:

```
$# LS-DYNA Keyword file created by LS-PrePost(R) V4.3 - 30Oct2019(20:00)
$# Created on Feb-07-2020 (18:55:08)
*KEYWORD MEMORY=125M
*TITLE
$#                                                                title
LS-DYNA keyword deck by LS-PrePost
*CONTROL_ACCURACY
$     OSU       INN    PIDOSU      IACC
$#     osu       inn    pidosu      iacc
       1         4         0         1
*CONTROL_IMPLICIT_EIGENVALUE
$#    neig    center     lflag    lftend     rflag    rhtend    eigmth    shfscl
      10       0.0         0-1.0000E29         01.00000E29         2       0.0
$#  isolid     ibeam    ishell   itshell    mstres    evdump   mstrscl
       0         0         0         0         0         0     0.001
*CONTROL_IMPLICIT_GENERAL
$   IMFLAG       DT0    IMFORM      NSBS       IGS     CNSTN      FORM
$#  imflag       dt0    imform      nsbs       igs     cnstn      form    zero_v
       1       1.0         2         1         2         0         0         0
*CONTROL_IMPLICIT_SOLUTION
$#  nsolvr    ilimit    maxref     dctol     ectol     rctol     lstol    abstol
       1        11        15     0.001     0.011.00000E10      0.91.0000E-10
$#   dnorm    diverg     istif   nlprint    nlnorm   d3itctl     cpchk
       2         1     99999         1         2         0         0
$#  arcctl    arcdir    arclen    arcmth    arcdmp    arcpsi    arcalf    arctim
       0         0       0.0         1         2         0         0         0
$#   lsmtd     lsdir      irad      srad      awgt      sred
       4         2       0.0       0.0       0.0       0.0
*CONTROL_OUTPUT
$   NPOPT    NEECHO    NREFUP    IACCOP     OPIFS    IPNINT    IKEDIT    IFLUSH
$#   npopt    neecho    nrefup    iaccop     opifs    ipnint    ikedit    iflush
       1         3         0         0       0.0         0       100      5000
$   IPRTF    IERODE     TET10    MSGMAX    IPCURV
$#   iprtf    ierode    tet10s8    msgmax    ipcurv      gmdt   ip1dblt      eocs
       0         0         1        50         0       0.0         0         0
$   TOLEV    NEWLEG    FRFREQ     MINFO    SOLSIG    MSGFLG
$#   tolev    newleg    frfreq     minfo    solsig    msgflg    cdetol
       2         0         1         1         0         1      10.0
*CONTROL_TERMINATION
$#  endtim    endcyc     dtmin    endeng    endmas
     1.0         0       0.0       0.01.000000E8
*PART
```

```
$#                                                  title
Bottom Skin
$#    pid     secid       mid     eosid      hgid      grav    adpopt      tmid
        1         1         2         0         0         0         0         0
*SECTION_SOLID_TITLE
Section-Solid
$#   secid    elform       aet
        1         1         0
*MAT_ELASTIC_TITLE
Magnesium
$#     mid        ro         e        pr        da        db  not used
       21.74000E-6      36.0      0.35       0.0       0.0         0
*PART
$#                                                  title
Bottom Adhesive
$#    pid     secid       mid     eosid      hgid      grav    adpopt      tmid
        2         1         5         0         0         0         0         0
*MAT_ELASTIC_TITLE
Adhesive
$#     mid        ro         e        pr        da        db  not used
       51.18000E-6     2.708       0.3       0.0       0.0         0
*PART
$#                                                  title
Bottom Ply
$#    pid     secid       mid     eosid      hgid      grav    adpopt      tmid
        3         1         3         0         0         0         0         0
*MAT_ORTHOTROPIC_ELASTIC_TITLE
Skin Ply
$#     mid        ro         ea        eb        ec      prba      prca      prcb
       31.63000E-6       9.3       9.3       1.0      0.25     0.028     0.028
$#     gab       gbc       gca      aopt         g      sigf
      1.0       1.0       1.0       2.0       0.0       0.0
$#      xp        yp        zp        a1        a2        a3      macf
      0.0       0.0       0.0       1.0       0.0       0.0         1
$#      v1        v2        v3        d1        d2        d3      beta       ref
      0.0       0.0       0.0       0.0       0.0       1.0       0.0       0.0
*PART
$#                                                  title
Pillars
$#    pid     secid       mid     eosid      hgid      grav    adpopt      tmid
        4         1         4         0         0         0         0         0
*MAT_ORTHOTROPIC_ELASTIC_TITLE
Core Pillars
$#     mid        ro         ea        eb        ec      prba      prca      prcb
       41.63000E-6       3.1      1.03       1.0     0.083     0.083      0.25
$#     gab       gbc       gca      aopt         g      sigf
      1.0       1.0       1.0       2.0       0.0       0.0
$#      xp        yp        zp        a1        a2        a3      macf
      0.0       0.0       0.0       0.5      0.86       0.0         1
$#      v1        v2        v3        d1        d2        d3      beta       ref
      0.0       0.0       0.0       0.0       1.0       0.0       0.0       0.0
*PART
$#                                                  title
Top Ply
$#    pid     secid       mid     eosid      hgid      grav    adpopt      tmid
        5         1         3         0         0         0         0         0
```

```
*PART
$#                                                  title
Top Adhesive
$#    pid    secid      mid    eosid     hgid     grav   adpopt     tmid
      6        1        5        0        0        0        0        0
*PART
$#                                                  title
Top Skin
$#    pid    secid      mid    eosid     hgid     grav   adpopt     tmid
      7        1        2        0        0        0        0        0
*ELEMENT_SOLID
$#   eid    pid     n1     n2     n3     n4     n5     n6     n7     n8
     1      3      1      2   1080   1079   5391   5392   5490   5489
     2      3      2      3   1081   1080   5392   5393   5491   5490
     3      3      3      4   1082   1081   5393   5394   5492   5491
     4      3      4      5   1083   1082   5394   5395   5493   5492
     5      3      5      6   1084   1083   5395   5396   5494   5493
     6      3      6      7   1085   1084   5396   5397   5495   5494
     7      3      7      8   1086   1085   5397   5398   5496   5495
     8      3      8      9   1087   1086   5398   5399   5497   5496
     9      3      9     10   1088   1087   5399   5400   5498   5497
    10      3     10     11   1089   1088   5400   5401   5499   5498
     .
     .
     .
     .
 23990      7  27467  27468  30682  30681  27446  27447  30637  30636
 23991      7  27468  27469  30683  30682  27447  27448  30638  30637
 23992      7  29922  30681  30684  30020  28452  30636  30687  30118
 23993      7  30681  30682  30685  30684  30636  30637  30688  30687
 23994      7  30682  30683  30686  30685  30637  30638  30689  30688
 23995      7  27424  27470  30693  30314  26836  27452  30642  28648
 23996      7  27470  27471  30694  30693  27452  27453  30643  30642
 23997      7  27471  27472  30695  30694  27453  27454  30644  30643
 23998      7  30314  30693  30696  30412  28648  30642  30699  30510
 23999      7  30693  30694  30697  30696  30642  30643  30700  30699
 24000      7  30694  30695  30698  30697  30643  30644  30701  30700
*NODE
$#   nid            x            y            z       tc      rc
     1          0.0        -2.25          0.0        0       0
     2          2.0        -2.25          0.0        0       0
     3          4.0        -2.25          0.0        0       0
     4          6.0        -2.25          0.0        0       0
     5          8.0        -2.25          0.0        0       0
     6         10.0        -2.25          0.0        0       0
     7         12.0        -2.25          0.0        0       0
     8         14.0        -2.25          0.0        0       0
     9         16.0        -2.25          0.0        0       0
    10         18.0        -2.25          0.0        0       0
     .
     .
     .
     .
 30695        200.0     2.565001        17.75        0       0
 30696        196.0     2.789999       17.825        0       0
 30697        198.0     2.789999       17.825        0       0
```

```
  30698      200.0     2.789999     17.825     0     0
  30699      196.0     2.789999     18.175     0     0
  30700      198.0     2.789999     18.175     0     0
  30701      200.0     2.789999     18.175     0     0
  30702      196.0     2.789999     20.0       0     0
  30703      198.0     2.789999     20.0       0     0
  30704      200.0     2.789999     20.0       0     0
*END
```